Durham E-Theses

Monte Carlo simulations of electron transport in quantum well heterostructures

Hoare, David

How to cite:

Hoare, David (1993) *Monte Carlo simulations of electron transport in quantum well heterostructures*, Durham theses, Durham University. Available at Durham E-Theses Online: http://etheses.dur.ac.uk/5557/

Use policy

MONTE CARLO SIMULATIONS OF

ELECTRON TRANSPORT IN

QUANTUM WELL HETEROSTRUCTURES

by

David Hoare, B.Sc.

A thesis

submitted in candidature for

the degree of Doctor of Philosophy

at the University of Durham

(Physics Department)

September 1993

-7 JUN 1994

DECLARATION

I hereby declare that the work reported in this thesis has not previously been submitted for any degree and is not being currently submitted in candidature for any other degree.

_____

The work reported in this thesis was carried out by the candidate.

_____

PhD Supervisor

_____

PhD Candidate

" 'Now, Hobson, you think you've

got me there. You think I don't know

what a thesis is. Well I do. I've got

a daughter at a polytechnic and she's

doing one. Great fat bundle of words

about sod all. What's yours about?' "

Mr. Forrest

The Beiderbecke Affair

by Alan Plater

Dedicated to:

Estelle Norton

Irene Hoare

Barrie Hoare (Snr.)

Susan Hoare

Steven Barrie Hoare

James Hoare

Barrie Hoare (Jnr.)

Kathrin Hoare

ACKNOWLEDGEMENTS

ABSTRACT
MONTE CARLO SIMULATIONS OF ELECTRON TRANSPORT IN QUANTUM WELL HETEROSTRUCTURES
Ph.D. Thesis 1993, by David Hoare, B.Sc.

The parallel transport of electrons in pseudomorphic $In_xGa_{1-x}As$/GaAs quantum wells is influenced by the degree of spacial confinement and by the effect of the indium concentration which determines, the amount of alloy scattering, the subband structure, and material parameters. The indium content changes the bandstructure and material parameters through both direct compositional and strain effects. We use the single particle and ensemble methods of Monte-Carlo simulation to investigate how the above phenomena influence the transport properties of electrons in $In_xGa_{1-x}As$/GaAs quantum wells.

To understand the effects of alloying and strain on the electron transport properties we first consider electrons in bulk $In_xGa_{1-x}As$. Alloying and strain are considered in artificial systems were the effect(s) of these factors on electron transport may be isolated. For a range of indium compositions, we consider independently the effects of alloying (with and without alloy scattering) and strain on the bandstructure and material parameters and, in turn, their effects on the electron transport properties. We show that increasing the indium concentration generally improves the carrier low field mobility and peak velocity of unstrained materials but has a detrimental effect on the saturation velocity. Strain reduces the low field mobility and peak velocity but gives a slightly higher saturation velocity when compared to GaAs, and the unstrained system.

Comparison of transient and steady state transport phenomena is made for strained $In_{0.15}Ga_{0.85}As$/GaAs quantum well structures, at fields high enough for real- and reciprocal-space transfer to occur. An artificial case, called the unstrained system, where the strain effects on the bandstructure and material parameters are neglected is also considered. Differences between the strained and unstrained well results are small and mainly transient. At steady state, most of the electrons for almost all fields reside in unbound states. The strained and unstrained systems show higher low field mobilities when compared to bulk GaAs.

Lattice vibrations are also affected by heterostructures and we have made a study of the effects on the low field transport of electrons in a 70Å $Al_{0.3}Ga_{0.7}As$/GaAs quantum well when the polar optical phonon modes which interact with the electrons are described by three phonon models which describe the lattice vibrations of the heterostructure; the Hydrodynamic Model (HDM), the Dielectric Continuum Model (DCM), and the Bulk Phonon Approximation (BPA). We show that the BPA and HDM predict similar transport effects and are in good agreement with experimental results. We conclude that, at present, the BPA is an adequate model to describe the phonon modes in heterostructure quantum wells for use in transport calculations.

CONTENTS

CHAPTER ONE

INTRODUCTION

*A*lthough silicon is well established as the mainstream material for use in integrated circuits, GaAs and other III-V semiconductors are used in some specialist areas in which they have advantages over silicon (due to smaller effective masses, direct band gaps, etc.) despite an inferior materials technology. One particular area of application, that has been a commercial success, is the low noise, high frequency transistors for use in satellite communication receivers (including satellite T.V.). The transistors used are the so called high electron mobility transistors (HEMTs), a development of the GaAs field effect transistor (FET).

The speed of operation of a HEMT is determined principally by the time it takes carriers to cross the region of the conducting channel under the gate. This is a small, high-field region where the electrons attain high transient-overshoot and saturation velocities. The region between source and gate is a low field region and materials with a high low field mobility are

desirable in order to provide a low source-gate region resistence. A well defined gate voltage at which all carriers are ejected from the channel (the pinch-off voltage) is another desirable characteristic in HEMT operation.

The first HEMT devices used an AlGaAs supply layer grown on an GaAs 'channel' layer which itself was grown on a GaAs substrate. In the HEMT the electrons originate from the doping of the supply layer but are confined in the potential well formed at the interface between the supply layer and the channel material which has a lower band gap. This modulation doping of devices is an improvement over the FET where the donor atoms and carriers are not spacially separated and ionised impurity scattering limits mobility. Further improvements have been made by use of a spacer-layer, a layer of undoped AlGaAs, which further separates the electrons from their donor atoms and so reduces remote ionised impurity scattering. Other ways of improving HEMT performance are being investigated. One development which seems to be particularly advantageous is the introduction of a strained InGaAs channel between the GaAs buffer and AlGaAs supply layers. InGaAs, when compared to GaAs, has a smaller Γ valley effective mass, a higher energy separation between the Γ valley and the satellite valleys, and a smaller band gap. It is hoped that, the smaller Γ valley effective mass will increase carrier velocity in the low field region between the source and gate, the higher energy of the satellite valleys, coupled with the lower Γ valley mass, will decrease the transit time across the region under the gate, and in the high field region between gate and drain real

space transfer will be inhibitted by the smaller band gap of InGaAs causing a deeper confining potential. This smaller band gap also improves carrier control due to the back barrier between it and the GaAs substrate leading to a well defined pinch-off voltage.

It is to the investigation, using the Monte-Carlo method, of transport in a simplified form of this quantum well channel region that the work of this thesis is directed. The Monte-Carlo technique is a very powerful and much used technique for simulation of carrier transport in semiconductor materials and devices. One particularly useful aspect of this method of simulation is the ease in which the effect on the transport properties of specific parameters or processes can be examined. The single particle method is used to study steady state phenomena in homogenous and non-time-varying systems and the ensemble method to investigate inhomogeneous systems and transient effects. Chapter two gives a brief overview of our simulations of electron transport in bulk III-V semiconductors using both the single particle and ensemble Monte-Carlo methods. We report simulations of electron transport in GaAs and InAs and then consider the important issues when simulating electron transport in ternary alloys. Amongst the subjects discussed are the bandstructure and material parameters of alloys along with the electron scattering mechanism, alloy scattering, which is in addition to those in the constituent binary materials. The effect of these matters on the transport properties are considered with particular reference to $In_{0.53}Ga_{0.47}As$ which can be grown epitaxially on InP to which it is lattice matched.

When a material is grown on a substrate of different lattice constant the lattice mismatch can be accommodated in two ways; the lattice constant in either or both materials may change or dislocations may occur. If a thin epitaxial layer is grown on a thick substrate in such a way that the lattice mismatch between the two materials is wholly taken up by a change of the in-plane lattice constant of the layer to that of the substrate then the layer is pseudomorphically strained. Strain has the effect of changing the band structure and other material parameters so that the strained material has different electronic transport properties to that of the unstrained semiconductor. Often the epitaxial layer thickness is sufficiently small to introduce quantum size effects. Also in chapter two, strain effects on bandstructure, material parameters, and transport properties are explored, without carrier quantisation effects, for the artifical system of bulk $In_xGa_{1-x}As$ $(x \leq 0.25)$ strained as though it were a pseudomorphically strained layer.

Longitudinal polar optical phonon scattering is one of the main factors affecting the electron transport properties of III-V semiconductors. It is well agreed how the electron states are affected by semiconductor heterostructures but there is less understanding of how the lattice vibrations are influenced by the interfaces between materials and the geometry of the device. Although the description of the scattering processes and phonon modes in bulk materials is well agreed upon, there is more controversy over the continuum models which describe phonon states of heterostructures and how they interact with the carriers. In chapter three we compare the electron

scattering rates by optical phonons predicted by three continuum phonon models and use a single particle Monte-Carlo model to investigate their effects on electron transport in the subbands of a 70Å $Al_{0.3}Ga_{0.7}As/GaAs$ quantum well.

In the high field regions of the HEMT channel the electrons attain energies at which scattering to unbound states of the Γ valley or the bound and unbound states of the satellite valleys is probable. We therefore need to consider real-space transfer (the scattering between bound and unbound states), reciprocal-space transfer (the scattering between valleys) and a more complete bandstructure model. In chapter four we compare the transport properties predicted by an ensemble Monte-Carlo model of electrons in the quantised states of the Γ, L and X valleys in strained and unstrained $In_{0.15}Ga_{0.85}As/GaAs$ structures. The bandstructure, and how the scattering rates between bound and unbound states is calculated are discussed along with an interpretation of the significant results obtained from these simulations.

Chapter five gives an overview of the work reported in this thesis, some general conclusions, and suggestions as to how this work may be developed.

CHAPTER TWO

SIMULATIONS OF BULK III-V SEMICONDUCTORS

2.1   Introduction.

R̸ecently a lot of research has been devoted to improving the

performance of AlGaAs/GaAs high electron mobility transistors (HEMTs),

in particular the velocity and control of carriers in the conducting channel.

Two areas in which advancements have been sought are in the materials

used and the device design.

$In_xGa_{1-x}As$ ($x \leq 0.25$) has been grown between the AlGaAs supply

and GaAs buffer layers to act as the conducting channel.   It is hoped

to provide a higher low field mobility because it has a lower Γ valley

effective mass than GaAs, and better carrier control due to the extra

confinement provided by the conduction band discontinuity between it and

GaAs.   However, it has two main drawbacks; i) because it has a larger

lattice constant than GaAs (or AlGaAs) it can only be grown in thin

pseudomorphically strained layers and, ii) because it is a ternary alloy the

carriers within it will be scattered due to the random fluctuations of the lattice potential.

Obtaining an understanding of these new structures is complicated by the many contributory factors which affect their performance. The factors we are mainly interested in are due to alloying, strain, and quantisation. In real devices some of these factors cannot be separated, for example strain limits the size of the channel layer and so quantum size effects are introduced, but in our computer simulations each factor can be introduced one at a time and its effect(s) on the transport properties examined.

We shall leave consideration of quantisation effects to later chapters and consider only those effects due to alloying and strain on the electron transport properties of bulk semiconductors.

In order to simulate steady state and transient electron transport in these materials we have used the single particle and ensemble Monte-Carlo methods. A brief description of these methods of numerical solution as applied to carrier transport is given in section 2.2 along with an outline of the material model we have used. The bandstructure used in, and the results from, simulating transport in the binary materials GaAs and InAs are given in section 2.3. In section 2.4 we introduce alloy scattering for ternary III-V semiconductor compounds and describe the main effects, due to alloying, on the conduction bandstructure. Section 2.5 gives the results obtained when we used our Monte-Carlo programs to simulate electrons subjected to electric fields in bulk $In_{0.53}Ga_{0.47}As$. The effects of strain on

the bandstructure and material parameters of bulk alloys are discussed in section 2.6, and results of electron transport simulation in unstrained and strained bulk $In_xGa_{1-x}As$ $(x = 0.05, 0.10, 0.15, 0.20$ and $0.25)$ are given in section 2.7. We finish this chapter with section 2.8 which is a brief summary of the main points of interest and conclusions drawn.

2.2   General features of the simulation model.

2.2.1 Monte-Carlo Method

We have used the Monte-Carlo method to simulate electron transport in a range of III-V semiconductor bulk materials. The method has been extensively discussed and reviewed elsewhere (Jacoboni & Regianni 1983, Fawcett *et al* 1970) and therefore only a brief general summary of the basic features of interest is given here.

Electron transport in semiconductors can be described by the integro-differential equation known as the Boltzmann equation (see for example Butcher 1973). In general no closed form algebraic solution of the Boltzmann equation exists but various methods of numerical solution have been developed (see for example Moglestue 1993). Monte-Carlo simulation is one such method widely used to describe the behaviour of systems which can only be defined probabilistically. When applied to charge transport in

semiconductors, the method consists of a simulation of the motion of one or more particles which represent the electrons inside the crystal. The electrons are subject to the action of external forces due to the applied electric (and magnetic) fields and the effect of certain scattering mechanisms, such as phonon, impurity, and alloy scattering. The duration of the carrier free flight and the scattering events that terminate the free flights are selected stochastically in the simulation, in accordance with the known probabilities describing the microscopic processes, by using random numbers generated by the computer.

When the purpose of the simulation is the investigation of a steady-state transport phenomenon in a spacially homogeneous system, it is normally sufficient to simulate the motion of a single particle. From ergodicity considerations we may assume that the simulation of a sufficiently long path of this particle will give information on the behaviour of the entire electron gas. However, when the transport phenomenon under investigation is time varying in nature or relates to a non-homogeneous system it is necessary to simulate an ensemble of particles. Averages over the whole ensemble at specific times may be taken to determine the time evolution of the system. Normally the quantities of interest are the wavevector, velocity, energy and real space distribution functions and the average drift velocity, although additional microscopic information may be extracted if required.

We have used the single particle Monte-Carlo method to simulate the equilibrium motion of electrons under a fixed electric field. The ensemble

method has been used to model the behaviour of an electron gas to a step function electric field applied at time t=0. These models have been developed from software written by members of the Theory of Semiconductor Materials and Devices Group at the University of Durham, Dr. R. W. Kelsall and Dr. D. T. Hughes.

2.2.2 Scattering processes

The scattering processes included in the simulation of electron transport in bulk binary III-V materials are:-

Polar Optical Phonon Scattering:-

In a polar crystal (e.g. GaAs), the optical modes of lattice vibration (essentially the contrary displacement of adjacent, oppositely charged atoms) create a polarisation, and hence an electric field which acts on the electrons. The associated phonons cause inelastic scattering of the carriers, and are well known as an important scattering mechanism in III-V semiconductors at room temperature.

Non-Polar Optical Phonon Scattering:-

The optical modes generate a strain in the lattice which, through its effect on the bandstructure described by a deformation potential, interacts with the electron. It can be shown by symmetry considerations (Harrison, 1956) that

negligible coupling between electrons and non-polar optical phonons takes place in the Γ and X valleys. Therefore this form of inelastic scattering has only to be included for scattering in the L valleys.

Acoustic Phonon Scattering:-

For acoustic modes of the lattice vibration the displacement of the atoms in the unit cell are in the same direction and causes a strain which interacts with the electron through a deformation potential. At room temperature most scattering events involve phonon energies small compared to typical electron energies, and it is common to assume that electron scattering by acoustic phonons is an elastic process.

Inter-valley Scattering:-

Although in principle inter-valley scattering can be caused by both acoustic and optical large wavevector phonons, we follow the common procedure (see for example Nag 1972) of incorporating an effective phonon scattering mechanism in the deformation potential approximation.

Other mechanisms such as ionised impurity and piezoelectric scattering can also be readily included in Monte-Carlo simulations but have not been taken into account here.

Ionised Impurity Scattering:-

Ionised impurity scattering is a result of the interaction of carriers with the electric field of dopant atoms substituted into the lattice and so does not occur in pure materials. This scattering becomes less effective with increasing carrier kinetic energy. Our concern here is only with low doped or pure materials.

Piezoelectric Scattering:-

In a polar material the strain associated with the acoustic modes creates an electric field which interacts with the carriers. Piezoelectric scattering is insignificant in III-V semiconductors at room temperature (Moglestue 1993).

2.2.3 Band structure.

For GaAs and InAs the three lowest sets of conduction band valleys occur at the Γ, L and X points, in order of increasing energy, and it is sufficient to model only these three sets for the range of fields $(0\text{-}20\text{kVcm}^{-1})$ we are considering. At the band edge, the Γ valley, of the unstrained semiconductor, is spherically symmetric in k-space. The satellite valleys have constant energy surfaces which are ellipsoids of revolution. However, unless otherwise stated, we take all valleys to be spherically symmetric with a parabolic E-k relationship. The satellite valley effective masses are taken as the effective density of states mass of that valley (Moglestue

1993)$(= [m_l^* m_t^{*2}]^{\frac{1}{3}}$, where m_l^* and m_t^* are the longitudinal and transverse effective masses in the valley). These are common approximations in Monte-Carlo models which have proved satisfactory for most purposes.

2.3   Simulation of electron transport in GaAs and InAs.

2.3.1 The bandstructure and related parameters

The conduction bandstructure of GaAs has been extensively investigated and the main features are known with some confidence (Aspnes 1976, Adams *et al* 1977, Littlejohn *et al* 1977, Landolt & Börnstein 1982). The Γ to L separation $(\Delta E_{\Gamma L})$ is 0.33eV and the Γ to X $(\Delta E_{\Gamma X})$ is 0.522eV at room temperature. The effective masses are $0.067m_0$, $0.220m_0$ and $0.580m_0$ for the Γ, L and X valleys respectively.

The InAs conduction band parameters required for the simulations are not as well known as in GaAs. The Γ valley effective mass is taken as $0.023m_0$ (Landolt & Börnstein, 1982). The other aspects of the conduction bandstructure are taken from Brennan & Hess, 1984, who used a pseudopotential method to calculate a $\Delta E_{\Gamma L}$ of 1.082eV, a $\Delta E_{\Gamma X}$ of 1.620eV, and effective masses in the L and X valleys of $0.286m_0$ and $0.640m_0$ respectively. The remaining material data is taken from Adachi, 1982, who collected parameters from many different sources.

Figures 2.1 and 2.2 show the conduction band valley energies and effective masses for GaAs and InAs used in our simulations. Features to note are the smaller effective mass in the Γ valley, the larger Γ to L separation and the larger effective masses of the satellite valleys of in InAs compared to GaAs.

2.3.2 Steady state simulation results.

The velocity field characteristics of GaAs and InAs, at room temperature, predicted by our model are shown in figure 2.3 and can be explained and understood in terms of the bandstructure of the two materials.

The slopes of the curves close to zero field give the low field mobilities as $\mu_{\text{GaAs}} = 0.9 m^2 V^{-1} s^{-1}$ and $\mu_{\text{InAs}} = 3.3 m^2 V^{-1} s^{-1}$. The smaller value for GaAs is explained by its larger Γ valley effective mass. The field value at which the peak velocity occurs and the peak velocity itself are determined by the Γ valley effective mass and the energy separation of the Γ and L valleys. As $\Delta E_{\Gamma L}$ increases the peak velocity and peak-velocity field values increase. When the effective mass decreases the average velocity increases and the electrons reach higher energies for a given field strength prior to significant satellite valley population. However, the peak velocity although possibly higher may occur at lower field strengths. So, as can be seen in figure 2.3, InAs with its smaller Γ valley effective mass and larger $\Delta E_{\Gamma L}$ has a greater peak velocity at a lower field strength in comparison with GaAs. The effective masses of the L and X valleys are greater in InAs and are the reason for a saturation velocity which is lower than in
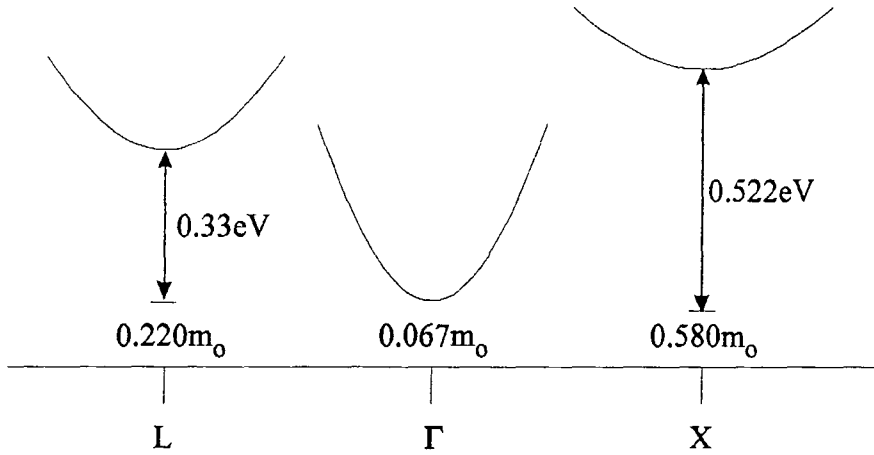
Figure 2.1

The energy separations and effective masses of the conduction

band valleys in GaAs.
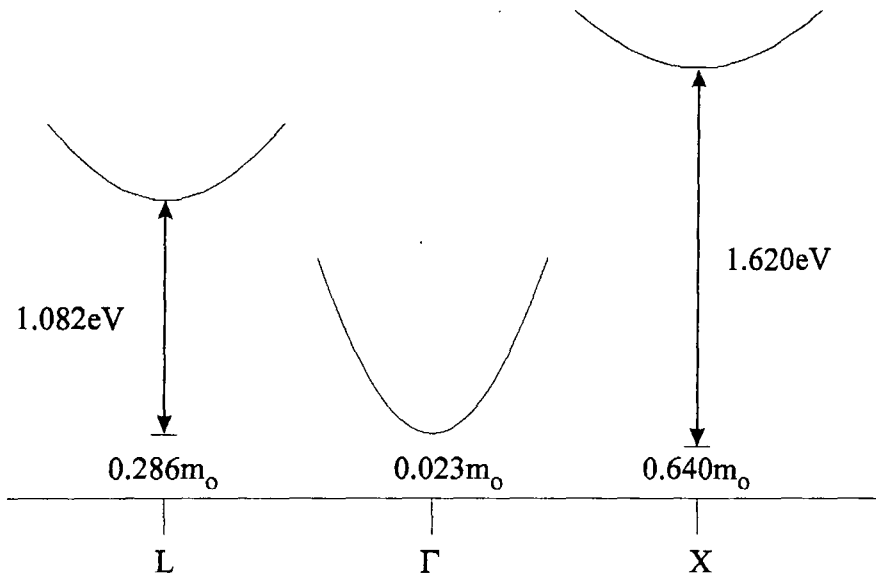
Figure 2.2

The energy separations and effective masses of the conduction

band valleys in InAs.
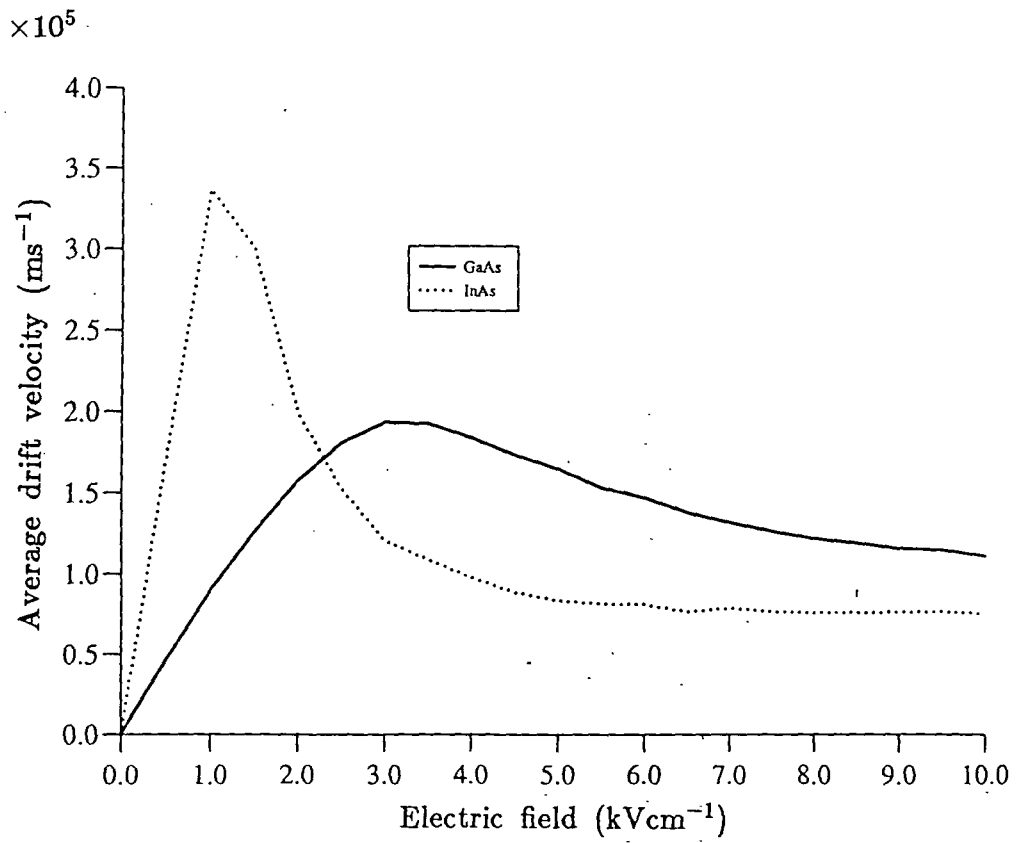
Figure 2.3

Mean electron drift velocity as a function of

applied electric field in GaAs and InAs.

GaAs. These results are in good agreement with experiments (see for example, Landolt & Börnstein 1982, Masselink 1989) and other Monte-Carlo simulations (see for example, Brennan & Hess 1984, Littlejohn *et al* 1977).

2.3.3 Transient behaviour

The transient responses of carriers in InAs and GaAs to a step function electric field were simulated using the ensemble method. The results for different field strengths are shown in figures 2.4 and 2.5. For the higher applied fields the velocity rises to a peak before falling to its steady state value. This is the well known and much studied velocity overshoot effect (see for example Glisson *et al* 1982 or Ghosal *et al* 1984) which is due to the electrons being able to attain a high non-equilibrium average velocity before the scattering has had time to impose the steady state.

The results of figure 2.4 and 2.5 show that the peak velocity also increases with field, exceeding $2.5 \times 10^6 \text{ms}^{-1}$ in InAs with a field of 20.0kVcm^{-1}. For both InAs and GaAs the equilibrium velocities, which are achieved by 5.0ps in almost all cases, agreed well with those obtained with the steady state model as would be expected.

Our average drift velocity results for GaAs show very good agreement with those from the Monte-Carlo simulations of Glisson *et al* 1982.
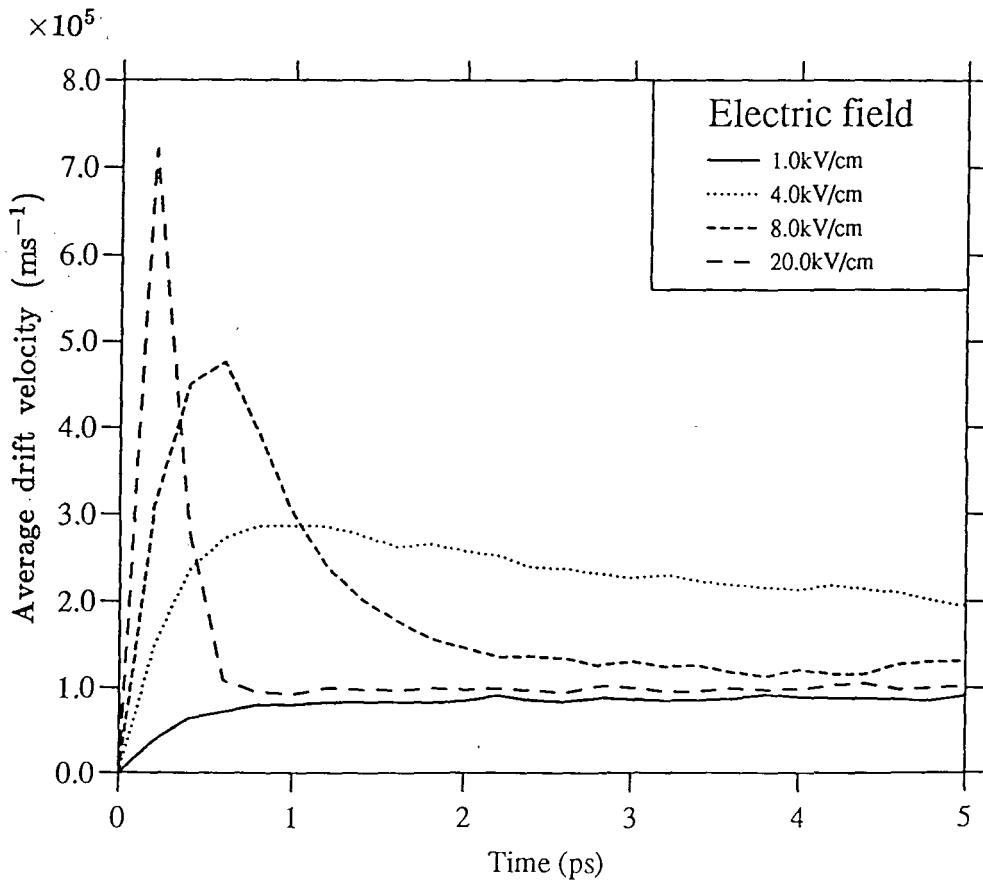
Figure 2.4

Mean electron drift velocity as a function of

time for different electric fields in GaAs.
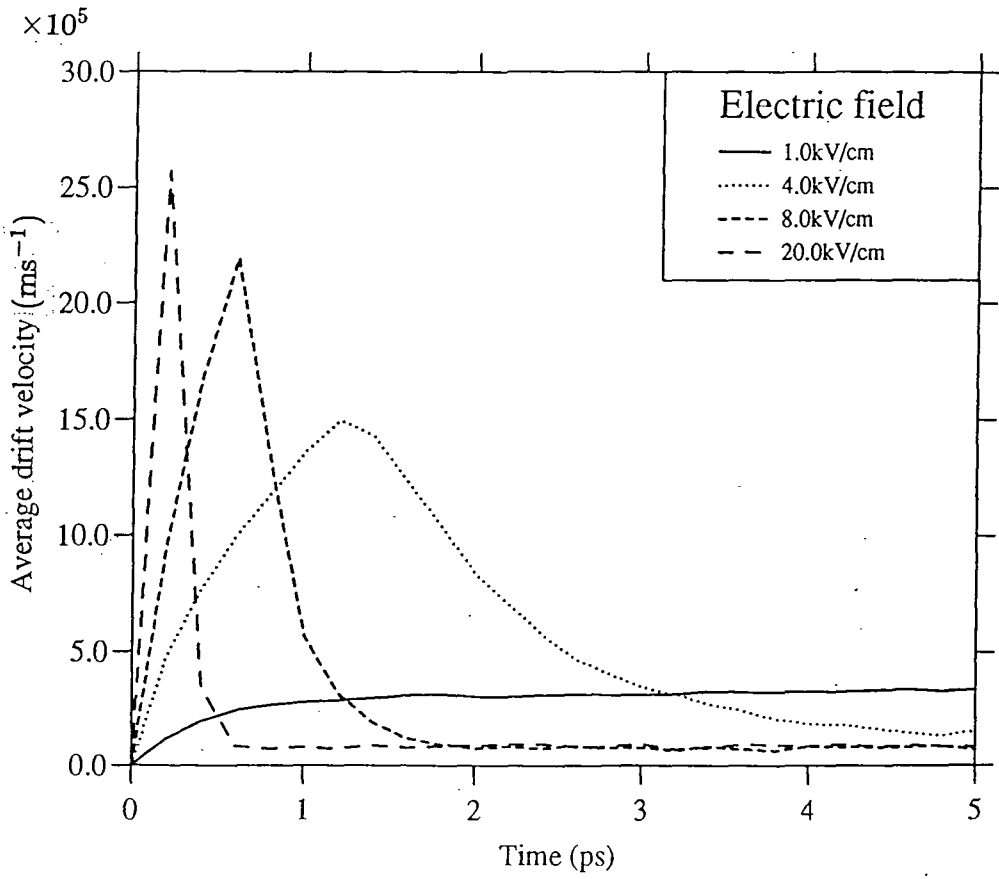
Figure 2.5

Mean electron drift velocity as a function of

time for different electric fields in InAs.

2.4   Ternary alloys.

$\mathcal{T}$o simulate electron transport in alloys it is necessary to include alloy scattering in the transport model. For the ternary alloy $A_x B_{1-x} C$ the C atoms occupy all the sites of one type in the zinc blende crystal. The other atoms, A and B, are distributed in some way on the other sites. In an ideal alloy system the A and B atoms would each be arranged regularly and periodically throughout the lattice. However, this is generally not the case, and they are distributed in some other way. One possibility is that large clusters of A and B atoms are found throughout the lattice with hardly any mixing between them, whilst another is that there is no correlation between atoms and the distribution of A and B atoms is totally random. We have made the assumption that the distribution of A and B atoms is totally random. Thus, although there is a periodic lattice in a random alloy the crystal potential is actually non-periodic because of the chemical disorder.

A simple model of the electronic structure of the random alloy is based on the virtual crystal approximation. This amounts to replacing the potential due to the A and B atoms by some average and so recovering a periodic system for the purposes of calculating band stucture. However the difference between the actual and virtual crystal potentials scatters the Bloch waves, and must be included in the simulation of carrier transport. The alloy scattering is in addition to the scattering mechanisms present in elements and compounds which do not have this chemical disorder. In this

model the alloy disorder is considered to be produced by a set of short range scatterers (Harrison & Hauser 1976). If the A and B atoms are arranged randomly without any correlation the alloy scattering rate, P_{alloy}, is (Harrison & Hauser, 1976, Asch & Hall, 1963, Littlejohn *et al* 1978),

$$P_{alloy} = \frac{3\sqrt{2}\pi m^{*\frac{3}{2}} x(1-x)(\Delta U)^2}{16 N \hbar^4} \epsilon^{\frac{1}{2}}. \qquad 2.1$$

In equation 2.1 m^* is the effective mass of the valley occupied by the electron, x is the concentration of A atoms in the alloy, ϵ is the electron energy, ΔU the magnitude of the short range scattering potential associated with each site, and N is the density of sites available to the A and B atoms (four in each cubic unit cell). There is no firm agreement on how ΔU should be derived or determined. For example, one approach is to use the difference in the value of the band gaps of the associated binary compounds (Littlejohn *et al* 1978), whilst another is to use the differences in their electron affinities (Harrison and Hauser 1976). Other workers have fitted values to experimental transport data to obtain a value of 0.42eV (Marsh *et al* 1981, Basu & Nag 1983).

Because of the large number of alloys available, each with a continuous range of compositions, the bandstructure and related parameters are generally not available from experiment. Interpolation between the end point binary material is normally used to obtain bandstructure and scattering parameters (Adachi 1982 & 1985, Marsh *et al* 1981, and Harrison & Hauser 1976). The values of most interest are the conduction band valley separations and their effective masses. We have used linear interpolation

for these parameters. Although the mass values may be calculated using a quadratic instead of a linear interpolation the bowing factor parameters are not reliably known at present. (Inclusion of a bowing factor in calculating the effective masses would alter the values from those used here and so have a corresponding effect on the velocities of the electrons; slower for larger masses, faster for lower ones.) For the effective masses $(m^*(x))$

$$m^*(x) = x m^*_{AC} + (1 - x) m^*_{BC} \qquad \qquad 2.2$$

and for the inter-valley separations $(\Delta E_{\Gamma L} \text{ and } \Delta E_{\Gamma X})$

$$\Delta E_{\Gamma i}(x) = x \Delta E_{\Gamma i AC} + (1 - x) \Delta E_{\Gamma i BC} \quad i = L \text{ or } X \qquad 2.3$$

The ternary III-V alloys such as $In_x Ga_{1-x} As$ are known to have two modes of lattice vibration with frequencies close to those of the individual binary materials (Chen *et al* 1966, Veleur & Barker 1966). The strength of these modes is dependent on the alloy composition (Kim & Spitzer 1979). The theory of this two mode behaviour of alloys has been discussed by many authors (Chang & Mitra 1970, Nash *et al* 1987, Verleur & Barker 1966) but we have found no satisfactory model to calculate scattering rates for materials with this two mode behaviour. We have therefore taken the common procedure in transport calculations, which is to model the lattice vibrations in terms of one mode with an effective phonon frequency. In this approach the effective longitudinal optical phonon frequency for the alloy $(\omega_{LO}^{eff}(x))$ is defined as (Adachi 1985)

$$\omega_{LO}^{eff}(x) = x \omega_{LO}^{AC}(x) + (1 - x) \omega_{LO}^{BC}(x) \qquad \qquad 2.4$$

where $\omega_{LO}^{AC}(x)$ and $\omega_{LO}^{BC}(x)$ are the AC-like and BC-like lattice vibration modes of the alloy.

Transport in $In_{0.53}Ga_{0.47}As$ has been extensively studied theoretically (Littlejohn *et al* 1978, Ahmed *et al* 1985 Harrison & Hauser 1976) and experimentally (Windhorn *et al* 1982, Marsh *et al* 1981) and is therefore a useful test of our simulation model. In the next section we describe the results of our transport simulations and compare these with published work and the results for GaAs reported in section 2.3.

2.5   Simulation of transport in bulk $In_{0.53}Ga_{0.47}As$.

*B*ecause $In_{0.53}Ga_{0.47}As$ is lattice matched to InP, it has been grown in thick layers and the electron drift velocity for bulk samples determined experimentally.

The important parameters used in the simulations are listed in table 2.1 and have been calculated using equations 2.2, 2.3, and 2.4.

The Monte-Carlo programs have been used to calculate both steady state and transient transport of electrons in the $In_{0.53}Ga_{0.47}As$ alloy. The steady state model has been used to calculate the effects of different values of the alloy scattering potential ΔU. The value of ΔU fitted to experiment was then used in the ensemble program to simulate the transient response

to a step function electric field applied at time t=0.

Γ valley effective mass $(m_\Gamma^*(0.53))$	$0.0437m_o$
L valley effective mass $(m_L^*(0.53))$	$0.26m_o$
X valley effective mass $(m_X^*(0.53))$	$0.612m_o$
Γ to L separation $(\Delta E_{\Gamma L}(0.53))$	$0.723eV$
Γ to X separation $(\Delta E_{\Gamma X}(0.53))$	$1.104eV$
GaAs-like phonon energy $\hbar\omega_{LO}^{GaAs}(0.53)$	$34meV$[†]
InAs-like phonon energy $\hbar\omega_{LO}^{InAs}(0.53)$	$29meV$[†]
Effective phonon energy $\hbar\omega_{LO}^{eff}(0.53)$	$31meV$

Table 2.1

Parameters used in bulk $In_{0.53}Ga_{0.47}As$ simulation

[†] from Nash *et al* 1986

2.5.1 Steady state simulation

The effects of different values of ΔU on the transport of electrons in bulk $In_{0.53}Ga_{0.47}As$ using the single particle Monte-Carlo program have been compared. Consideration has been given to $\Delta U = 1.08eV$, obtained from the difference in electron affinity of InAs and GaAs (from Littlejohn *et al* 1978), $\Delta U = 0.83eV$ from the difference in band gap (from Harrison & Hauser 1976) and $\Delta U = 0.42eV$ which has been shown (Marsh *et al* 1981) to be a good fit to experiment. It is useful to separate the scattering effects of alloying from those derived from the bandstructure effects and the case in which no alloy scattering is present (effectively $\Delta U = 0.0eV$) has also

been examined.

The results of the transport simulations are shown in figure 2.6. The general trend in the velocity-field curves is a reduction of the drift velocity with increased alloy scattering potential. This is expected as an increase in alloy potential increases the total scattering rate and decreases the electron free flight time. The occupancy of the L valleys versus electric field presented in figure 2.7, shows that as the alloy potential is increased, a larger field is needed to achieve a given level of L valley population. This can also be explained by the reduction of the time between collisions. As the free flight time falls the energy gained in this time decreases, and so a higher field is needed for the electron to attain the energy at which scattering to the L valleys becomes possible. A direct consequence of this is that the electron population in the Γ valley at any given field increases with alloy scattering strength and results in the shift of the peak velocity to higher fields seen in figure 2.6.

Table 2.2 compares the low field mobilities for different values of ΔU with that for GaAs.

If we compare the transport results for GaAs with those for $In_{0.53}Ga_{0.47}As$ with $\Delta U = 0.00eV$ we see the effect due to the changes in bandstructure and material parameters from alloying alone. As expected, the alloy has a greater low field mobility and higher peak velocity which is in turn because it has a lower Γ valley effective mass and a larger $\Delta E_{\Gamma L}$. The alloy also has a lower saturation velocity due to its larger satellite valley
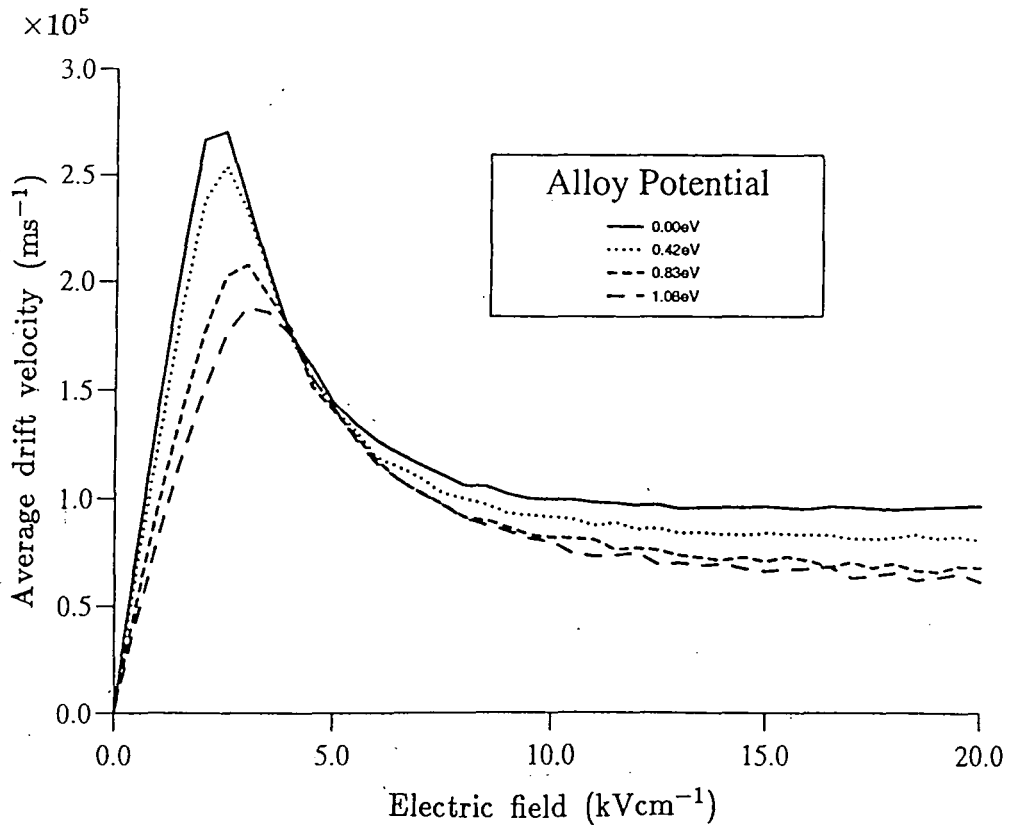
Figure 2.6

Mean electron drift velocity versus electric field

for different alloy scattering potentials in bulk $In_{0.53}Ga_{0.47}As$
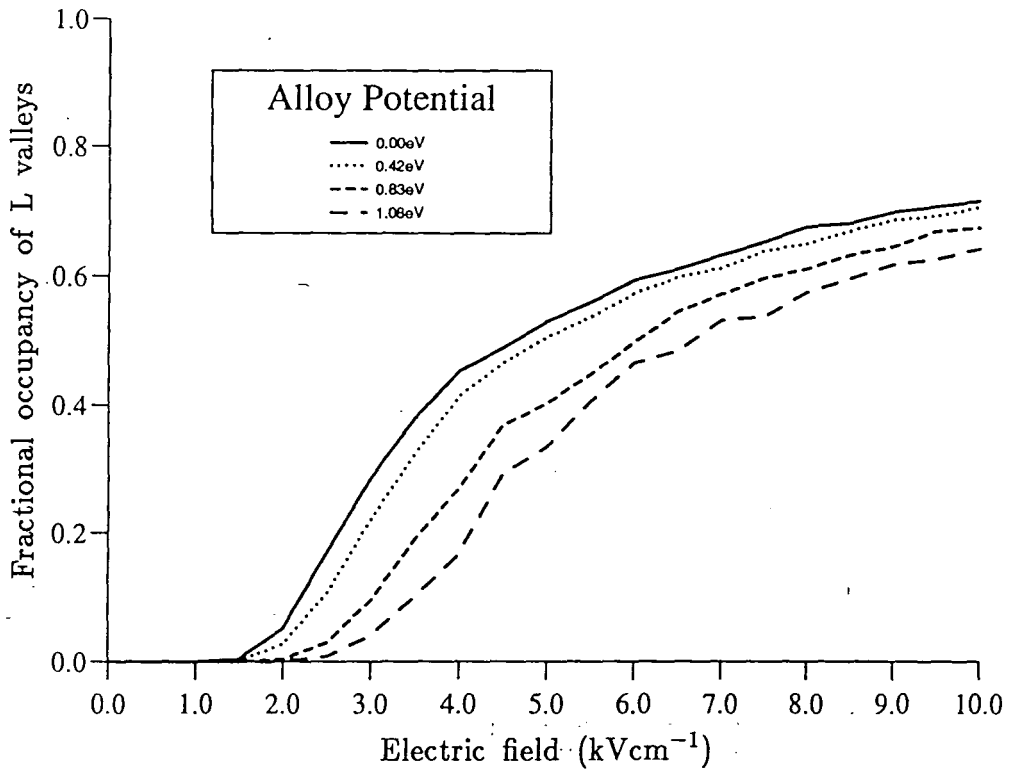
Figure 2.7

Fractional occupancy of L valleys versus electric field

for different alloy scattering potentials in bulk $In_{0.53}Ga_{0.47}As$

effective masses. As ΔU increases the positive effect introduced from the changes in bandstructure and other material parameters is negated somewhat, but only for the higher values of ΔU (0.83eV & 1.08eV) considered do we see a lower peak velocity, and for $\Delta U = 1.08$eV alone a lower mobility, than in GaAs.

ΔU (eV)	0.00	0.42	0.83	1.08	GaAs
μ $(m^2V^{-1}s^{-1})$	1.46	1.22	0.97	0.81	0.9
Peak velocity $(\times 10^5 ms^{-1})$	2.7	2.5	2.1	1.8	2.2

Table 2.2

Comparison of the low field mobility, μ, and peak velocity

for GaAs and $In_{0.53}Ga_{0.47}As$ with different values of ΔU

Comparison of low field mobilities and saturation velocities reported in the literature show significant variation between sources. However, the results presented here show a good agreement with the Monte-Carlo simulation work of Brennan & Park 1989, and Thobel *et al* 1990, and the experimental and Monte-Carlo results reported by Marsh *et al* in 1981, Littlejohn *et al* in 1978 and Windhorn *et al* in 1982, for $\Delta U = 0.42$eV. We have therefore taken $\Delta U = 0.42$eV to simulate the transient behaviour of $In_{0.53}Ga_{0.47}As$ which is described in the next section.

2.5.2 Transient behaviour of $In_{0.53}Ga_{0.47}As$

Figure 2.8 shows the mean drift velocity of electrons in $In_{0.53}Ga_{0.47}As$
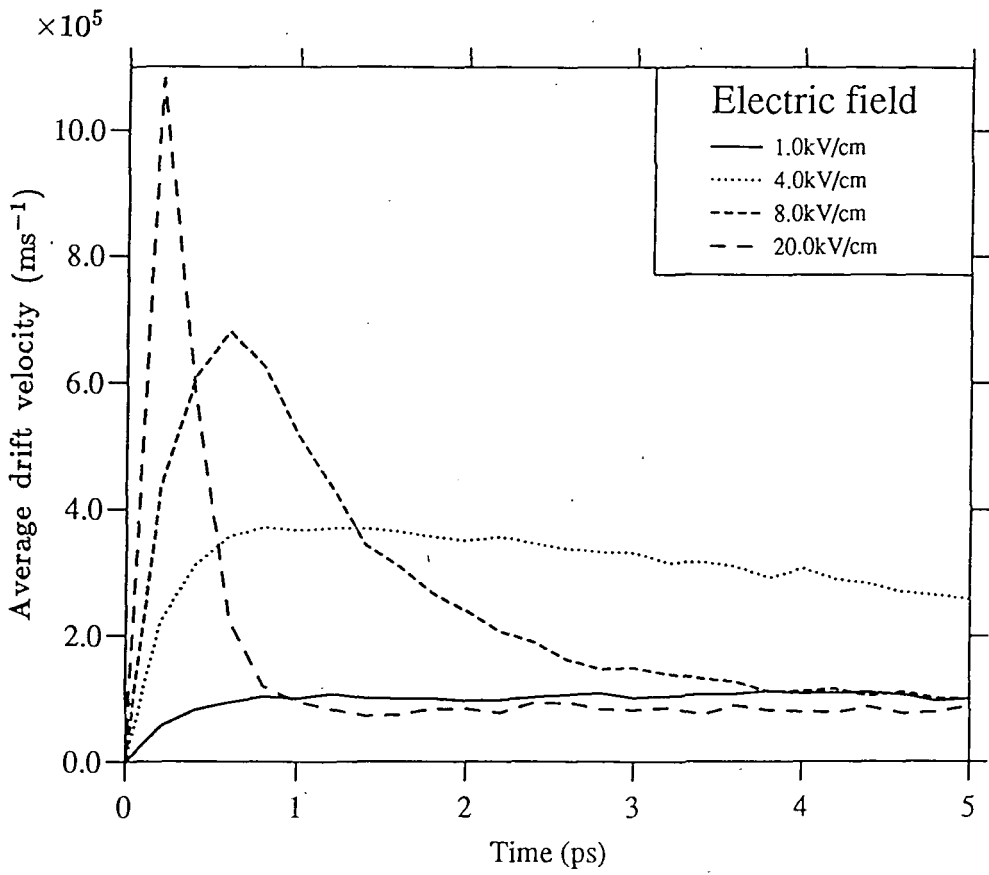
Figure 2.8

Mean electron drift velocity as a function of time

for different electric fields in bulk $In_{0.53}Ga_{0.47}As$

with an alloy scattering potential = 0.42eV.

when the material is subjected to an electric field switched on at t=0.0. The results are qualitatively similar to those for GaAs and InAs.

The ensemble simulation results show good agreement with the theoretical calculations of Ghosal *et al* 1984, with a peak in the velocity-time curve at about 0.15 ps. for a field of 20.0kVcm^{-1}.

2.6   Strain effects.

*A*s mentioned in section 2.1 $In_x Ga_{1-x} As$ (normally $x \leq 0.25$) is used as the conducting channel in some strained high electron mobility transistors (HEMTs) based on GaAs technology. The layers for such devices are produced by epitaxial growth on a GaAs substrate. Although $In_x Ga_{1-x} As$ has a larger lattice constant than GaAs, the channel in the HEMT is made sufficiently thin (≤ 150Å) that its growth is pseudomorphic. That is, the in-plane lattice constant of the alloy layer adjusts to that of the GaAs substrate (with no dislocations or other defects at the interface) and there is an accompanying expansion of the alloy lattice in the growth direction. Of interest here is the effect the strain has on the bandstructure and other material parameters which determine the electronic transport properties of the material.

Hence we have a system in which the transport properties are

influenced by both alloying and strain. In fact we should also recognise the effects of confinement of the electron in the thin layer, including quantum size effects. However, we delay consideration of the latter to isolate the effects of strain achieved by alloying. To do this we consider a case which is physically unrealistic but nevertheless instructive; electron transport in a bulk sample which is strained as if it were a pseudomorphic layer.

This following discussion on the effects of strain on the conduction band is based on the model solid theory of C. G. Van de Walle, 1989. We shall refer to the strained alloy as the layer material, and the material that determines the amount of strain as the substrate material. A quantity is described as *in-plane* when it is parallel to the imaginary interface between the layer material and the substrate. Similarly a quantity is *perpendicular* when it is normal to this interface.

The strain in the layer is defined in terms of the lattice constants of the bulk layer and substrate materials (a_l and a_s) and the elastic constants of the layer material (c_{11} and c_{12}). The in-plane strain $\epsilon_{\parallel}$ $(= \epsilon_{xx} = \epsilon_{yy})$ is defined for the layer

$$\epsilon_{\parallel} = \frac{a_s}{a_l} - 1, \qquad\qquad 2.5$$

and the perpendicular strain $\epsilon_{\perp}(= \epsilon_{zz})$ thus

$$\epsilon_{\perp} = -2\frac{c_{12}}{c_{11}}\epsilon_{\parallel} = -\frac{2\sigma}{1-\sigma}\epsilon_{\parallel}, \qquad\qquad 2.6$$

where σ is Poisson's ratio.

The strain tensor can be thought of as having isotropic $(\epsilon_{xx}+\epsilon_{yy}+\epsilon_{zz})$ and uniaxial $(\epsilon_\perp - \epsilon_\parallel)$ parts. The isotropic part has the same effect as an applied hydrostatic pressure, defined as

$$P = -B\frac{\Delta\Omega}{\Omega}, \qquad\qquad 2.7$$

where B is the bulk modulus of the alloy $(= -(c_{11} + 2c_{12})/3)$ and $\Delta\Omega/\Omega$ is the fractional volume change $(= \epsilon_{xx} + \epsilon_{yy} + \epsilon_{zz})$. A consequence of this hydrostatic pressure is a shift in the energies of the valley minima away from their unstrained positions. The Γ and L valleys increase in energy, at different rates, $(\frac{\partial E_\Gamma}{\partial P} = 10.73 meVkBar^{-1}$ and $\frac{\partial E_L}{\partial P} = 5.58 meVkBar^{-1}$ for GaAs, Landolt & Börnstein 1982) and the X valleys are lowered in energy $(\frac{\partial E_X}{\partial P} = -1.34 meVkBar^{-1}$ for GaAs, Landolt & Börnstein 1982).

The uniaxial part of the strain lowers the lattice symmetry with the consequences that the Γ valley becomes anisotropic in k-space and the X valleys are split in energy.

For growth along the (100) direction the six-fold degenerate X valleys are split into a four-fold quadruplet and a two-fold pair with the weighted mean energy of the valleys remaining unchanged. The energy splitting of the X valleys $(\Delta E_{X2X4} = E_{X2} - E_{X4})$ is obtained using the deformation potential, Φ_u, as

$$\Delta E_{X2X4} = \Phi_u(\epsilon_\perp - \epsilon_\parallel). \qquad\qquad 2.8$$

Φ_u was calculated using a linear interpolation between the values of Φ_u of GaAs and InAs (8.61eV and 4.5eV respectively, Van de Walle 1989)

We have used the GaAs values for the rate of change of the valley separations in the conduction band of the alloys. This is a reasonable approximation as the percentage of indium in the materials considered is small.

For growth along the (100) direction the L valleys are not split by the uniaxial component of the strain as they all have equivalent alignments to the substrate/layer interface.

The strain causes the Γ valley to become anisotropic. The constant energy surfaces are ellipsoids of revolution with different effective masses perpendicular and parallel to the substrate/layer interface. The perpendicular and parallel effective masses were calculated using an 8 band $\mathbf{k} \cdot \mathbf{p}$ program, supplied by colleagues G. C. Crow and M. Walmsley, which calculates the bulk bandstructure of strained III-V semiconductors.

2.7 Simulations of transport in strained $In_x Ga_{1-x} As$.

$\mathcal{T}$o study the effects of alloy composition and strain on the electron transport properties of bulk $In_x Ga_{1-x} As$ we have used the single particle Monte-Carlo program to simulate the five alloy compositions x = 0.05, 0.10, 0.15, 0.20 and 0.25. In particular, simulations have been carried out for the unstrained alloy, corresponding to bulk material where the changes in bandstructure are entirely due to compositional effects; and for the strained material corresponding to a pseudomorphic layer on a GaAs substrate. In the latter case both electric fields applied perpendicular and parallel to the substrate/layer interface are considered.

Figure 2.9 shows the velocity-field characteristics of the $x = 0.15$ alloy with and without strain. It is apparent that the strained material has a smaller low field mobility and peak velocity than the unstrained material but the saturation velocity is greater. The electron velocity is generally lower for an electric field perpendicular to the substrate/layer interface but there is no significant difference between the saturation velocities for the two field directions.

The low field mobilities and peak velocities are compared with GaAs in table 2.3. The results of figure 2.9 and table 2.3 can be explained with reference to the bandstructure of the materials and the relative carrier occupancy of the conduction band valleys.

Table 2.4 shows the effects on the Γ valley effective masses in both

	Unstrained		Strained			
			Parallel field		Perpendicular field	
Indium concentration	Mobility μ $(\text{m}^2\text{V}^{-1}\text{s}^{-1})$	Peak Velocity $(\times 10^5 \text{ms}^{-1})$	Mobility μ $(\text{m}^2\text{V}^{-1}\text{s}^{-1})$	Peak Velocity $(\times 10^5 \text{ms}^{-1})$	Mobility μ $(\text{m}^2\text{V}^{-1}\text{s}^{-1})$	Peak Velocity $(\times 10^5 \text{ms}^{-1})$
0%	0.90	1.94	0.90	1.94	0.90	1.94
5%	0.89	1.98	0.87	2.00	0.84	1.98
10%	0.88	2.03	0.82	2.01	0.78	1.97
15%	0.95	2.22	0.83	2.04	0.75	1.96
20%	0.96	2.26	0.81	2.11	0.71	1.97
25%	0.99	2.30	0.83	2.20	0.70	2.03

Table 2.3

Effect of alloy composition and strain on the mobility and peak velocity of $\text{In}_x\text{Ga}_{1-x}\text{As}$.

(Fluctuations in the general trend of the values are due to statistical errors in the method.)

$\times 10^5$
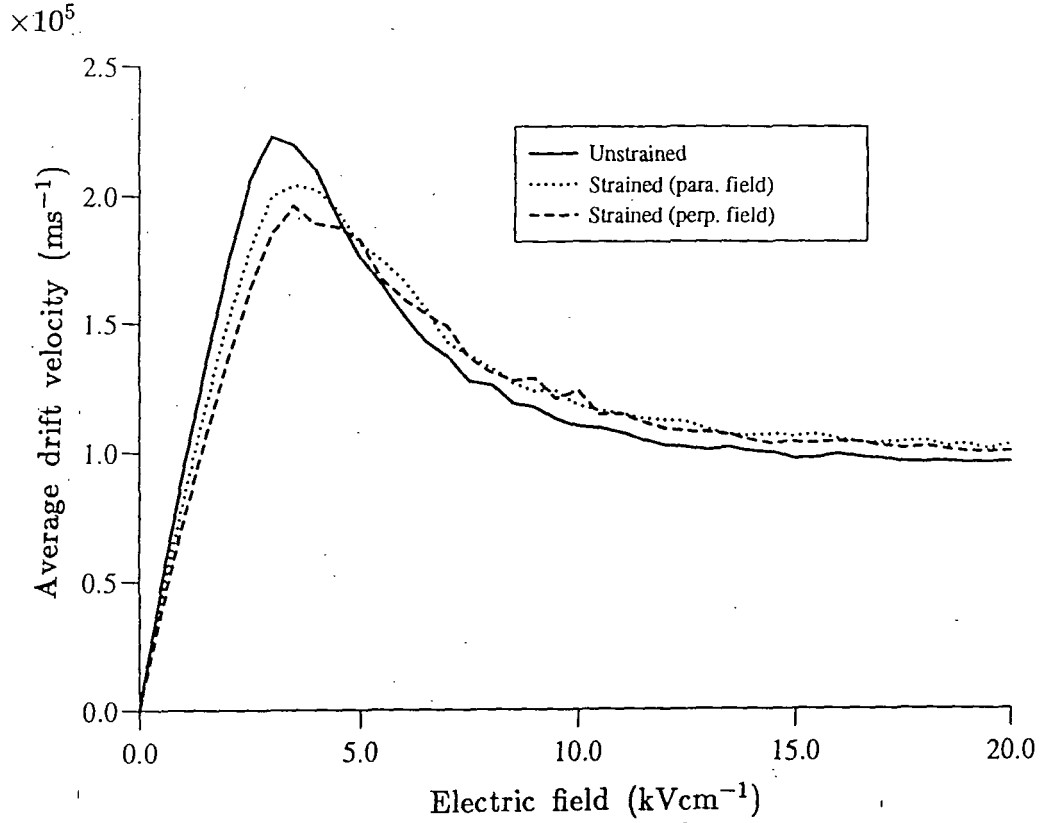
Figure 2.9

Mean electron drift velocity versus electric field for $In_{0.15}Ga_{0.85}As$ with and without strain. In the strained case the strain is appropriate to a pseudomorphic layer on a GaAs substrate, and field directions parallel and perpendicular to the substrate/layer interface are considered.

the parallel and perpendicular directions as predicted by a $\mathbf{k} \cdot \mathbf{p}$ bandstructure calculation. The Γ valley effective mass of the strained material is anisotropic with an in-plane component $(m_\parallel^*)$ which is lighter than the perpendicular component $(m_\perp^*)$. Both effective masses, $m_\parallel^*$ and $m_\perp^*$, increase with strain but at different rates. The other influence to consider is the direct effect of the indium on the effective mass, so that unstrained InGaAs has a lower mass than GaAs. The net result of compositional and strain effects is for $m_\parallel^*$ to be smaller, and $m_\perp^*$ to be greater than the isotropic mass of unstrained GaAs.

Indium concentration	Compressive strain (%)	Unstrained effective mass m^*	Strained	
			Parallel effective mass $m_\parallel^*$	Perpendicular effective mass $m_\perp^*$
5%	0.42	$0.065 m_o$	$0.066 m_o$	$0.068 m_o$
10%	0.77	$0.063 m_o$	$0.066 m_o$	$0.069 m_o$
15%	1.13	$0.060 m_o$	$0.064 m_o$	$0.071 m_o$
20%	1.48	$0.058 m_o$	$0.063 m_o$	$0.072 m_o$
25%	1.83	$0.056 m_o$	$0.062 m_o$	$0.075 m_o$

Table 2.4

Effect of alloy composition and strain on the

Γ valley effective mass of $In_x Ga_{1-x} As$

The changes in the effective mass have a direct effect on the low field mobility. It is known that as the effective mass of the Γ valley increases,

the low field mobility reduces which explains why as seen in figure 2.10, the unstrained material always has a greater low field mobility, than the strained material. When the field is applied parallel to the interface between the layer and the substrate materials, the effective mass is smaller than in the perpendicular direction, and the mobility is correspondingly higher. It is apparent from table 2.3 and figure 2.10 that the strain (coupled with alloy scattering) reduces the low field mobility to less than that of bulk GaAs (x=0.0).

Table 2.5 shows the conduction band valley separations of the strained and unstrained alloys. As the strain increases the energy separations between the Γ valley and the L and X valleys decrease, compensated to some degree by the increase in the valley separation due to the increase in indium concentration. The strain effects in the conduction band give a general reduction of the peak velocity is shown in figure 2.11. This decrease is a result of two main effects. First, the increase in the Γ valley effective mass makes the resident electrons less mobile, and second, the decrease in the Γ to L valley separation means the electrons are able to scatter into the L valleys at lower energies.

The relative occupancy of the valleys versus electric field for $In_{0.15}Ga_{0.85}As$ is shown in figure 2.12. The strained material has a greater fraction of carriers in the Γ valley than the unstrained materials for the larger fields and although other cases are not shown here, this behaviour is common to all alloy compositions considered. This is due to the larger
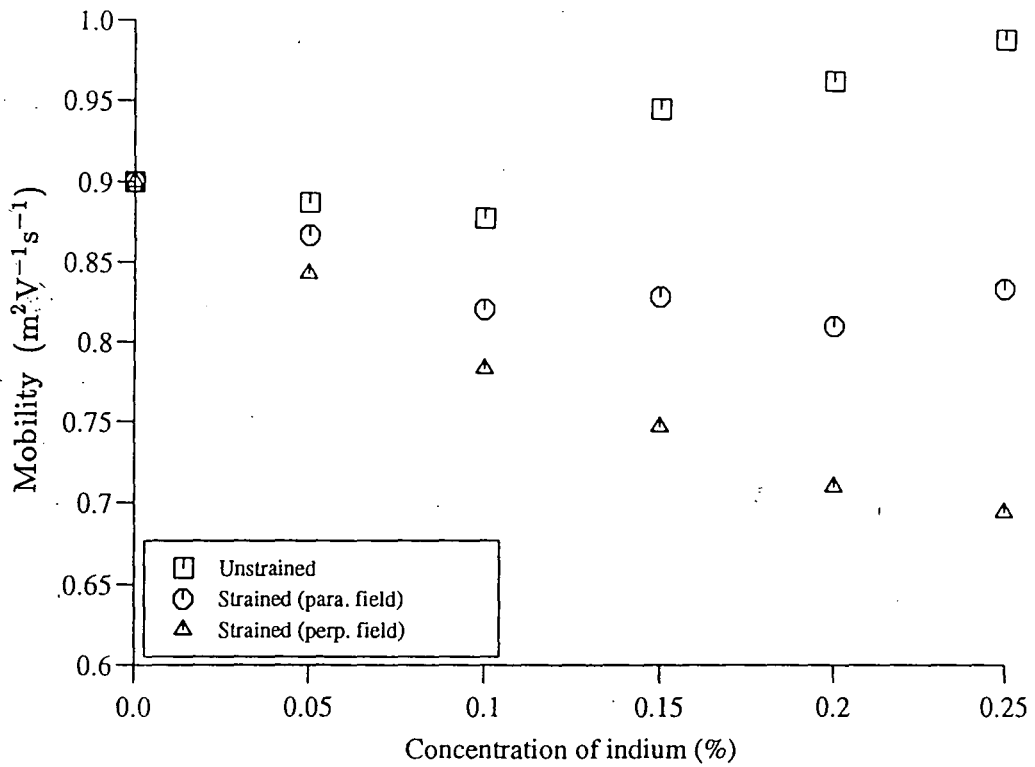
Figure 2.10

Electron mobility as a function of indium concentration (x) in bulk $In_x Ga_{1-x} As$. Both unstrained and strained materials, with electric fields in the parallel and perpendicular directions in the latter case, are considered.

Figure 2.11

Peak electron velocity as a function of indium concentration (x) in bulk $In_x Ga_{1-x} As$. Both unstrained and strained materials, with electric fields in the parallel and perpendicular directions in the latter case, are considered.
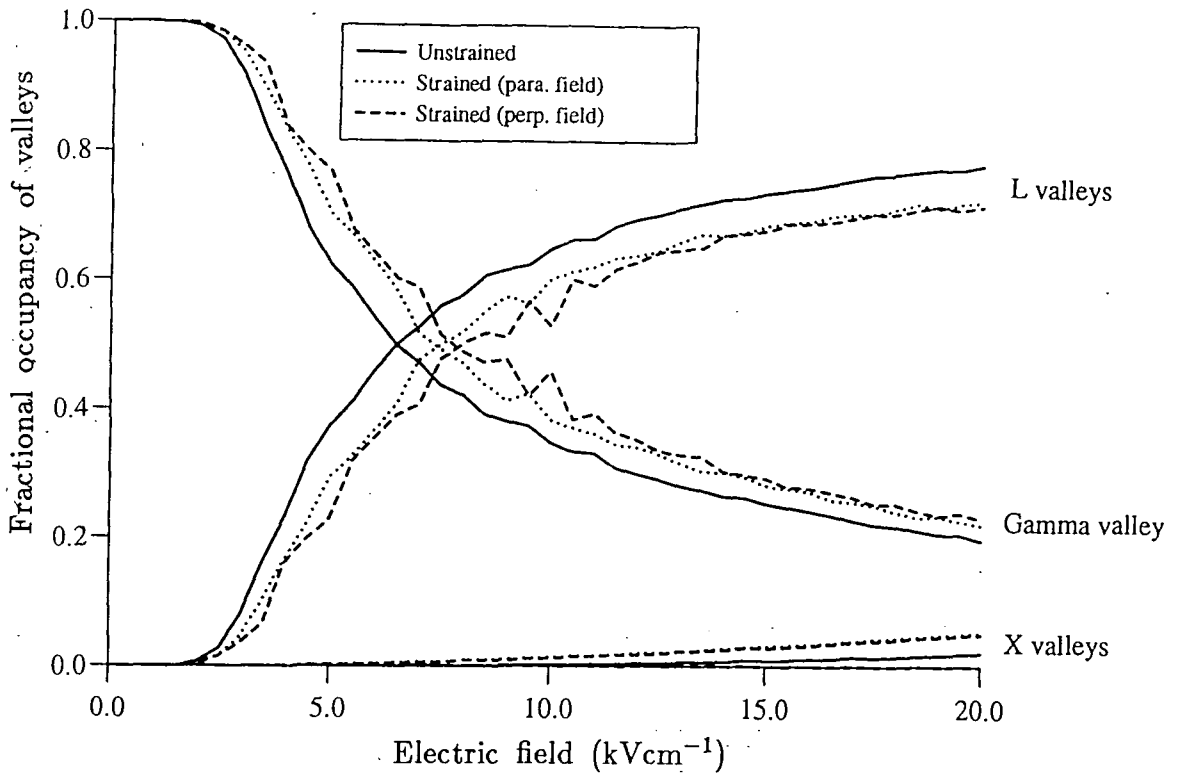
Figure 2.12

Fractional occupancy of conduction band valleys in bulk $In_{0.15}Ga_{0.85}As$ with and without strain. Electric fields parallel and perpendicular to the layer/substrate interface are considered for the strained alloy.

Γ valley effective masses in the strained material inhibiting electron heating

and transfer to the satellite valleys. Although the Γ valley effective mass is

larger in the strained material the electrons in the Γ valley of the strained

material are more mobile than in the satellite valleys of the unstrained (or

strained) material. As a result, the higher fraction of carriers in the Γ valley

of the strained material gives the higher average saturation velocity seen in

figure 2.13.

	Unstrained		Strained		
Indium concentration	$\Delta E_{\Gamma L}$ eV	$\Delta E_{\Gamma X}$ eV	$\Delta E_{\Gamma L}$ eV	$\Delta E_{\Gamma X4}$ eV	$\Delta E_{\Gamma X2}$ eV
5%	0.367	0.577	0.354	0.536	0.586
10%	0.405	0.632	0.377	0.546	0.652
15%	0.442	0.687	0.400	0.558	0.717
20%	0.479	0.742	0.424	0.571	0.781
25%	0.516	0.797	0.448	0.587	0.844

Table 2.5

Effect of strain on the conduction bandstructure of $In_x Ga_{1-x} As$

Figure 2.12 shows a small fraction of carriers in the X valleys. The

reduction in energy between the Γ and X valleys in the strained material is

more substantial than the change in Γ to L separation and results in a greater

fractional population in the X valleys of the strained material. Although

it is not indicated in the figure all the carriers reside in the X4 valleys
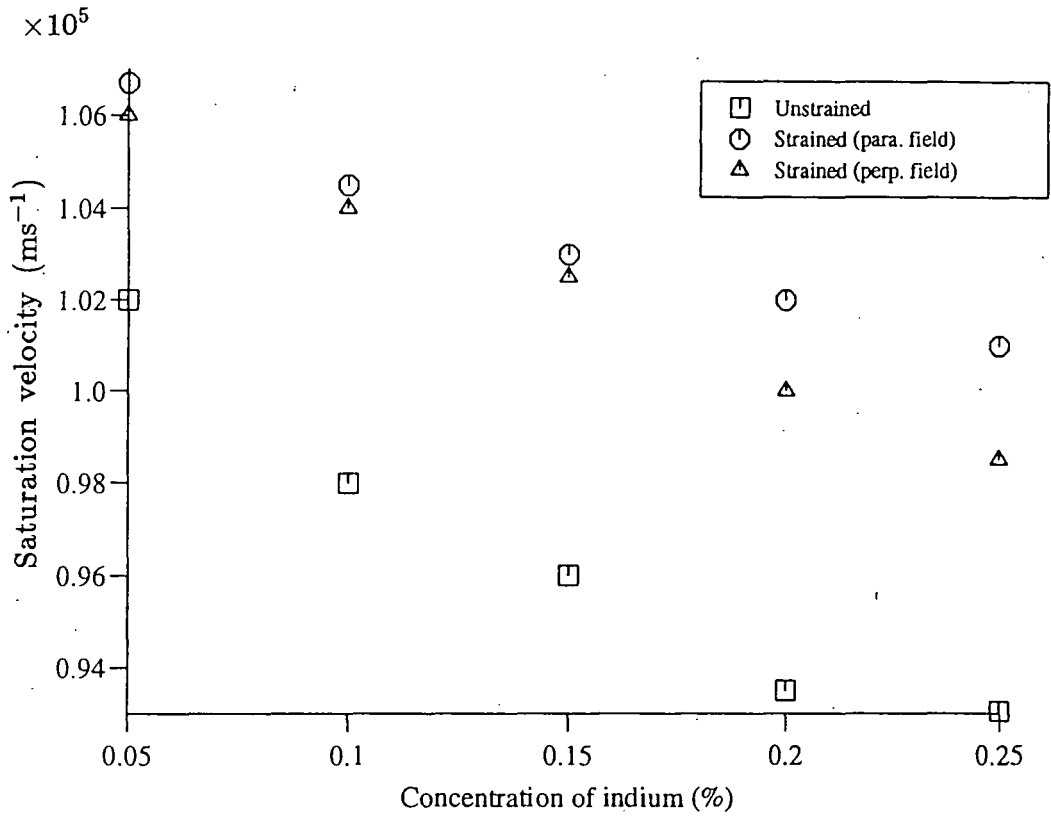
Figure 2.13

Saturation electron velocity as a function of indium concentration (x)

in bulk $In_x Ga_{1-x} As$. Both unstrained and strained materials,

with electric fields in the parallel and perpendicular directions
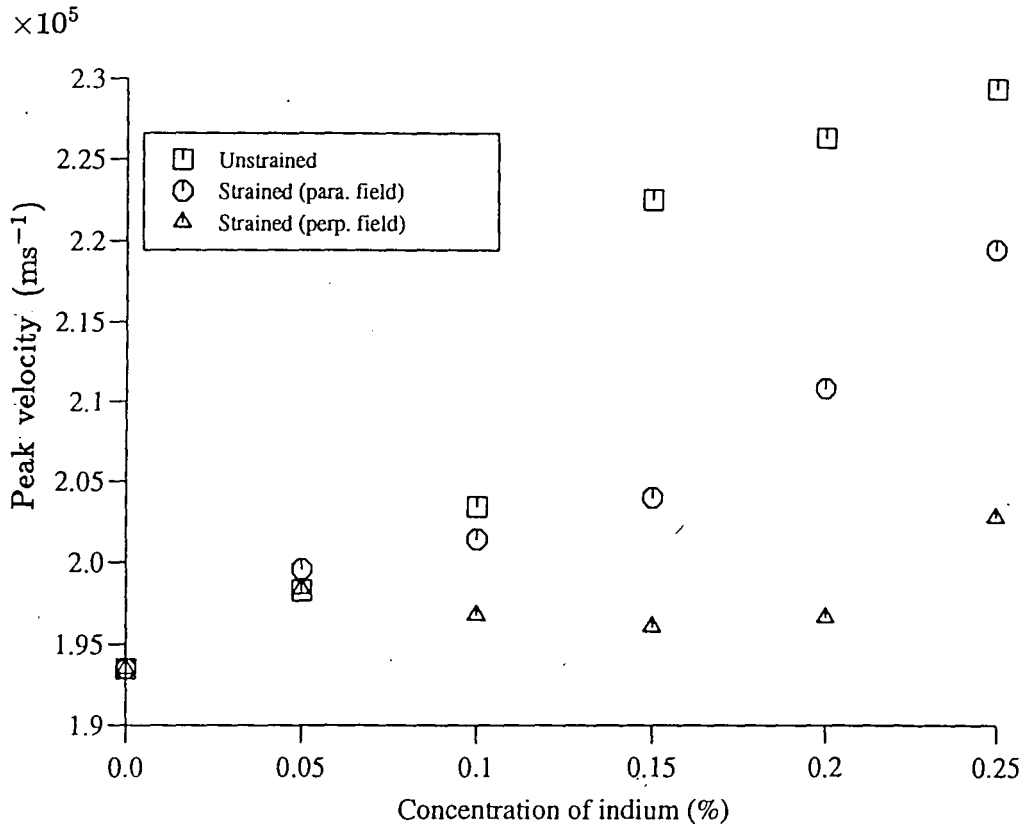
in the latter case, are considered.

because the large effective mass of the X valleys inhibits significant heating of resident carriers.

The results reported above are in good general agreement with those of Thobel *et al* 1990 but differ in that they found a decrease in the saturation velocity with strain. It is not possible to investigate this difference further because of the limited information provided on their model.

2.8   Summary & conclusions.

In this chapter we have introduced and examined the effects of alloy concentration and strain on the bandstructure and material parameters of bulk $In_xGa_{1-x}As$ (x= 0.00, 0.05, 0.10, 0.15, 0.20, 0.25, 0.53, and 1.00), and how this effects the transport properties, especially the average drift velocity, predicted by our Monte-Carlo simulation programs.

We found that, for $x = 0.53$, the alloy scattering potential ΔU had an important effect on the carrier velocity, as ΔU increased the scattering rate increased and the carrier velocity was reduced. However, for the most of the range of ΔU considered and especially the value fitted to experimental results $\Delta U = 0.42$ we found a higher low field mobility and increased peak velocity over that for GaAs, due to the smaller Γ valley effective mass and larger $\Delta E_{\Gamma L}$ in the alloy.

We have found that (with $\Delta U = 0.42$) increasing indium concentration, $(0.00 \leq x \leq 0.25)$,

[i] generally improved low field mobility, due to the smaller Γ valley effective mass,

[ii] increased the peak velocity, because of the larger value of $\Delta E_{\Gamma L}$,

[iii] reduced the saturation velocity, which we attributed to the larger satellite valley effective masses.

Strain had the effect of;

[i] reducing the low field mobility to values lower than GaAs, because of the increase in Γ valley effective mass with strain,

[ii] reducing the peak velocity below that of the unstrained material (but still larger than in GaAs), because of the general reduction in energy separation between satellite valleys.

[iii] increasing the saturation velocity, which was due to the higher percentage of carriers in the Γ valley.

References for chapter two.

Adachi S. 1982 *J. Appl. Phys.* **53** 8775

Adachi S. 1985 *J. Appl. Phys.* **58** R1

Adams A. R., Vinson P. J., Pickering C., Pitt G. D., and Fawcett W. 1977 *Electron. Lett.* **13** 46

Ahmed S. R., Nag B. R., and Deb Roy M. 1985 *Solid State Electron.* **28** 1193

Asch A. E. and Hall G. L. 1963 *Phys. Rev.* **132** 1047

Aspnes D. E. 1976 *Phys. Rev. B* **14** 5331

Basu P. K. and Nag B. R. 1983 *Appl. Phys. Lett.* **43** 689

Brennan K. F. and Hess K. 1984 *Solid State Electron.* **27** 347

Brennan K. F. and Park D. H., 1989 *J. Appl. Phys.* **65** 1156

Butcher P. N. 1973 *Electrons in Crystaline Solids* International Atomic Energy Agency, Vienna. p103.

Chang I. F. and Mitra S. S. 1970 *Phys. Rev. B* **2** 1215

Chen Y. S., Shockley W., and Pearson G. L. 1966 *Phys. Rev.* **151** 648

Fawcett W., Boardman A. D., and Swain S. 1970 *J. Phys. Chem. Solids* **31** 1963

Ghosal A., Chattopadhyay D., and Purkait N. N., 1984 *Appl. Phys. Lett.* **44** 773

Glisson T. H., Williams C. K., Hauser J. R., and Littlejohn M. A. 1982 *VLSI Electronics: Microstructure Science* **4** Academic Press, New York.

Harrison J. W. and Hauser J. R. 1976 *J. Appl. Phys.* **47** 292

Harrison J. W. and Hauser J. R. 1976 *Phys. Rev. B.* **13** 5347

Harrison W. A. 1956 *Phys. Rev.* **104** 1281

Jacoboni C. and Regiani L. 1983 *Rev. Mod. Phys.* **55** 645

Kim O. K. and Spitzer W. G. 1979 *J. Appl. Phys.* **50** 4362

Landolt-Börnstein 1982 *Numerical Data and Functional Relationships in Science and Technology* ed. O. Madelung, vol. III/17a. Springer-Verlag, Berlin.

Littlejohn M. A., Hauser J. R., and Glisson T. H. 1977 *J. Appl. Phys.* **48** 4587

Littlejohn M. A., Hauser J. R., Glisson T. H., Ferry D. K., and Harrison J. W. 1978 *Solid State Electron.* **21** 107

Marsh J. H., Houston P. A., and Robson P. N. 1981 *Proceedings of the 17th International Symposium on Gallium Arsenide and Related Compounds, Vienna 1980* Institute of Physics, London. p621.

Masselink W. T. 1989 *Semicond. Sci. Technol.* **4** 503

Moglestue C. 1993 *Monte Carlo Simulation of Semiconductor Devices* Chapman & Hall, London.

Nag B. R. 1972 *Theory of Electrical Transport in Semiconductors* Pergamon Press, Oxford.

Nash K. J., Skolnick M. S., and Bass S. J. 1987 *Semicond. Sci. Technol.* **2** 329

Thobel J. L., Baudry L., Cappy A., Bourel P., and Fauquembergue R. 1990 *Appl. Phys. Lett.* **56** 346

Van de Walle C. G. 1989 *Phys. Rev. B* **39** 1871

Verleur H. W. and Barker Jr. A. S. 1966 *Phys. Rev.* **149** 715

Windhorn T. H., Cook L. W., and Stillman G. E. 1981 *IEEE Elec. Dev. Lett.* **3** 18

CHAPTER THREE

A COMPARISON OF LOW FIELD ELECTRON TRANSPORT IN AN $Al_{0.3}Ga_{0.7}As$/GaAs QUANTUM WELL USING DIFFERENT PHONON MODELS.

3.1   Introduction.

$\mathcal{T}he$ electronic states of semiconductor heterostructures have been the subject of considerable attention in recent years but much less research effort has been devoted to the properties of the phonon states in these systems. Nevertheless microscopic models of lattice vibration in heterostructures have been developed and appear to provide a satisfactory description of the phonon states in a number of structures (see for example Molinari *et al* 1992, Ren *et al* 1989). Such models, dealing with the dynamics of the individual atoms or ions and involving large scale numerical calculations, are not the most appropriate to incorporate in theories of electron transport. They may, however, be used to compare with the ionic displacements, electron-phonon interactions, and scattering rates predicted by the simpler macroscopic con-

tinuum models, which describe the lattice vibrations in terms of an elastic continuum rather than being concerned with individual particles, and are more suitable for transport calculations, including Monte-Carlo simulation.

A number of continuum models have been developed to describe the optical phonon states present in heterostructure quantum wells. At the time this work was carried out the Dielectric Continuum Model (DCM), and related models (Huang & Zhu 1988, Haupt & Wendler 1991), based on the work of Fuchs and Kliewer (1965), were particularly prevalent but alternative approaches had been proposed including the Hydrodynamic Model (HDM) of Babiker and co-workers (Babiker 1986, Ridley 1989, Chamberlain 1987 & 1990). These two models approach the problem in different ways, the first is an electromagnetic treatment using standard boundary conditions between dielectrics of different permitivities, the second an electro-mechanical treatment of the lattice employing hydrodynamic boundary conditions. These two models predict different phonon modes, both of which have some inconsistencies when compared to the modes from microscopic models.

Recently developed continuum models, which are more in line with microscopic model calculations, are the so called Hybrid Models (Zianni *et al* 1992, Ridley *et al* 1993). These models include dispersion, realistic boundary conditions and more importantly allow coupling between confined and interface modes.

Another option in electron transport calculations is simply to ignore the effects of the heterostructures on the lattice vibrations and to assume the

phonon modes are the same as in a bulk sample of the well semiconductor (Riddoch & Ridley 1983, Ridley 1982, Price 1981). We called this the Bulk Phonon Approximation (BPA).

In collaboration with Dr. M. P. Chamberlain of the Max Planck Institute, Stuttgart, we have considered how each of the three phonon models (DCM, HDM & BPA) would affect parallel electron transport in a semiconductor quantum well (Chamberlain *et al* 1992). A comparison of the rates of electron scattering between subbands has been made and of the results of single particle Monte-Carlo simulations of parallel electron transport. A comparison with results predicted using Hybrid model phonon modes is not included as these models were not fully developed when this work was carried out.

We first describe the quantum well heterostructure, including its electron subbands. This is followed by a brief review of scattering processes in quantum wells and a description of each phonon model in sections 3.3 and 3.4 respectively. Section 3.5 compares the results obtained for each phonon model when Fermi's Golden Rule is used to calculate the electron-phonon scattering rates. The low field average drift velocity, electron energies, and a comparison of the number of phonon absorption and emission events obtained when these rates were included in a Monte-Carlo transport simulation are reported and discussed in section 3.6.

3.2 $Al_{0.3}Ga_{0.7}As/GaAs$ quantum well model.

$\mathcal{T}he$ system used to compare the effects of the different phonon models is the quantum well in the Γ valley formed by growing 70Å of GaAs between two semi-infinite layers of $Al_{0.3}Ga_{0.7}As$, as shown in figure 3.1. The parameters of the system are specified in table 3.1. Growth is along the (001) crystalographic direction for both well and barrier materials with perfectly smooth interfaces between them. The difference in lattice constant between $Al_{0.3}Ga_{0.7}As$ and GaAs is very small and we have taken them to be lattice matched ($a_0 = 5.66$Å for AlAs and, $a_0 = 5.65$Å for GaAs, Landolt & Börnstein 1982), and there are no effects on the band structure or other material parameters due to strain. The effective mass of GaAs (m_w^*) has been taken to be $0.063m_0$ (Littlejohn 1977) and the alloy mass (m_b^*) derived using a linear interpolation between values for AlAs $(0.146m_o)$ and GaAs (Casey & Panish 1978, Adachi 1985);

$$m_b^* = 0.063 + 0.083x \qquad\qquad 3.1$$

The Γ valley effective masses of AlGaAs and GaAs were assumed isotropic and wavevector independent.

The conduction band offset, which forms the confining potential well, between $Al_xGa_{1-x}As$ and GaAs is generally accepted to be $\approx 60\%$ of the difference in the bulk material band gaps (Rogers & Nicholas 1985). The band gap of $Al_{0.3}Ga_{0.7}As$ is derived as a linear interpolation between the band gaps of AlAs and GaAs (Adachi, 1985).
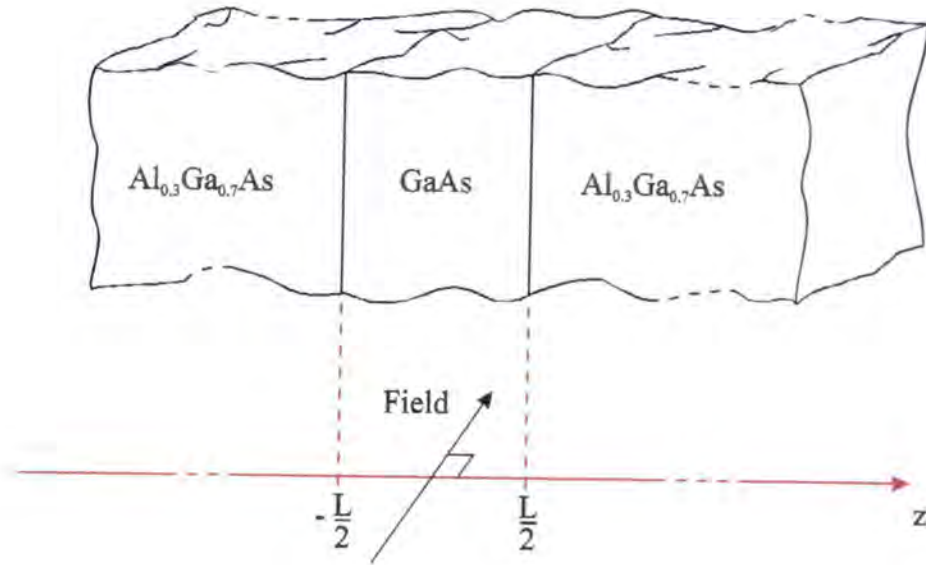
Figure 3.1

Schematic diagram of $Al_{0.3}Ga_{0.7}As/GaAs$ heterostructure studied

Well effective mass (m_w^*)	$0.063m_o$
Barrier effective mass (m_b^*)	$0.088m_o$
Well width (L)	70.0Å
Lattice temperature (T_L)	300K
Potential well depth (V_0)	0.19eV
Ground state energy (E_0)	0.047eV
First excited state energy (E_1)	0.17eV

Table 3.1

Parameters used in $Al_{0.3}Ga_{0.7}As/GaAs$ quantum well simulation

The doping density of the heterostructure is taken to be sufficiently small that there are no effects on the electron states due to band bending. The effective mass model, and standard theory (Bastard 1988) for the quantum well has been used to describe the electron states. The well is deep enough to bind two states at the band minima $(k_{\parallel} = 0)$, and produce two subbands for non-zero values of parallel electron wavevector $(k_{\parallel})$, as shown in figure 3.2. The effective potential well depth decreases with $k_{\parallel}$ because the effective mass of the alloy (barrier) is greater than that of GaAs (well). As a consequence the first excited state becomes unbound for values of $k_{\parallel} \geq 0.063\text{Å}^{-1}$, as apparent in figure 3.2.

We have simulated parallel electron transport at 300K for electric fields applied perpendicular to the growth direction. The electric field is restricted to values sufficiently low that electron scattering out of the well (real space transfer) or scattering to valleys other than the Γ valley are improbable. This simplifies our problem and localises the electrons to the region where the effect of the heterostructure on the phonon modes is dominant.
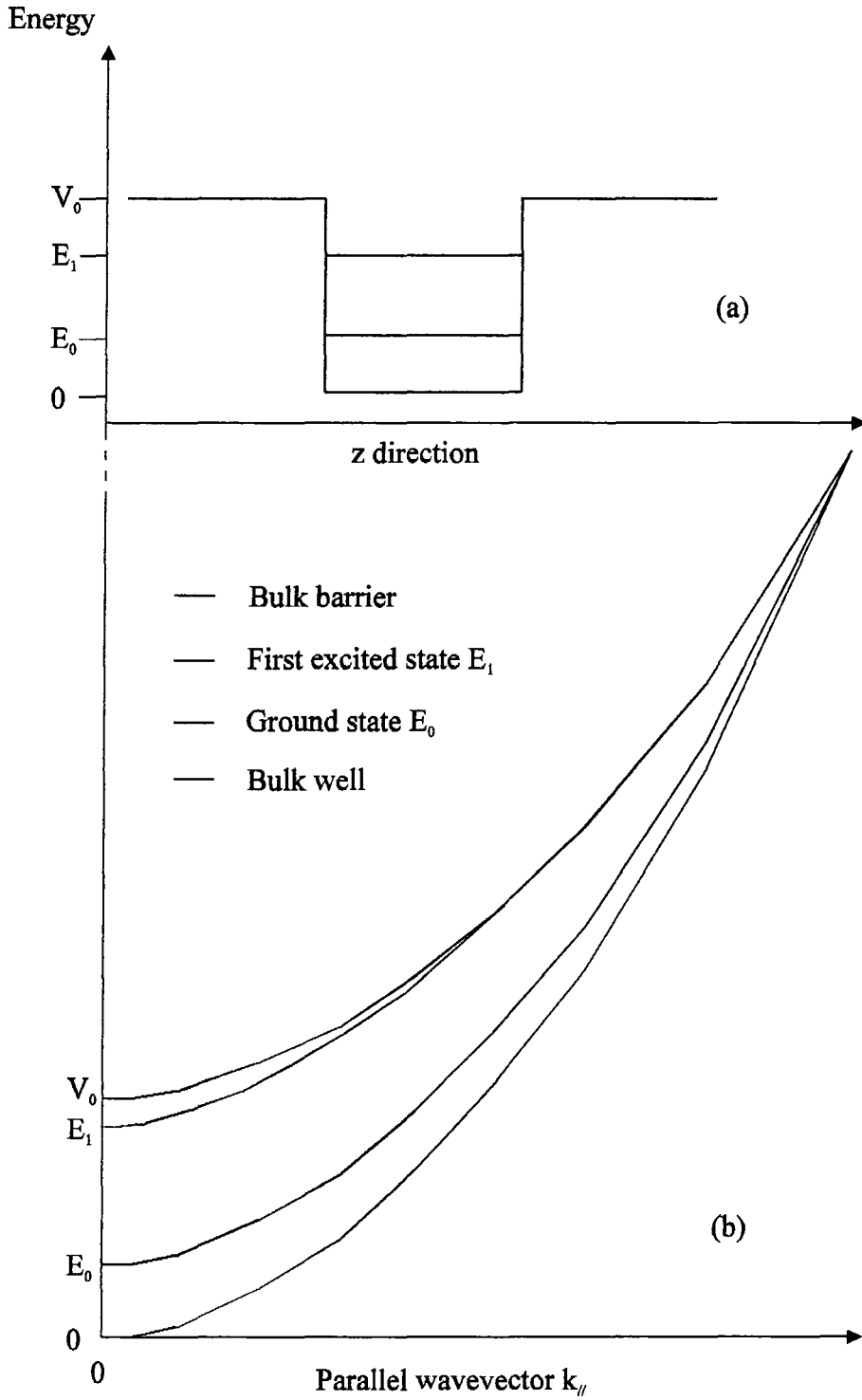
Figure 3.2

Electron energy states in the quantum well.

(a) at $k_{//} = 0$, (b) with increasing $k_{//}$.

3.3   Scattering events in quantum wells.

*L*ongitudinal polar optical (LPO) phonon scattering of electrons is well known to be the dominant process in limiting the room temperature low field mobility of carriers in III-V semiconductors and has been included in our simulation, along with elastic scattering via acoustic phonons. Piezoelectric scattering is not included as it is only significant at low temperatures. The two mode character of the lattice vibrations in AlGaAs has been approximated for simplicity by one effective mode, as in chapter two.

Doping the barrier material to supply carriers for the quantum well is a common way of reducing ionised impurity scattering of the bound states while maintaining the required density of charge in the well. Often there is a layer of undoped barrier, a spacer layer, to separate further the charge in the well from their donor atoms in the barrier. However, this spacer layer is usually thin enough that the potential of the donor atoms still has some interaction with the bound carriers; this causes *remote* ionised impurity scattering. However, as we are only considering low doped structures, remote ionised impurity scattering is small and has not been included in our simulations. Also, as the well material is undoped, there is no *local* ionised impurity scattering of the electrons.

In real devices the interfaces between the well layer and the barrier materials are not perfectly smooth. The fluctuations in layer width affect the energy levels in the potential well causing them to deviate from their

average positions. This can be modelled as fluctuations of the potential well depth away from a perfect well layer potential, and its effect on the electron transport is described as interface roughness scattering. Interface roughness scattering is dependent on the electron density; the higher the density the greater the effect. In low doped structures like ours, interface roughness scattering will be negligible and has not been included (Weisbuch & Vinter, 1991).

That portion of the electron probability density which penetrates the alloy barrier will interact with the randomly arranged scattering potentials of the $Al_{0.3}Ga_{0.7}As$ lattice. However, this interaction will be small due to the small penetration of the bound states into the barrier (Bastard 1983) and so alloy scattering has not been included in our simulations.

As can be seen the main scattering process in our quantum well under these conditions is LPO phonon scattering. Therefore, this model will provide a good comparison of the effects the scattering rates from the three phonon models have on the parallel transport properties of bound eletrons.

3.4 Polar optical phonon models.

*F*or LPO phonons the electron-phonon interaction energy is given by $e\Phi$, where e is the charge on the electron and Φ is the scalar potential of the electric field associated with the lattice vibration. For each of the phonon models introduced in section 3.1 the scalar potential will have, due to isotropy and translational symmetry perpendicular to the growth direction, a plane wave form for the parallel phonon wavevector ($q_{\parallel}$) (Huang & Zhu 1988, Chamberlain 1987),

$$\Phi(\mathbf{r}) = \phi_z(z)e^{i\mathbf{q}_{\parallel}\cdot\mathbf{x}_{\parallel}} \qquad 3.2$$

The variation of the potential in the growth direction, $\phi_z(z)$, for each model is derived from the boundary conditions of that model.

3.4.1 Bulk phonon approximation (BPA)

The Bulk Phonon Approximation neglects any effect due to the heterostructure. Before the introduction of macroscopic theories for phonons in double heterostructures the BPA was widely used in simulation of transport in quantum wells (Tanimoto *et al* 1988, Riddoch & Ridley 1983). We use it here as a method of measuring the effects of phonon confinement on the electron-phonon interaction and transport properties.

Since the electron probability is concentrated in the well region of the heterostructure it is appropriate to consider the phonon properties of the system as those of a bulk sample of the well material. The scalar potential

for a bulk phonon mode is (Kelsall 1989)

$$\Phi(\mathbf{r}) = \left[\frac{\hbar \omega_{LO} \left(\varepsilon_s - \varepsilon_\infty \right)}{2\Omega \varepsilon_0 \varepsilon_s \varepsilon_\infty q^2} \right]^{\frac{1}{2}} e^{i(\mathbf{q} \cdot \mathbf{r} - \omega t)} \qquad 3.3$$

where $\mathbf{q}$ is the phonon wavevector, ω_{LO} is the phonon frequency and ε_∞ and ε_s are the high and low frequency dielectric functions respectively.

3.4.2 Dielectric Continuum Model (DCM)

The DCM model is based on the Fuchs and Kliewer (1965) treatment of an ionic film. At the interface between two materials of different permitivities it is necessary, in electromagnetic theory, to have continuity of the parallel component of the electric field $\mathbf{E}_\parallel$ and, the perpendicular component of the displacement field $\mathbf{D}_\perp$. These requirements are used in conjunction with the equations of electrostatics;

$$\nabla \times \mathbf{E} = 0 \qquad 3.4$$

and,

$$\nabla \cdot \varepsilon(\omega) \mathbf{E} = \rho(x). \qquad 3.5$$

where $\rho(x)$ is the free charge density (for our low doped device approximated as $=0$) and $\varepsilon(\omega)$ is the frequency dependent form of the dielectric function given as (Born & Huang 1954, Huang & Zhu 1988),

$$\varepsilon(\omega) = \varepsilon_\infty \frac{\left(\omega^2 - \omega_{LO}^2 \right)}{\left(\omega^2 - \omega_{TO}^2 \right)}. \qquad 3.6$$

In equation 3.6, ω_{LO} and ω_{TO} are the longitudinal and transverse optical zone centre phonon frequencies of the bulk lattice vibration.

For longitudinal optical modes equation 3.4 is satisfied by $\mathbf{E} = -\nabla\Phi(\mathbf{r})$ which gives for equation 3.5

$$\varepsilon(\omega)\nabla^2\Phi(\mathbf{r}) = 0. \qquad 3.7$$

The solutions to equation 3.7, together with the boundary conditions and the dielectric functions of the well and barrier materials, $\varepsilon_W(\omega)$ and $\varepsilon_B(\omega)$, specify the scalar potentials for this model. These solutions are divided into confined and interface modes. The confined modes are strictly confined to the quantum well and vibrate with the well material phonon frequencies. The interface modes have a maximum in the scalar potential at the well edges which decays exponentially into both the well and barrier, and vibrate with phonon frequencies between the LO and TO mode values of the barrier and well materials.

The scalar potential for the confined LOP modes in the Dielectric Continuum Model is given by

$$\Phi = \left[\frac{\hbar\left(\varepsilon_s - \varepsilon_\infty\right)\omega_{LO}^2}{\Omega\varepsilon_0\varepsilon_\infty\varepsilon_s\left(q_\|^2 + q_z^2\right)}\right]^{\frac{1}{2}} \left\{\begin{array}{c}\cos\left(\frac{n\pi}{L}z\right) \\ \sin\left(\frac{n\pi}{L}z\right)\end{array}\right\} e^{i\mathbf{q}_\|\cdot\mathbf{x}_\|} \quad \begin{array}{l} n = 1, 3, 5, \ldots \\ \\ n = 2, 4, 6, \ldots \end{array} \qquad 3.8$$

where L is the thickness of the confining layer, z has its origin at the midpoint of the layer, $x_\|$ and $q_\|$ are the position and wavevector parallel to the barrier-well interface (the x-y plane), q_z is the wavevector in the growth direction $\left[= \frac{n\pi}{L}\right]$ and all other quantities are defined as in the BPA case above.

Substitution for the form of Φ (equation 3.2) into equation 3.7 and use of the boundary conditions, for solutions that do not vibrate with bulk
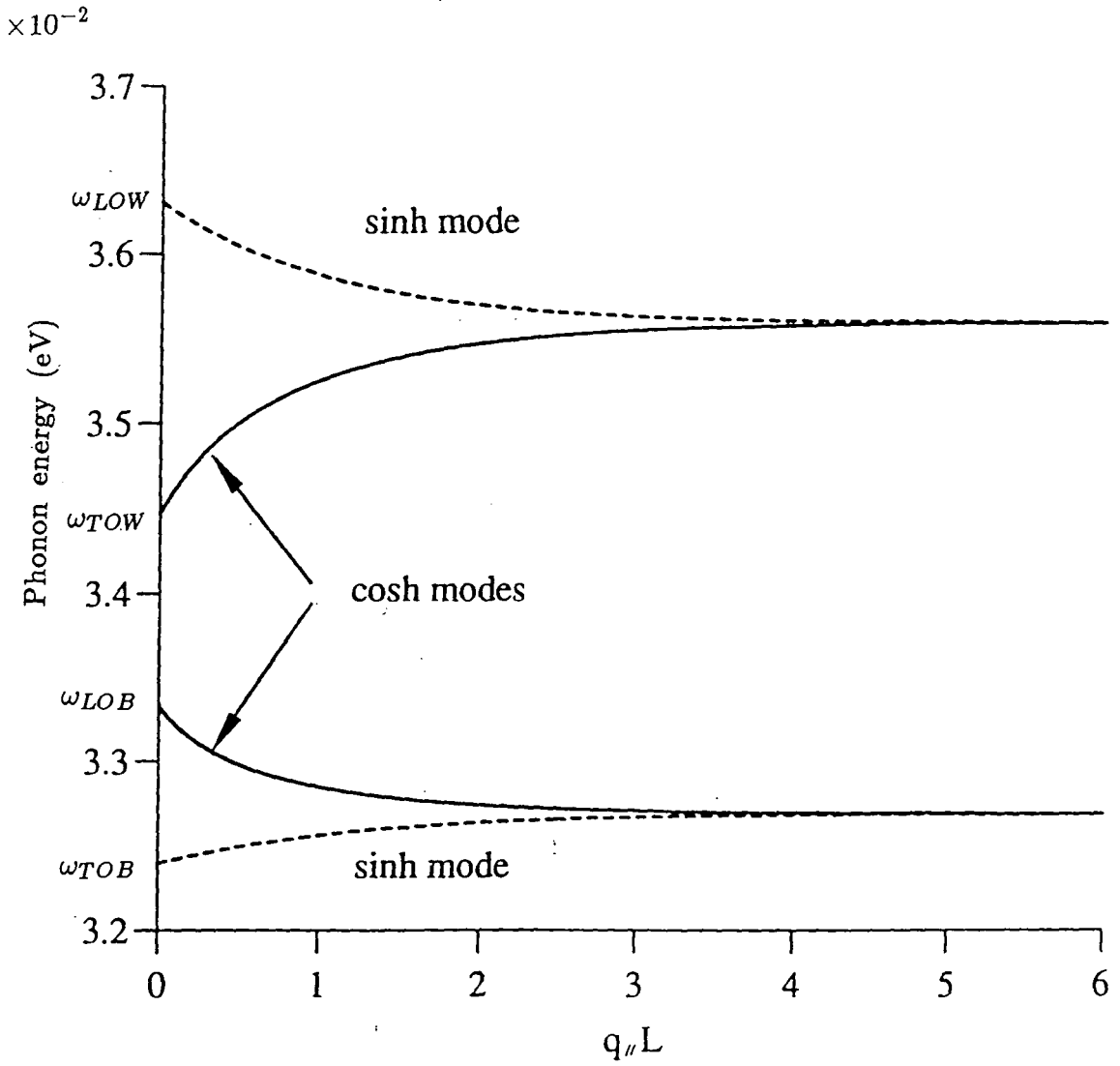
Figure 3.3

Dispersion relation for the DCM interface modes.

well material phonon frequencies, gives the general form for the interface

modes and sets $q_z = q_\parallel$. For the boundary condition equations to have a

non-trivial solution requires (Fuchs & Kliewer 1965)

$$e^{-q_\parallel L} = \pm \frac{(\varepsilon_W + \varepsilon_B)}{(\varepsilon_W - \varepsilon_B)},\qquad\qquad 3.9$$

which can be thought of as a dispersion relation defining the vibrational

frequencies of the interface modes, see figure 3.3. Here the energy of the

phonon $(= \hbar\omega)$ is plotted against the parallel phonon wavevector times the

well width, L. As can be seen, for small in-plane wavevectors there are four

distinct frequencies of vibration which have values very close to the bulk

LO and TO modes of the well and barrier materials(ω_{LOW}, ω_{TOW}, ω_{LOB},

ω_{TOB}). However, for large wavevectors these four frequencies converge to

give two values. The four modes of vibration are made up of two even

parity, cosh-like potentials and two odd parity, sinh-like potentials. The

form of the scalar potential for both even modes is the same

$$\Phi = A_2 \begin{Bmatrix} \left[1 + e^{q_z L}\right] e^{q_z z} \\ 2\cosh\left(q_z z\right) \\ \left[1 + e^{q_z L}\right] e^{-q_z z} \end{Bmatrix} e^{i q_\parallel \cdot x_\parallel} \quad \begin{matrix} z \le -\frac{L}{2} \\ -\frac{L}{2} \le z \le \frac{L}{2} \\ \frac{L}{2} \le z \end{matrix} \qquad 3.10$$

with only the phonon frequency branch defining which of the two even

potentials is being considered. Similarly with the odd potentials, which have

the form

$$\Phi = A_2 \begin{Bmatrix} \left[1 - e^{q_z L}\right] e^{q_z z} \\ 2\sinh\left(q_z z\right) \\ -\left[1 - e^{q_z L}\right] e^{-q_z z} \end{Bmatrix} e^{i q_\parallel \cdot x_\parallel} \quad \begin{matrix} z \le -\frac{L}{2} \\ -\frac{L}{2} \le z \le \frac{L}{2} \\ \frac{L}{2} \le z \end{matrix}. \qquad 3.11$$

where, in equations 3.10 and 3.11

$$|A_2|^2 = \frac{\hbar\omega}{4Aq_\parallel}\left[2\left(\frac{\varepsilon_0}{\alpha_B}\right)^2\left(\omega^2+\omega_{LO_B}^2\right)\left\{\begin{array}{c}\cosh^2\left(\frac{q_zL}{2}\right)\\\sinh^2\left(\frac{q_zL}{2}\right)\end{array}\right\}\right.$$
$$\left.+\left(\frac{\varepsilon_0}{\alpha_W}\right)^2\left(\omega^2+\omega_{LO_W}^2\right)\sinh\left(q_zL\right)\right]^{-1} \qquad 3.12$$

with the upper case for cosh modes and the lower case for sinh modes. α_i is defined as

$$\alpha_i^2 = \left[\frac{\varepsilon_0\left(\varepsilon_{si}-\varepsilon_{\infty i}\right)}{\varepsilon_{si}\varepsilon_{\infty i}}\right]\omega_{LO_i}^2 \quad i=W \text{ or } B. \qquad 3.13$$

3.4.3 The Hydrodynamic Model (HDM)

Babiker and co-workers (Babiker 1986, Ridley 1989, Chamberlain 1987 & 1990) have made use of the lattice dynamical treatment of Born and Huang (1965) with hydrodynamic boundary conditions at the well edges to describe the phonon states of the heterostructure quantum well. The heterointerface conditions are that the pressure and the velocity perpendicular to the well-barrier interface are continuous across the boundary. The hydrodynamic model also includes the effects of optical phonon mode dispersion on the heterostructure phonon.

Both guided and interface modes are predicted by the model and the derivation of the scalar potential and dispersion relations for both are the same but for the definition of the growth direction (z) component of the wavevector in the well region, q_W. There are four guided modes in our 70Å well (Chamberlain 1987) and they have ionic displacements that decay exponentially away from the interface in the barriers and have cos-like or

sin-like displacements in the well. There are two interface modes in the HDM, one cosh-like the other sinh-like, which have ionic displacements that are at a maximum at the well edges and decay exponentially into both the well and barriers. Both guided and interface modes for the HDM give a scalar potential of the form (Chamberlain 1990)

$$\Phi = 2A_1 \left\{ \begin{array}{ll} \sin\left(\frac{q_W L}{2}\right) \left[\frac{q_W \rho_B^{\frac{1}{2}}}{q_B \rho_W^{\frac{1}{2}}}\right] e^{-\frac{q_B L}{2}} e^{q_B z} & z \leq -\frac{L}{2} \\ \cos\left(q_W z\right) & -\frac{L}{2} \leq z \leq \frac{L}{2} \\ \sin\left(\frac{q_W L}{2}\right) \left[\frac{q_W \rho_B^{\frac{1}{2}}}{q_B \rho_W^{\frac{1}{2}}}\right] e^{-\frac{q_B L}{2}} e^{-q_B z} & \frac{L}{2} \leq z \end{array} \right\} e^{i q_{\parallel} \cdot x_{\parallel}} \qquad 3.14$$

for the even modes and

$$\Phi = 2iA_1 \left\{ \begin{array}{ll} \cos\left(\frac{q_W L}{2}\right) \left[\frac{q_W \rho_B^{\frac{1}{2}}}{q_B \rho_W^{\frac{1}{2}}}\right] e^{-\frac{q_B L}{2}} e^{q_B z} & z \leq -\frac{L}{2} \\ \sin\left(q_W z\right) & -\frac{L}{2} \leq z \leq \frac{L}{2} \\ \cos\left(\frac{q_W L}{2}\right) \left[\frac{q_W \rho_B^{\frac{1}{2}}}{q_B \rho_W^{\frac{1}{2}}}\right] e^{-\frac{q_B L}{2}} e^{-q_B z} & \frac{L}{2} \leq z \end{array} \right\} e^{i q_{\parallel} \cdot x_{\parallel}} \qquad 3.15$$

for the odd modes. Here A_1 is defined by,

$$|A_1|^2 = \frac{\hbar}{A \varepsilon_0^2 \omega} \left[\mp 2 \frac{\rho_B q_W^2 \left(q_B^2 + q_{\parallel}^2\right)}{\rho_W q_B^3 \alpha_B^2} e^{-2 q_B L} \left\{ \begin{array}{c} \sin^2\left(\frac{q_W L}{2}\right) \\ \cos^2\left(\frac{q_W L}{2}\right) \end{array} \right\} \right. $$
$$\left. + \frac{\left(q_W^2 + q_{\parallel}^2\right) L}{\alpha_W^2} \left[1 \pm \frac{\sin\left(q_W L\right)}{q_W L} \right] \right]^{-1} \qquad 3.16$$
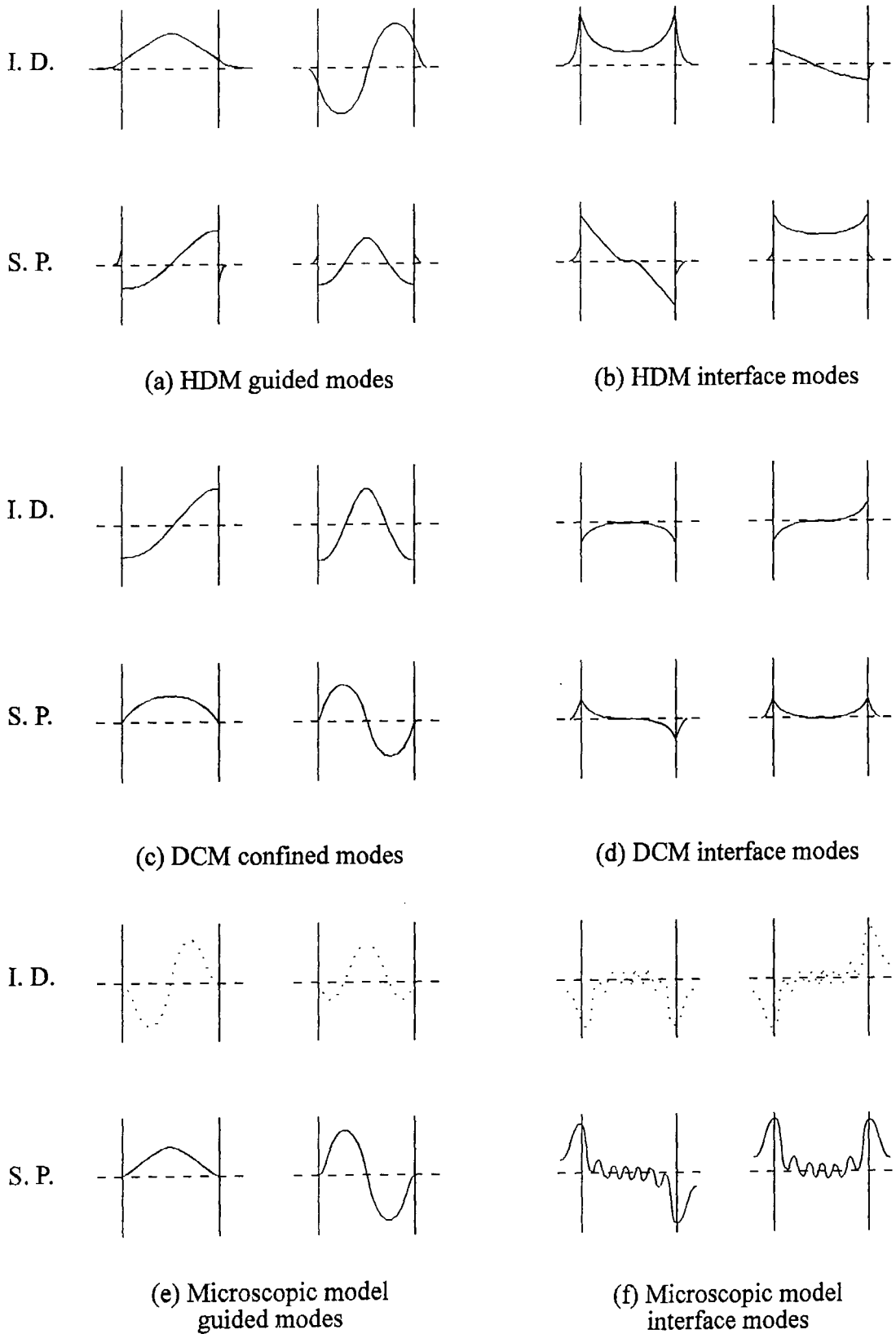
with the upper/lower choice of sign and function for the even/odd modes respectively. ρ_i is the material density, α_i is defined in section 3.4.2, and q_i is the q_z component of the wavevector in the the well or barrier material, defined as,

$$q_i^2 = \frac{\omega_{LOi}^2 - \omega^2}{\beta_i^2} - q_{\parallel}^2 \quad i = W \text{ or } B \qquad 3.17$$

with β_i the velocity parameter in the bulk dispersion relation of the well or barrier material. The z component of the wavevector in the well region, q_W, is real for the guided modes and imaginary for the interface modes.

3.4.4 Comparison & criticism of the phonon models.

The main differences in the three phonon models can be seen with reference to figure 3.4, which is a schematic pictorial representation of the scalar potentials and ionic displacements for the interface modes of both the HDM and the DCM, the two lowest guided and confined modes of the HDM and DCM models respectively and a microscopic model (Rücker *et al* 1992). The microscopic model has been included for comparison as it provides an accurate description of the actual lattice vibrations of a quantum well heterostructure. The DCM confined modes are strictly confined to the well region and at the heterointerface there are nodes in the scalar potentials with anti-nodes and discontinuities in the ionic displacements. Conversely the HDM guided modes penetrate into the barrier region and have ionic displacements that approach zero with anti-nodes and discontinuities in the scalar potentials at the well edges. The microscopic model is continuous across the boundaries in both scalar potential and ionic displacement. Also note that the lowest mode scalar potential of the DCM confined state is cos-like while that of the HDM guided mode is sin-like, this is important when calculating scattering rates as will be discussed later. The DCM and HDM are alike in that they both predict interface modes of a similar form, although they have different dispersion relations. The BPA, as it neglects

(a) HDM guided modes

(b) HDM interface modes

(c) DCM confined modes

(d) DCM interface modes

(e) Microscopic model
guided modes

(f) Microscopic model
interface modes

Figure 3.4

Comparison of ionic displacement (I. D.) and scalar potential (S. P.)
for the HDM and DCM phonon models and, for comparison,
a microscopic model (Rücker et al 1992).

the heterostructure entirely, is continuous in both scalar potential and ionic displacement but is not necessarily nodal at the interfaces.

There are two main criticisms of the DCM theory. First, the discontinuities in the ionic displacement at the well edges is un-physical and does not agree with microscopic models, and secondly, it neglects the effects of phonon dispersion in the bulk materials. Modified models which set the ionic displacement to zero at the interfaces have recently been developed (Huang & Zhu 1988). Haupt & Wendler (1991) have shown that the modified DCM theory predicts similar though slightly smaller scattering rates to the original. In the transport calculations we have used the original formulation for simplicity.

The HDM is also defective in that it predicts anti-nodes and discontinuities in the scalar potential at the well edges and the lowest order guided mode scalar potential is sin-like. All of these points are in contradiction with the results of the microscopic model.

A problem which the DCM and HDM models have in common is that they do not allow the confined and interface modes to couple, which is again predicted by the microscopic models, although hybrid continuum models which account for these main discrepencies between continuum and microscopic models have recently been developed (Ridley 1992, Zianni *et al* 1992).

3.5 The scattering rates.

$\mathcal{F}rom$ Fermi's Golden rule, we can obtain the formula for scattering a bound electron from a state **k** to a state **k**$'$ by optical phonons as (Kelsall 1989, Chamberlain 1987);

$$P\left(\mathbf{k}, \mathbf{k}'\right) = \frac{2\pi}{\hbar} R \int \left\{ \begin{matrix} N_q \\ N_q + 1 \end{matrix} \right\} \left| I(\mathbf{k}', \mathbf{k}) \right|^2 \delta\left(E_{k'} - E_k \mp \epsilon_{ph}\right) d\mathbf{Q}, \qquad 3.18$$

where

$$R = \frac{A}{(2\pi)^2} \text{ and } d\mathbf{Q} = d\mathbf{q}_{\parallel} \qquad\qquad 3.19$$

for the HDM and DCM, as the z component of the phonon wavevector, q_z, is already defined by the phonon mode under consideration, and,

$$R = \frac{\Omega}{(2\pi)^3} \text{ and } d\mathbf{Q} = d\mathbf{q} \qquad\qquad 3.20$$

for the BPA. In equations 3.18 to 3.20, A is the area of the well plane, N_q is the phonon mode occupation number, E_k, $E_{k'}$ and ϵ_{ph} are the initial and final electron state energies and, the phonon energy respectively. The upper options are for absorption of a phonon and the lower options are for the emission of a phonon. $I(\mathbf{k}', \mathbf{k})$ is the matrix element;

$$I(\mathbf{k}', \mathbf{k}) = \int \psi_{k'}^* e\Phi\psi_k \, d\mathbf{r} \qquad\qquad 3.21$$

where e is the charge on an electron and Φ is the phonon scalar potential defined (in equation 3.2) as

$$\Phi = \phi_z e^{i\mathbf{q}_{\parallel} \cdot \mathbf{x}_{\parallel}}. \qquad\qquad 3.22$$

(The form of ϕ_z can be seen with reference to section 3.4).

The initial and final electron state wavefunctions are designated by ψ_k and $\psi_{k'}$ respectively, and are functions of the form:-

$$\psi_k = \frac{1}{\sqrt{A}} u_k(r) f(z) e^{i k_\parallel \cdot x_\parallel}, \qquad 3.23$$

where $u_k(r)$ is the periodic part of the bulk Bloch function, and $f(z)$ describes the z dependence of the wavefunction.

After substituting for the electron and phonon states into the matrix element (equation 3.21) and expanding the periodic function $u_{k'}^*(r) u_k(r)$, as a Fourier series over reciprocal lattice vectors, g, we get

$$I(k',k) = e \sum_{g} c_g \frac{(2\pi)}{A} \delta(k_\parallel - k'_\parallel \pm q_\parallel + g_\parallel) \int f'^*(z) \phi_z e^{i g_z \cdot z} f(z) dz', \qquad 3.24$$

where the c_g are the coefficients of the Fourier series and are defined by:-

$$c_g = \frac{1}{V_{\text{cell}}} \int_{\text{cell}} u_{k'}^*(r') u_k(r') e^{-i g \cdot r'} dr'. \qquad 3.25$$

As the smallest non-zero value of $g_\parallel$ is much larger than $k_\parallel$ and $q_\parallel$, the argument of the delta function can vanish only if $g_\parallel = 0$. On this basis, we assume only terms with g = 0 contribute to the scattering rate (Kelsall 1989). The total probability of scattering from a bound state k for polar optical scattering is then

$$P\left(k, k'\right) = \frac{2\pi}{\hbar} Re \int \left\{ \begin{matrix} N_q \\ N_q + 1 \end{matrix} \right\} \left| J(q_\parallel, q_z) \right|^2 \left| G(k', k) \right|^2$$

$$\times \frac{(2\pi)^2}{A} \delta(k_\parallel - k'_\parallel \pm q_\parallel) \delta\left(E_{k'} - E_k \mp \epsilon_q\right) dQ, \qquad 3.26$$

where $G(\mathbf{k}', \mathbf{k})$ is the overlap integral;

$$G(\mathbf{k}', \mathbf{k}) = \frac{1}{V_{\text{cell}}} \int_{\text{cell}} u^*_{k'}(r') u_k(r') dr', \qquad 3.27$$

and,

$$J(q_{\parallel}, q_z) = \int f'^*(z) \phi_z f(z) dz. \qquad 3.28$$

Making the standard assumption that the functions $u_k(r)$ can be approximated by the zone centre Bloch functions $|G(k'_z, k_z)|^2$ is unity for all transitions. Integrating over $\mathbf{q}_{\parallel}$ in equation 3.26 then gives

$$P(k, k') = \frac{L_z}{\hbar} \int_{-\infty}^{+\infty} \left\{ \begin{matrix} N_q \\ N_q + 1 \end{matrix} \right\} \left| J(q_{\parallel}, q_z) \right|^2 \Big|_{q_{\parallel} = k_{\parallel} - k'_{\parallel}} \delta\left(E_{k'} - E_k \mp \epsilon_{ph}\right) dq_z,$$

$$3.29$$

for the BPA where L_z is the total device length, and

$$P(\mathbf{k}, \mathbf{k}') = \frac{2\pi}{\hbar} \left\{ \begin{matrix} N_q \\ N_q + 1 \end{matrix} \right\} \left| J(q_{\parallel}, q_z) \right|^2 \Big|_{q_{\parallel} = k_{\parallel} - k'_{\parallel}} \delta\left(E_{k'} - E_k \mp \epsilon_{ph}\right) \qquad 3.30$$

for the DCM and HDM.

To get the total scattering rate, $P(\mathbf{k})$, we must integrate over all final electron states

$$P(\mathbf{k}) = \frac{A}{(2\pi)^2} \int P(\mathbf{k}, \mathbf{k}') d\mathbf{k}'_{\parallel}. \qquad 3.31$$

The integral over all final electron states is only over the parallel wavevector component of the state $(\mathbf{k}'_{\parallel})$ as the final k_z component is already defined for the process we are considering. It is convenient in equations 3.31 to

convert the delta function argument to wavevectors using

$$\delta(E' - E_f) = \frac{\delta(k' - k_f)}{\left|\frac{\partial E'}{\partial k'}\right|}, \qquad 3.32$$

and change the vector integral to

$$d\mathbf{k}'_\parallel = k'_\parallel dk'_\parallel d\theta \qquad 3.33$$

where θ is taken as the angle between $k'_\parallel$ and $k_\parallel$. Integrating over $k_\parallel$ now gives

$$P(\mathbf{k}) = \frac{\Omega}{\hbar(2\pi)^2} \left\{ \begin{matrix} N_q \\ N_q + 1 \end{matrix} \right\} \int_0^{2\pi} \int_{-\infty}^{\infty} \left| J(q_\parallel, q_z) \right|^2_{\Big|q_\parallel = k_\parallel - k'_\parallel} \frac{k_{\parallel_f}}{\left|\frac{\partial E'}{\partial k'}\right|} dq_z d\theta, \qquad 3.34$$

for the BPA, and

$$P(\mathbf{k}) = \frac{A}{2\hbar\pi} \left\{ \begin{matrix} N_q \\ N_q + 1 \end{matrix} \right\} \int_0^{2\pi} \left| J(q_\parallel, q_z) \right|^2_{\Big|q_\parallel = k_\parallel - k'_\parallel} \frac{k_{\parallel_f}}{\left|\frac{\partial E'}{\partial k'}\right|} d\theta, \qquad 3.35$$

for the DCM and HDM.

The integral over θ is straightforward for the BPA and DCM confined modes but, due to the complex nature of ϕ and the dependence of q_z on $q_\parallel$ in the DCM interface and HDM modes, we have to evaluate the integral in θ numerically for these cases. The integral over q_z in the BPA has to be evaluated numerically.

3.5.1 Acoustic scattering

When this work was carried out there were, to our knowledge, no continuum models which describe quantum well acoustic phonon modes

that took into account the heterostructure. In bulk semiconductors, rates for acoustic phonon scattering of electrons are well known to be small in comparison with polar optical phonon scattering, and it is expected that the same will be true when considering scattering by phonons in heterostructure quantum wells.

Scattering by acoustic phonons was described in all cases by the standard deformation potential theory in the bulk phonon approximation. The calculation is similar for the BPA optical phonon scattering described above except for the matrix element definition which in the acoustic phonon case is (Kelsall 1989)

$$I(\mathbf{k'}, \mathbf{k}) = \left(\frac{\hbar}{2\Omega\rho v_s q}\right)^{\frac{1}{2}} \int \psi_{k'}^* \Xi q \psi_k \, d\mathbf{r} \qquad 3.36$$

where Ξ is the deformation potential, v_s is the sound velocity, and ρ is the material density.

Figure 3.5 shows the rate for total scattering of electrons in the ground state by acoustic phonons including intra- and inter-subband elastic scattering, and a comparison with the infinite well approximation of Price (1981), and with the rate for the bulk material. The total rate is plotted against initial electron energy measured from the subband minimum. It can be seen that the quantum well rates are of a similar magnitude to the bulk. The bulk rate gradually increases from zero with a square root dependence on energy, which can be directly attributed to the bulk density of states. However, rates for our finite well model and the infinite well
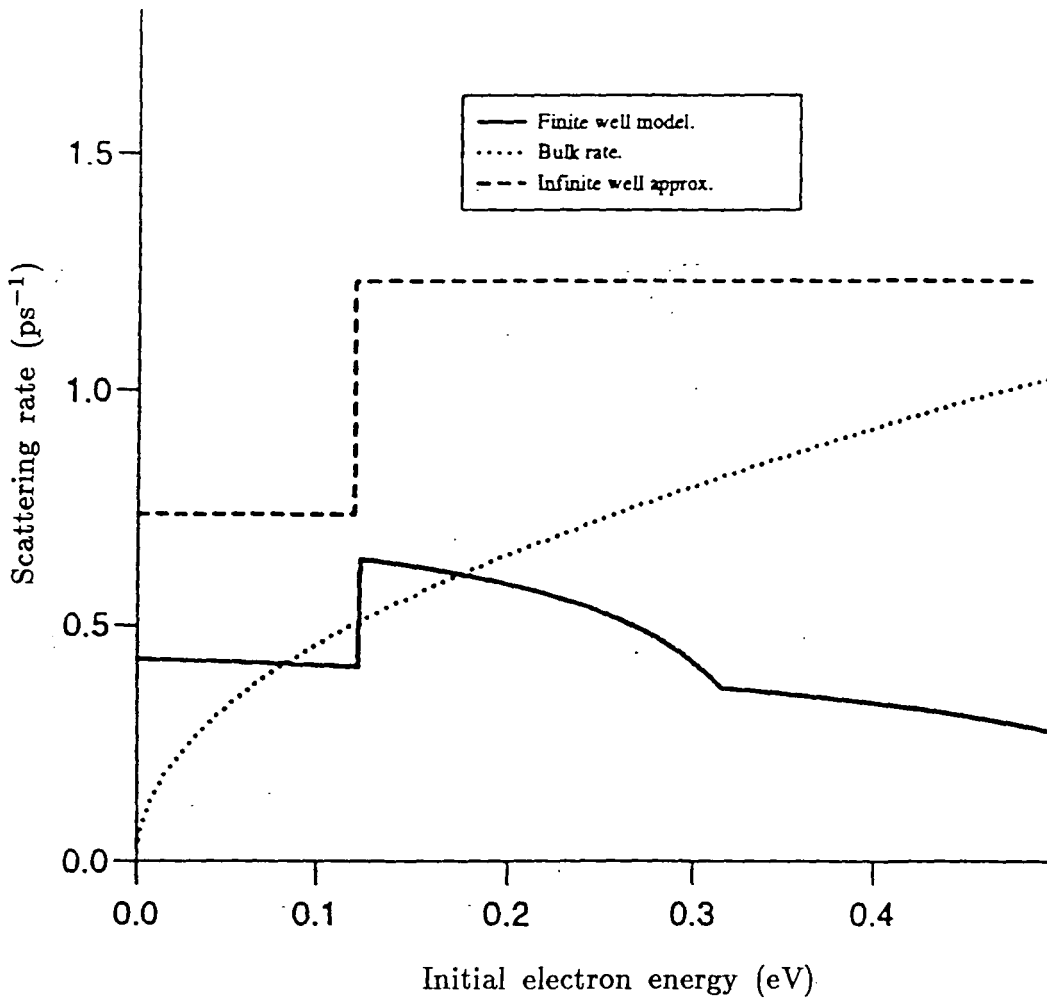
Figure 3.5

Acoustic phonon scattering rates for our finite well model,

the infinite well approximation (Price 1981) and bulk GaAs.

approximation have non-zero rates at zero initial energy and sharp step-like changes in probability. These features are due to the step-like form of the electronic density of states in a quantum well, and the sharp increase in scattering occurs at an initial energy of $\approx 0.13\text{eV}$ where transitions to the first excited state become probable. Transitions to the first excited state stop in the finite well model at about 0.33eV, which is where this state becomes unbound.

3.5.2 Optical phonon scattering rates

In order to conserve parity the scalar potentials have to be symmetric with respect to the centre of the well for intra-subband scattering and anti-symmetric for inter-subband transitions. For the DCM confined modes it is the potential of the first even/odd mode which has the greatest interaction with the electrons for intra-/inter-subband scattering. The potentials of higher order modes give rates at least an order of magnitude lower, and so only the potential of the first mode of each parity has been used in our calculations. A similar trend is seen for the guided modes of the HDM, but it should be noted that the scalar potential of the first even mode comes not from the lowest order phonon mode, and Chamberlain (1987) has shown that this and subsequent even modes interact weakly with the electrons, and so have not been included in our simulations. Scattering by all interface modes' potentials of the DCM have been included but only the even parity interface mode's potential of the HDM is used to calculate scattering rates as the odd one has a weak interaction with the electrons.

The two main scattering rates which have been compared for the three phonon models are the phonon emission rates for scatterings in the ground state and from the first excited state to the ground state. The results can be seen in figures 3.6 and 3.7, where the scattering rate is plotted against the initial electron energy measured from the subband minimum. In figure 3.6 intra-subband polar optical phonon emission is plotted for the three phonon models, and as can be seen each model rate has a sharp increase at the point where the initial electron energy equals the phonon energy. This non-zero rate at threshold is due to the non-zero density of states at the subband minimum. The BPA and HDM models agree at the threshold but the BPA rate reduces while the HDM rate maintains a high value for a large range of energy. The total DCM rate (interface and confined modes) is much higher and reduces with increasing energy in a manner similar to the BPA.

Figure 3.7 shows the transition rates for an electron in the first excited state scattering to the ground state subband. Each model has the same general trend, with a maximum rate at the subband minimum gradually reducing with increasing energy. There is a non-zero rate at zero initial energy because the electron is emitting a phonon and falling into the lower energy ground state subband. The BPA and HDM predict rates of a similar magnitude, and again the total DCM gives a rate larger than the other two models. Note, that the inter-subband rate is nearly an order of magnitude lower than the intra-subband rates.
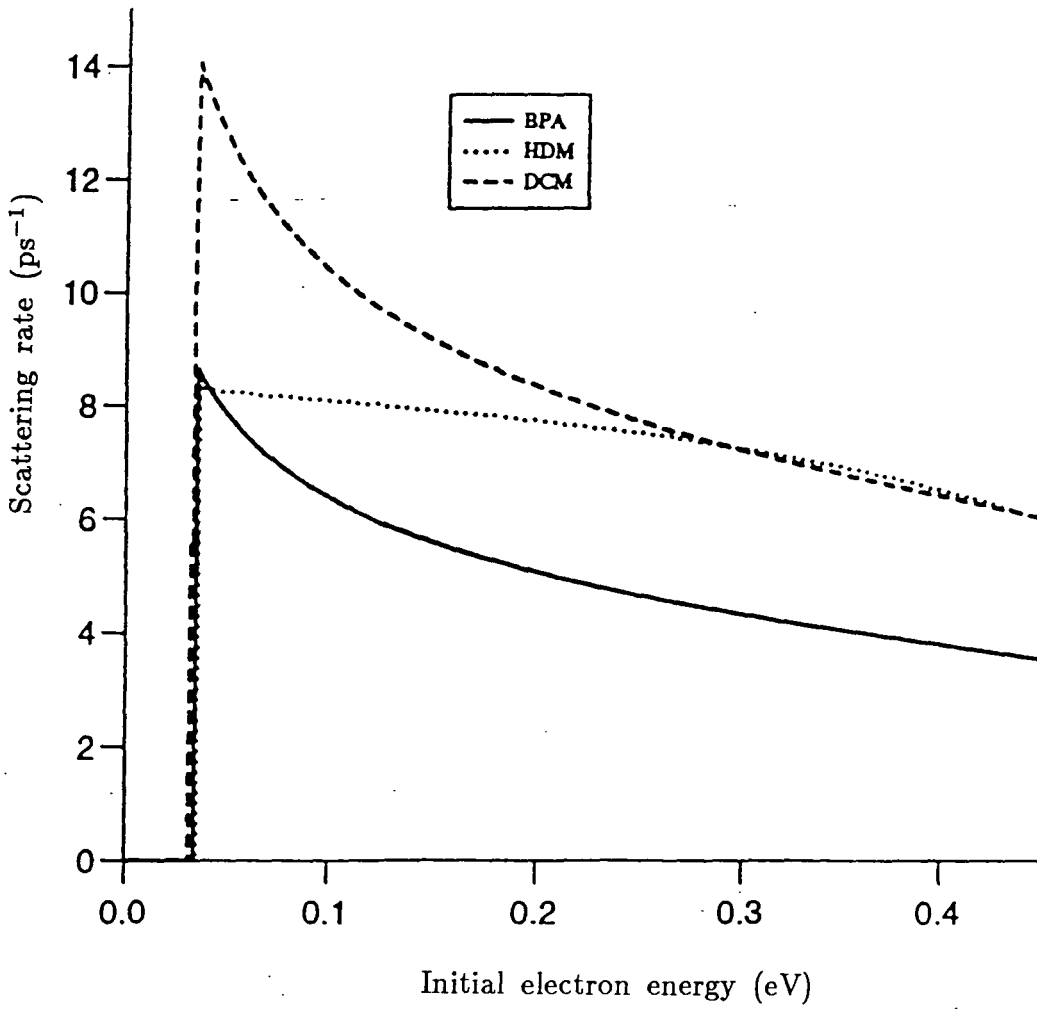
Figure 3.6

Comparison ground state intra-subband polar optical phonon
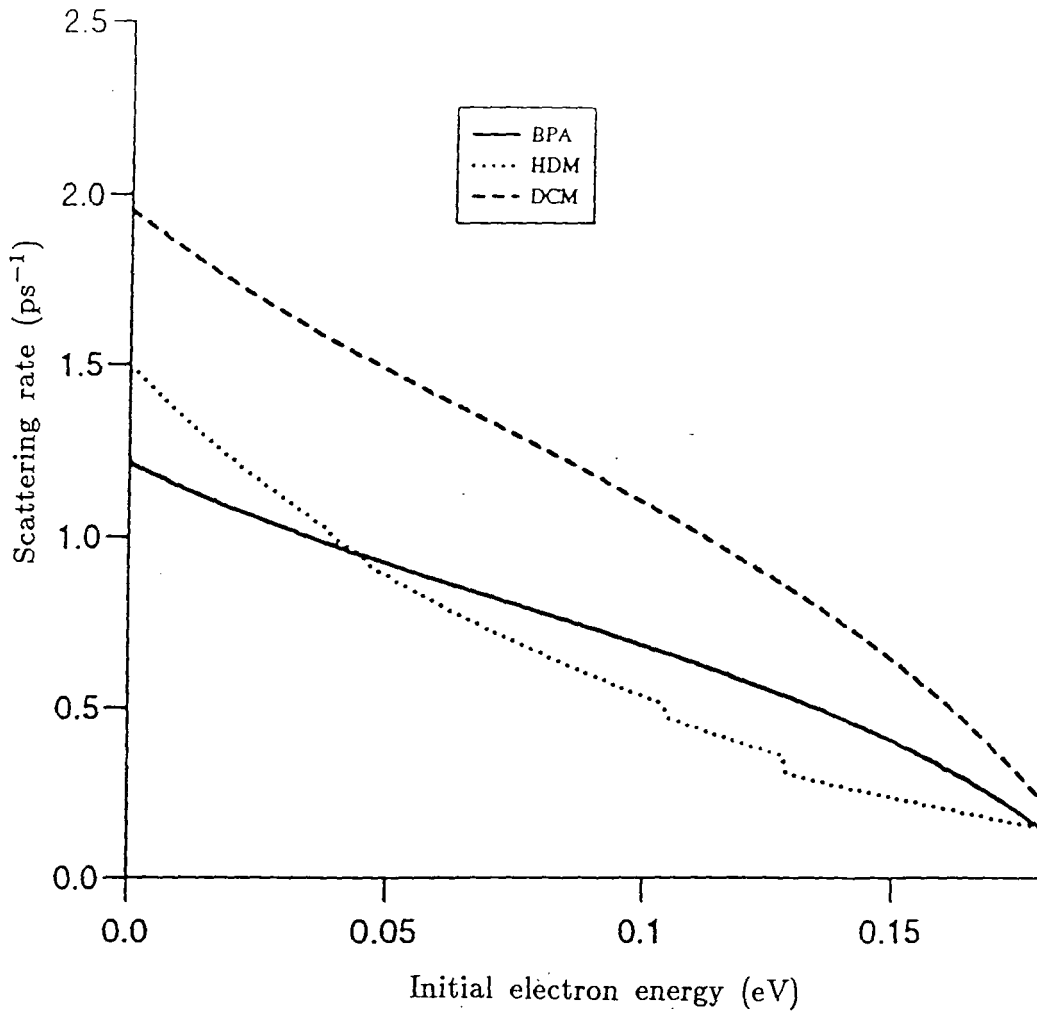
emission rates for the phonon models.

Figure 3.7

Transition from the first excited to ground state via polar

optical phonon emission for the phonon models.

(The step-like changes in the HDM rate are artifacts due

to the numerical method used to calculate these rates.)

The close agreement between the intrasubband rates for the HDM and the BPA is in contrast to previous work (Rudin & Reinecke 1990, Weber *et al* 1991), which compared the magnitude of the scattering rates predicted by these models, and is entirely due to the HDM interface modes which were not considered in these previous comparisons.

3.6   Results of Monte-Carlo simulations.

*S*ingle particle Monte-Carlo simulations of parallel transport in the quantum well with an applied parallel electric field have been carried out for all three phonon models. The purpose was to consider how macroscopic and microscopic transport properties are influenced by the different phonon models. The simulation scheme is based on a well established Monte-Carlo model of transport in quantum wells (Kelsall 1989, 1991 & 1992) which has been adapted to the particular physical system under consideration (Chamberlain *et al* 1992). The simulation has been used to examine the electron drift velocity, average energy and the frequency of ground state intra-subband absorption and emission events with steady state electric fields which are sufficiently low to avoid significant excitation of electrons out of the Γ valley well.

3.6.1 Drift velocities and mobilities

A comparison of the drift velocity against electric field for the three phonon models is shown in figure 3.8. The maximum electric field considered for each case is different because the different scattering rates affect the level of electric field which will cause significant emission from the well. The BPA and HDM models predict similar drift velocities and maximum field although it should be noted that the HDM velocities are slightly smaller than those predicted by the BPA. The DCM however, predicts velocities much lower than, and a maximum electric field seventy percent larger than, those for the BPA and HDM. The low field mobilities (at 300K) are, 1.16 $m^2V^{-1}s^{-1}$ for the BPA, 0.99 $m^2V^{-1}s^{-1}$ for the HDM and 0.462 $m^2V^{-1}s^{-1}$ for the DCM.

We can explain the differences in the three models with reference to the scattering rates in figure 3.6 and the average energy plot in figure 3.9. Figure 3.9 shows the average energy measured from the subband minimum plotted against electric field for the three models. It shows that the BPA and HDM have similar values for all fields (although the values in the HDM are smaller than in the BPA at higher fields), and the DCM predicts energies that are always much less than those in the other two models. For low electron energies ($\leq$ 0.035eV at fields less than $\approx$ 2.0kVcm^{-1}) the scattering rates for the BPA and HDM are very similar and the velocities and energies are roughly equal but as the field increases, and the average electron energy rises, the scattering rate in the BPA becomes less than in
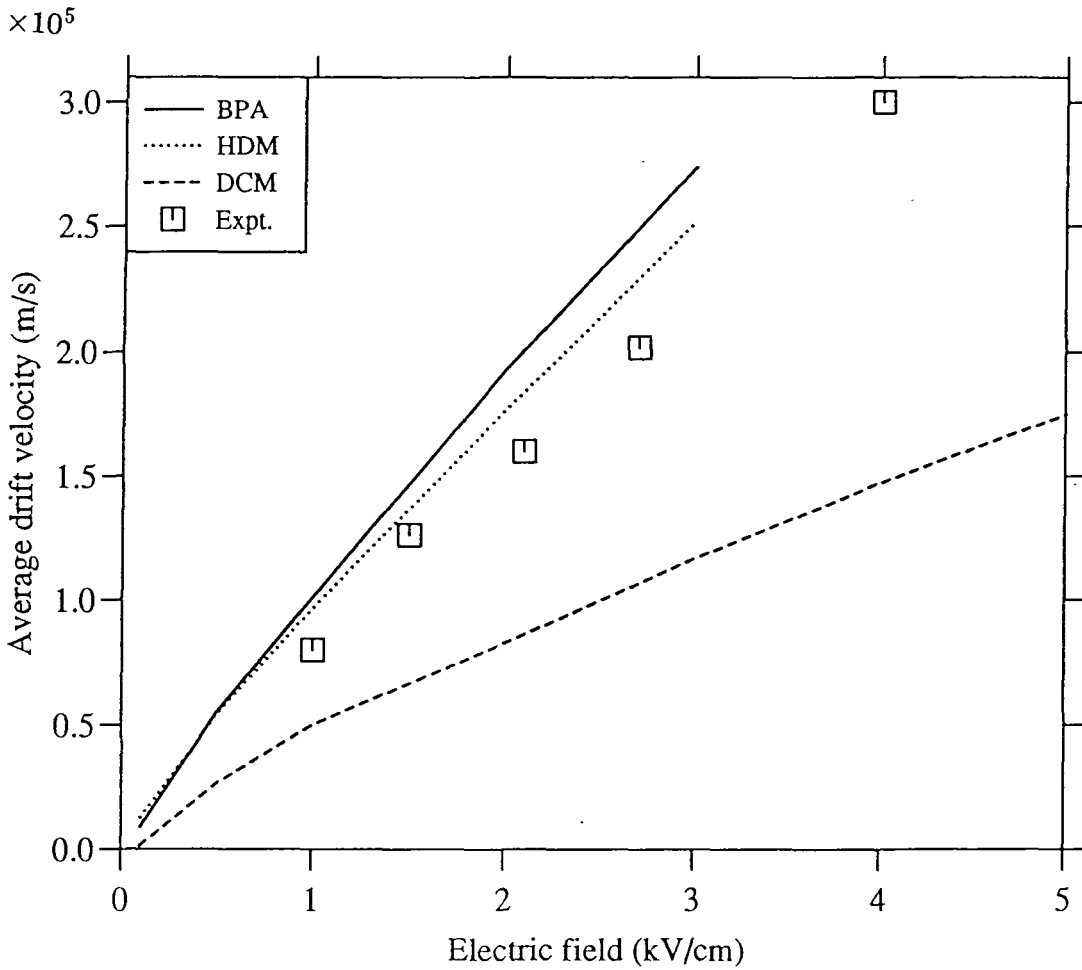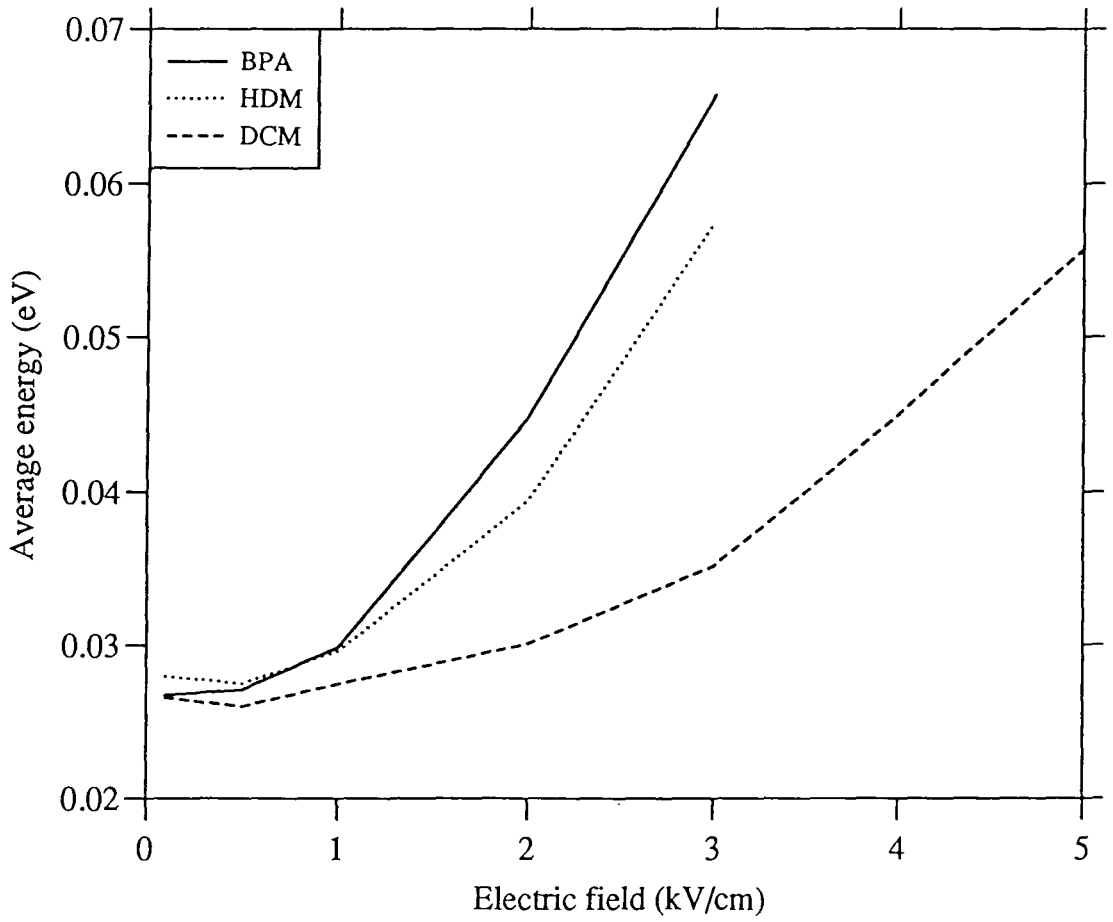
$\times 10^5$

Figure 3.8

The average drift velocity against electric field predicted

by the three phonon models and, for comparison, some

experimental results (Balkan *et al* 1989).

Figure 3.9

Average electron energy against electric field from the BPA,

HDM, and DCM simulations.

the HDM, and so electrons can achieve higher energies and velocities. The DCM has higher scattering rates and the velocity is correspondingly lower.

A contributory factor to the lower DCM drift velocity, which is not immediately apparent, is the dependence on θ, the angle between $\mathbf{k}'_\parallel$ and $\mathbf{k}_\parallel$, in the scattering rate. If we return to equation 3.29 and 3.30, which give the probability of scattering from a state $\mathbf{k}$ to another state $\mathbf{k}'$, we find a dependence on $q_\parallel$ of the form

$$P\left(q_\parallel\right) = \frac{f\left(q_z, q_\parallel\right)}{q_\parallel^2 + q_z^2} \qquad 3.37$$

for the DCM and HDM models, and

$$P\left(q_\parallel\right) = \int_{-\infty}^{\infty} \frac{f\left(q_z, q_\parallel\right)}{q_\parallel^2 + q_z^2} dq_z \qquad 3.38$$

for the BPA, where

$$q_\parallel^2 = {k_\parallel}^2 + {k'_\parallel}^2 - 2k_\parallel k'_\parallel \cos\theta \qquad 3.39$$

Generally, for the HDM and DCM, the functional form of $f\left(q_z, q_\parallel\right)$ is complicated but equation 3.37 can be taken[†] to a good approximation as

$$P\left(q_\parallel\right) = \frac{1}{q_\parallel^2 + q_z^2}. \qquad 3.40$$

This can be further simplified for the DCM interface modes, and in the HDM, by realising that $q_z = q_\parallel$ for DCM interface modes and $q_z = Fq_\parallel$ for the HDM (where F is a number less than unity). Equation 3.40 is now

$$P\left(q_\parallel\right) = \frac{1}{q_\parallel^2} \qquad 3.41$$

[†] Only for calculation of the angle $\mathbf{k}'_\parallel$ makes to $\mathbf{k}_\parallel$ after scattering.

for the DCM interface and HDM modes. For the DCM confined modes equation 3.40 becomes

$$P\left(q_{\parallel}\right) = \frac{1}{q_{\parallel}^2 + \left[\frac{n\pi}{L}\right]^2}. \qquad\qquad 3.42$$

In the BPA the function $f\left(q_z, q_{\parallel}\right)$ is sharply peaked at $q_z = 0$ which allows equation 3.38 to be approximated[†] as

$$P\left(q_{\parallel}\right) = \frac{1}{q_{\parallel}^2}. \qquad\qquad 3.43$$

Figure 3.10 shows the general dependence on θ for the BPA, HDM and DCM confined and interface modes. The probability is normalised for each model at $\cos\theta = 1$ as it is only the shape of the curve that is important. At $\cos\theta = 1$ the final electron parallel wavevector points the same way as the initial one, and at $\cos\theta = -1$ it is in the opposite direction.

The BPA, HDM and DCM interface (IF) modes have exactly the same dependence and are all strongly forward scattering. The DCM confined (bulk) modes, due to the large constant factor $\left([n\pi/L]^2\right)$ in equation 3.42 which flattens the dependence curve, is more velocity randomising in nature, and has the effect of further reducing the average drift velocity.

Balkan *et al* 1989 have measured the drift velocities of electrons in GaAs/Al$_x$Ga$_{1-x}$As multiple quantum wells. Their sample OC82 was an 85Å GaAs well, 100Å Al$_{0.3}$Ga$_{0.7}$As barrier multiple quantum well structure with

---

[†] Again, only for calculation of the angle $\mathbf{k}_{\parallel}'$ makes to $\mathbf{k}_{\parallel}$ after scattering.
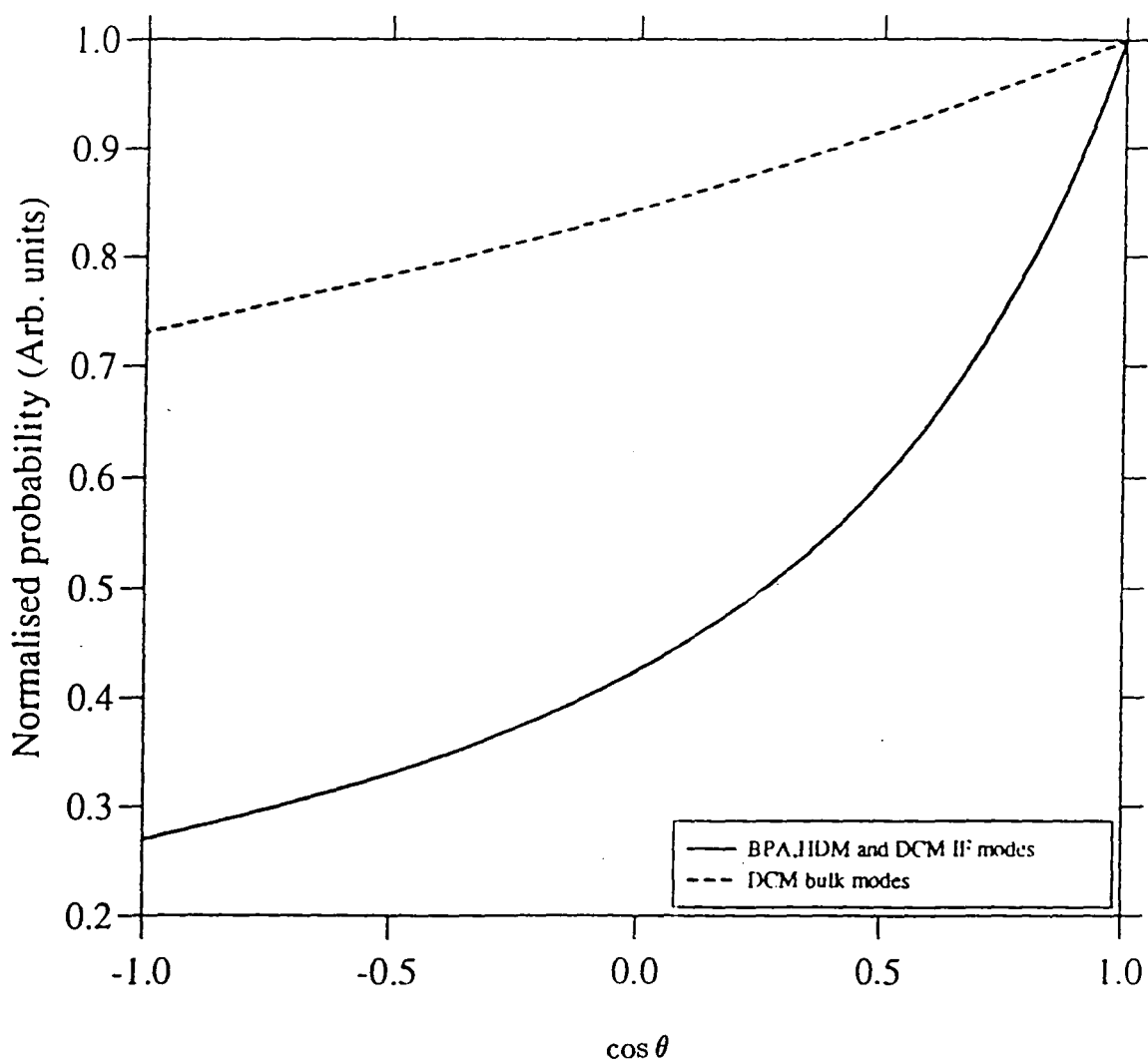
Figure 3.10

Comparison of the scattering angle, θ, dependence of the

BPA, HDM, DCM interface (IF) modes and DCM

confined (bulk) modes.

an electron density in the well of $1.2 \times 10^{10} \mathrm{cm}^{-2}$. The doping density of this sample is relatively small and the well has a width not far removed from our 70Å, and so our results should be comparable. We have plotted their results along side ours in figure 3.8 and, as can be seen, the experimentally determined dependence of drift velocity on electric field is in close agreement with the results for the HDM and BPA simulations.

3.6.2 Scattering events

It is informative to study the microscopic aspects of the electron transport. For example, the number of intra-subband optical phonon absorption and emission events as a percentage of the total scattering events for transitions originating in the ground state, plotted against electric field, are shown in figure 3.11. Each model displays the same characteristic shape; at low fields the absorption and emission events are equal but as the field increases the emission events prevail and the absorption events become a smaller fraction of the total.

Again we see that the BPA and HDM are in close agreement with a similar percentage of each intra-subband scattering event for all fields. The DCM model predicts a larger percentage for both events at low fields but as the strength of the field increases the rise of emission events and fall of absorption events is not as rapid as in the BPA and HDM. The general and specific shape of these curves can be explained with reference to the average energy plot in figure 3.9 and the scattering rate plot in figure 3.6. At low fields the average energy is well below the threshold for phonon
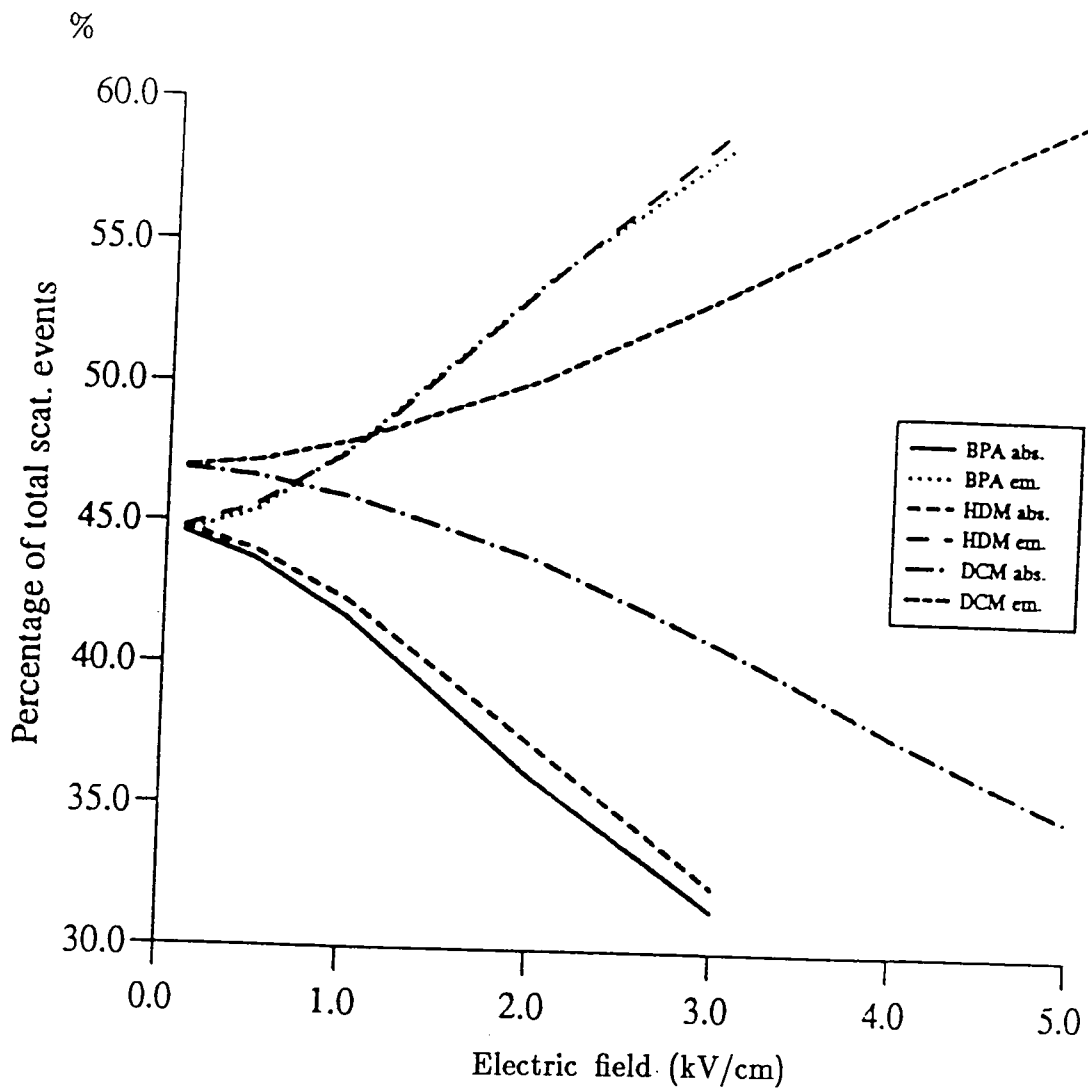
Figure 3.11

Comparison of absorption (abs.) and emission (em.) events

from each phonon model simulation

emission ($\approx$ 36meV) and so electrons have to absorb a phonon before being able to emit one and so the number of absorption and emission events are roughly equal. As the field increases more electrons reach energies where they are able to emit a phonon without having to absorb one first and as the emission rate is $\approx$ 4.3 times the absorption rate[†] there is a greater percentage of phonons emitted than absorbed. The results for the BPA and HDM are in close agreement because their scattering rates are similar for the range of electron energies studied. The DCM predicts higher LPO scattering rates and so there are a greater percentage of these events. In the DCM, as the scattering rates are so high, the energy is suppressed and larger fields are needed for the electrons to reach equivalent BPA and HDM simulation electron energies. As it is the energies that are important when considering the relative percentages of LPO phonon scattering events, this explains the slower change in relative proportions of each event for the DCM in figure 3.11.

[†] $\frac{N_q+1}{N_q} \approx 4.3$

3.7   Conclusion.

Three continuum phonon models for quantum well heterostructures, the bulk phonon approximation, the dielectic continuum model and the hydrodynamic model, have been used to calculate scattering rates and velocity field curves for a 70Å AlGaAs/GaAs quantum well at 300K. We have shown that the BPA and the HDM predict similar transport effects, which are in agreement with experimental results, but the DCM model gives rather higher electron scattering rates and a lower mobility.

Heterostructure phonon theory is a rapidly developing field, and there are now new models predicting phonon modes with longitudinal and transverse components which also obey both mechanical and electromagnetic boundary conditions. These new continuum phonon models couple together interface and confined modes and give excellent agreement with microscopic models. Therefore, further simulations are now required to investigate the transport properties of electrons in quantum well heterostructures when the scattering rates are calculated using phonon modes derived from these new models. Until then, the BPA appears to provide an adequate model for use in transport calculations.

References for chapter three.

Adachi S. 1985 *J. Appl. Phys.* **58** R1

Babiker M. 1986 *J. Phys. C: Solid State Phys.* **19** L339

Balkan N., Gupta R., Ridley B. K., Emeny M., Roberts J., and Goodridge I. 1989 *Solid State Electron.* **32** 1641

Bastard G. 1983 *Appl. Phy. Lett.* **43** 591

Bastard G. 1988 *Wave Mechanics Applied to Semiconductor Heterostructures*

Born M. and Huang K. 1954 *Dynamical Theory of Crystal Lattices* Clarendon, Oxford.

Casey (Jnr.) H. C. and Panish M. B. 1978 *Heterostructure Lasers Part B: Operating Characteristics* Academic Press, New York.

Chamberlain M. P. 1987 *MSc Thesis* Essex University, unpublished.

Chamberlain M. P. 1990 *Phd Thesis* Essex University, unpublished.

Chamberlain M. P., Hoare D., Kelsall R. W., and Abram R. A. 1992 *Semicond. Sci. Technol.* **7** B45

Fuchs R. and Kliewer K. L. 1965 *Phy. Rev.* **140** A2076

Haupt R. and Wendler L. 1991 *Phys. Rev. B* **44** 1850

Huang K. and Zhu B. 1988 *Phys. Rev. B* **38** 13377

Kelsall R. W. 1989 *PhD Thesis* Durham University, unpublished

Kelsall R. W., Wood A. C. G., and Abram R. A. 1991 *Semicond. Sci. Technol.* **6** 841

Kelsall R. W., Wood A. C. G., and Abram R. A. 1992 *Semicond. Sci. Technol.* **6** B312

Landolt-Börnstein 1982 *Numerical Data and Functional Relationships in Science and Technology* ed. O. Madelung, vol. III/17a. Springer-Verlag, Berlin.

Littlejohn M. A., Hauser J. R., and Glisson T. H. 1977 *J. Appl. Phys.* **48** 4587

Molinari E., Baroni S., Giannozzi P., and de Gironcoli S. 1992 *Phys. Rev. B* **45** 4280

Price P. J. 1981 *Ann. Phys.* **133** 217

Ren S. F., Chu Y. C., and Chang Y. C. 1989 *Phys. Rev. B* **40** 3060

Riddoch F. A. and Ridley B. K. 1983 *J. Phys C: Solid State Physics* **16** 6971

Ridley B. K. 1982 *J. Phys C: Solid State Physics* **15** 5899

Ridley B. K. 1989 *Phys. Rev. B* **39** 5282

Ridley B. K. 1993 *Phys. Rev. B* **47** 4592

Rogers D. C. and Nicholas R. J. 1985 *J. Phys. C* **18** L891

Rücker H., Molinari E., and Lugli P. 1992 *Phys. Rev. B* **45** 6747

Rudin S. and Reinecke T. L. 1990 *Phys. Rev. B* **19** 7713

Tanimoto H., Yasuda N., Taniguchi K., and Hamaguchi C. 1988 *Jpn. J. Appl. Phys.* **27** 563

Webber G., de Paula A. M., and Ryan J. F. 1991 *Semicond. Sci. Technol.* **6** 397

Weisbuch C. and Vinter B. 1991 *Quantum Semiconductor Structures: Fundamentals and Applications* Academic Press, New York.

Zianni X., Butcher P. N., and Dharssi I. 1992 *J. Phys. Condens. Matter* **4** L77

CHAPTER FOUR

SIMULATION OF ELECTRON TRANSPORT IN

$In_{0.15}Ga_{0.85}As/GaAs$ QUANTUM WELLS

4.1 Introduction.

In recent years high electron mobility transistor (HEMT) development has turned towards the inclusion of a strained $In_xGa_{1-x}As$ $(x \leq 25\%)$ layer within the conventional AlGaAs/GaAs device. The channel alloy layer is pseudomorphically grown between the GaAs buffer and AlGaAs supply layers, and has to be thin enough (≤ 150Å) that no defects, due to strain, occur. The incorporation of the layer is intended to provide better control over the electrons in the conducting channel and to increase carrier velocity. Improved control is attained due to the 'back barrier' introduced by the conduction band discontinuity between the lower band gap InGaAs layer and the GaAs substrate. Increased carrier velocity is hoped for in the low field regions of the channel because InGaAs alloy has a lower Γ valley effective mass than GaAs. Although the transport simulations of electrons in bulk

strained InGaAs show a mobility reduced from that of bulk GaAs (chapter two), we need also consider effects on the transport properties arising from the quantum confinement of the carriers.

In the conventional HEMT, the band bending due to charge transfer generally introduces a triangular well region at the AlGaAs/GaAs interface, in which the electrons exist in subbands due to quantisation of energy associated with confinement. In the pseudomorphic HEMT, the strained layer is sufficiently thin that the subband structure is determined by the conduction band discontinuities between the channel layer and the supply and buffer layers (see figure 4.1). However, in Monte-Carlo simulations of heterojunction devices such as HEMTs (Kelsall & Abram 1992, Kim *et al* 1991, Dollfus *et al* 1992, Jensen *et al* 1991), it is common to neglect the effects of quantisation on the carriers and treat them as classical particles. This simplifies the model and therefore reduces computation time.

Quantisation effects have been taken into account when calculating the mobility of electrons in triangular wells, such as would be found at the supply-layer/conducting-channel interface (Walukiewicz *et al* 1984, Lee *et al* 1983), and for double heterostructure wells (Brum & Bastard 1985, Thobel *et al* 1993). However these workers only consider low fields, for which the electrons remain in confined states and do not discuss the escape of carriers which will occur in an operating HEMT. Monte-Carlo simulations which do include quantisation effects in HEMTs, triangular quantum wells (Artaki & Hess 1988, Park & Brennan 1988, 1989, 1990, Kobayashi *et al*
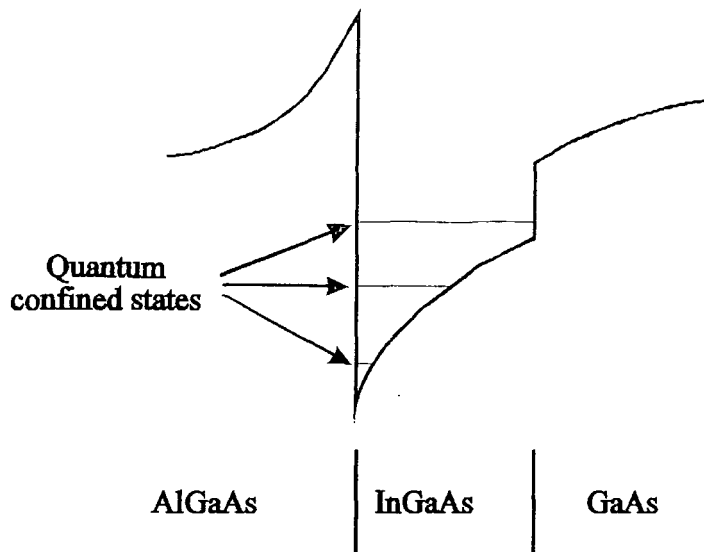
a) Pseudomorphic HEMT
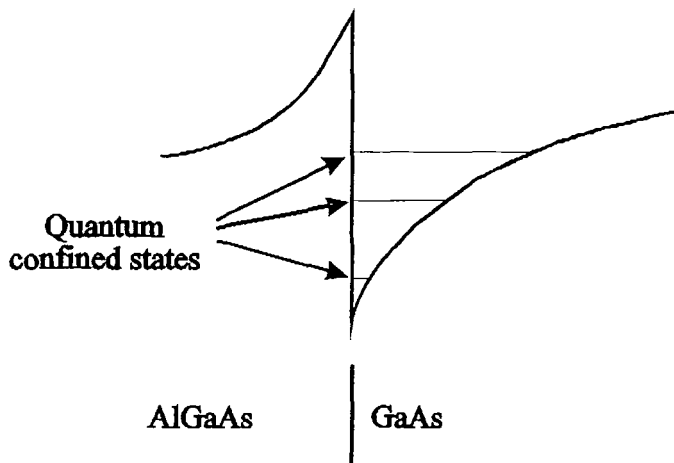
b) Convensional HEMT

Figure 4.1

Schematic diagram of the conduction band edge of,

a) a pseudomorphic AlGaAs/InGaAs/GaAs HEMT,

and b) a conventional AlGaAs/GaAs HEMT.

1989), and double heterostructure wells (Chamberlain *et al* 1992, Crow *et al* 1992, Kelsall *et al* 1992, Thobel *et al* 1991) either introduce some effective transition between bound and unbound states or only consider fields low enough that transfer out of the well is improbable.

Electron escape from the well can be considered as a quantum mechanical transition between bound and unbound states of the well, caused by some scattering mechanism such as lattice vibrations after the carrier has been heated by the applied electric field. Carrier capture is the inverse process. Calculations of the rate of capture due to longitudinal polar optical phonon scattering have been performed for a finite square well system by Brum & Bastard 1985. They considered a finite square well within effective mass theory. However, we are not aware of any incorporation of this approach in Monte-Carlo simulations of carrier transport in a semiconductor quantum well.

Most models and simulations of single heterostructures or HEMTs treat the conduction band satellite valleys as bulk-like with no quantisation effects. One notable exception is Kobayashi *et al* 1989, who have included quantum confined states in both the L and X satellite valleys. Simulations of the satellite valleys in double heterostructure wells have been done by Moško & Novák 1989, who made the well regions so large that the electrons could be treated in the classical limit, and Tanimoto *et al* 1988 who have calculated quantised electron states in satellite valleys but did not included any scattering to unbound regions.

We have used the Monte-Carlo method to simulate the response of an ensemble of electrons in the double heterostructure $In_{0.15}Ga_{0.85}As/GaAs$ quantum well system to a range of electric fields applied parallel to the well/barrier interface. All the electrons start in the ground state of the Γ valley well but some of the fields are high enough that transitions to unbound states and scattering to satellite valley states are probable. Full descriptions of the bound and unbound states in all valley wells, and scattering between them, have been included within the effective mass approximation.

In section 4.2 we present the model for the quantum well system, and demonstrate the particular effects of strain. A brief description of the scattering processes that have been considered is given in section 4.3, and an outline of how the scattering rates between bound and unbound states are calculated is presented in section 4.4. Results of three valley simulations showing the effects of strain on the electron transport properties of the quantum well are discussed in section 4.5. The chapter finishes with section 4.6, which gives a brief summary of the conclusions drawn from our work on strained semiconductor quantum wells.

4.2   The quantum well model.

$\mathcal{T}he$ quantum well device we have modelled is a thin layer of $In_{0.15}Ga_{0.85}As$ forming the electron well, grown between two semi-infinite layers of GaAs. Growth is along the (001) crystallographic direction for both well and barrier materials with the lattice constant of $In_{0.15}Ga_{0.85}As$ being larger than that of GaAs. The total device width is $1\mu m$, with the well of width 70Å in the centre. This well layer is sufficiently thin to be pseudomorphically strained and for the familiar electron subbands associated with quasi-two-dimensional structures to exist. Hence the system is one in which the electron transport properties are affected by both strain and size quantisation.

The simulations of electron transport in a bulk alloy, which is artificially strained as if it were a psuedomorphic layer, are reported and discussed in chapter two. Here we consider electron transport in a strained layer, *including the effects of quantisation due to confinement of the electronic states*, and compare the results with the same system in which the effects of strain are artificially left out.

We have simulated electron transport in $In_{0.15}Ga_{0.85}As$/GaAs quantum wells at fields sufficiently large that real space and reciprocal space transfer effects are probable. In order to study these phenomena we have included the electronic states of the three lowest conduction bands of the well and of the barrier materials. The bulk band structure of GaAs, a de-

scription of the effects of strain on the band structure of $In_{0.15}Ga_{0.85}As$, and other relevant material parameters are presented in chapter two. However, since this work has been done we have received data that better fits the experimental transport measurements of $In_{0.53}Ga_{0.47}As$ (Kelsall 1992), and the bandstructure we have used for $In_{0.15}Ga_{0.85}As$ has been calculated from this.

Table 4.1 shows the differences in the data used to simulate transport in bulk $In_{0.15}Ga_{0.85}As$ (chapter two) and the new data used for the simulations reported in this chapter. The effective masses in both cases agree to within 4%, and the valley separations in the quantum well simulations are slightly less, but still within 10% of the bulk simulation figures.

	Bulk data	Quantum well data
Γ valley effective mass	$0.060m_0$	$0.060m_0$
L valley effective mass	$0.238m_0$	$0.233m_0$
X valley effective mass	$0.589m_0$	$0.591m_0$
Γ to L energy separation $\Delta E_{\Gamma L}(eV)$	0.441	0.426
Γ to X energy separation $\Delta E_{\Gamma X}(eV)$	0.687	0.629

Table 4.1

Comparison of the bandstructure data used for bulk simulation of

$In_{0.15}Ga_{0.85}As$ and that used in this chapter.

The band gap of the alloy is smaller than the barrier material and, for this type I interface, the conduction band offset between the well and barrier is $\approx 68\%$ (Ji *et al* 1987). From this information it is possible to determine the energy offsets at all the valley minima using the known inter-valley separations of the well and barrier materials. There are then three groups of quantum well to be considered; those at the Γ, L and X points.

All the conduction band valley minima for the bulk materials have been taken as spherically symmetric with parabolic E-k dependences, except for the Γ valley of the strained alloy, which has constant energy surfaces that are ellipsoids of revolution ($m_{\perp}^{*} = 0.071 m_o$ compared to $m_{\parallel}^{*} = 0.064 m_o$).

Valley	Parallel effective mass $m_{\parallel}^{*}$ (in m_o)			Well depth (eV)		Number of bound states at $k_{\parallel} = 0$	
	Barrier	Well					
		Unstrnd	Strnd	Unstrnd	Strnd	Unstrnd	Strnd
Γ	0.067	0.060	0.064	0.1492	0.1106	2	
L	0.2320	0.2328		0.0529	0.0552	2	
X	0.5800	0.5913		0.0422	0.128	2	4

Table 4.2

Comparison of the unstrained (Unstrnd) and strained (Strnd) $In_{0.15}Ga_{0.85}As/GaAs$ quantum well bandstructure.

Figure 4.2 and Table 4.2 show the differences in the strained and unstrained band structure of the quantum well device. As was explained in chapter two, the isotropic component of the strain reduces the inter-valley energy separation, with the Γ and L minima increasing, and the X points reducing in energy. Therefore, in the strained layer, the potential well at the Γ point diminishes and those at the X and L points deepen. The X4 valleys are further reduced in energy, increasing their well depth, due to the X valley splitting caused by the uniaxial component of strain. We have included in our bandstructure model only the X4 valleys of the strained well material as the X2 valleys are increased in energy so much that the well disappears. Furthermore, the electron population of the X2 valleys for the fields we consider was shown to be negligible for simulation of electron transport in the bulk material (chapter two).

As explained in chapter three, the depth of a quantum well changes with in-plane wavevector due to the different effective masses of the well and barrier materials. The change with the parallel electron wavevector relative to the valley minima, $k_{\parallel}$, of the potential wells in both the strained and unstrained structures have the same general trends. The parallel Γ valley effective mass in the alloy is less than in the barrier and so, as with the AlGaAs/GaAs well described in chapter three, the depth of this well decreases with increasing $k_{\parallel}$. Conversely the satellite valley effective masses are lighter in the barrier than in the well, and so these wells deepen as $k_{\parallel}$ increases.
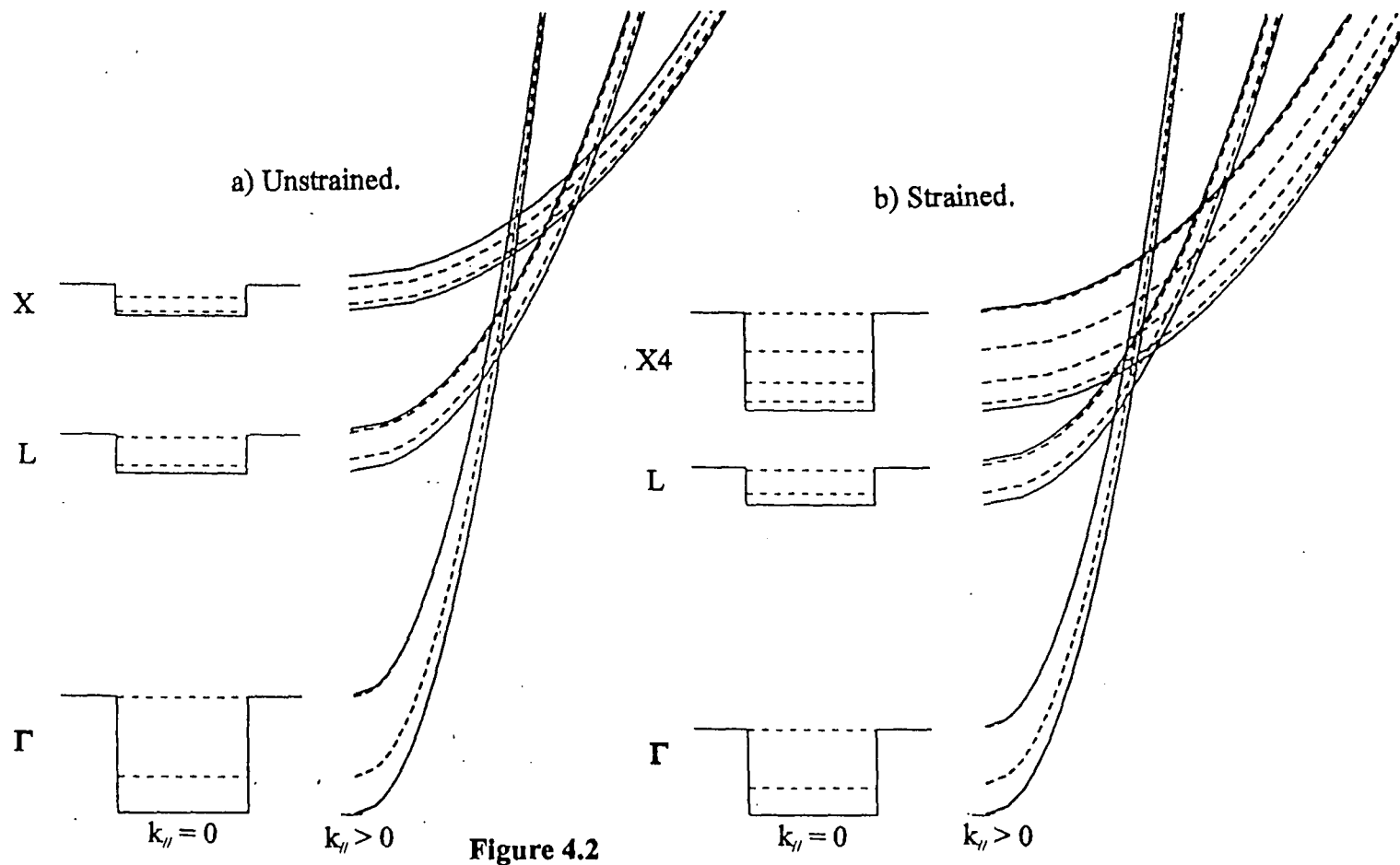
a) Unstrained.

b) Strained.

X

L

Γ

X4

L

Γ

$k_{//} = 0$

$k_{//} > 0$

$k_{//} = 0$

$k_{//} > 0$

Figure 4.2

The conduction bandstructure of a) the unstrained and, b) the strained $In_{0.15}Ga_{0.85}As/GaAs$ quantum well showing the energy separation of the valleys and the parallel wavevector, relative to the valley minima, dependence of the confined states.

It is assumed that the GaAs doping density is low and the In$_{0.15}$Ga$_{0.85}$As is undoped. It is therefore appropriate to model the quantum well system in the flat band limit, as in chapter three. We have solved Schrödinger's equation for the subbands of the wells using the effective mass approximation. With our simple model of the conduction band and electron states we are unable to include effects on the energy levels due to the interaction of equivalent and non-equivalent valley states. More complex band structure calculations, such as the pseudopotential method, can offer a description of these effects but are beyond the scope of this work.

There are two bound states at the valley minima ($k_{\parallel} = 0$) in the Γ, L and X wells of the unstrained layer. The first excited state in the Γ valley well is unbound for $k_{\parallel} \geq 0.054\text{Å}^{-1}$, conversely, due to the increasing well depth of the X valley wells a third state becomes bound for $k_{\parallel} \geq 0.274\text{Å}^{-1}$. The strained layer has two bound states at $k_{\parallel} = 0$ for the Γ and L valleys and four in the X4 valley wells. The first excited state in the Γ valley is unbound for $k_{\parallel} \geq 0.031\text{Å}^{-1}$.

Two models for the unbound electron states are used, depending on the process of interest. For scattering between a bound and an unbound state, the unbound state is obtained by solving the finite square well problem of the well-barrier structure, within the effective mass theory. For a given energy there will exist two unbound states which correspond to a carrier moving along the z axis from the left to the right or vice versa. We consider symmetric and anti-symmetric combinations of these states to form

standing waves with parities similar to the bound states of a well, as shown in figure 4.3. This is a common way to treat unbound electron states in the calculation of scattering rates. However, for electron scattering between unbound states or in the simulation of the transport of an unbound electron the effects of the well region are neglected, and the state is treated as a bulk barrier state. This is a good approximation as the well region is only 0.7% of the total device width.

4.3   Scattering events.

*R*_{oom} temperature simulations of electron transport in a quantum layer device are carried out with electron scattering via longitudinal polar optical phonons, acoustic phonons, non-polar optical phonons in the L valleys, inter-valley phonons described in the deformation potential approximation and alloy scattering due to the fluctuations of the well material crystal potential. All phonon scatterings explicitly include emission and absorption events except for scattering via acoustic phonons which is treated in the elastic approximation. The two mode phonon behaviour of $In_{0.15}Ga_{0.85}As$ has been approximated to one average mode as in chapter two. Bulk phonon approximations are used to describe all types of phonon scattering. Scattering processes involving one or two bound states are considered due to phonons of the bulk well material. The results of chapter three suggest
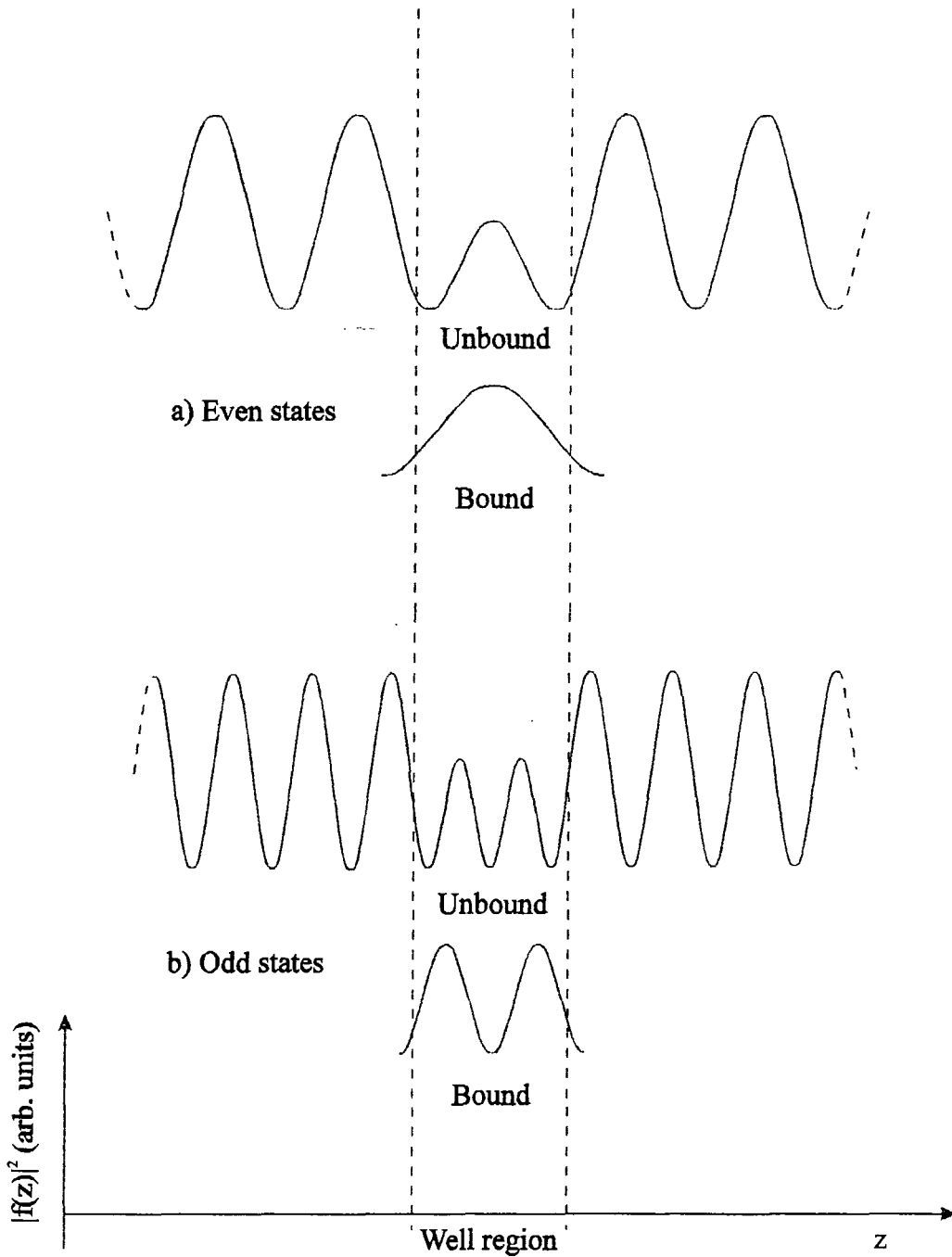
Figure 4.3

Comparison of the modulus of the envelope function squared ($|f(z)|^2$), against z around the well region, for bound and unbound, odd and even states.

that this approach is a reasonable approximation. The scattering between

unbound electron states is taken as via bulk barrier material phonons. This

is expected to be a good approximation because the unbound electrons are

in states that extend throughout the system and the barrier makes up 99.3%

of the total device.

Alloy scattering in the two dimensional system is modelled in a

similar way as for bulk materials. The scattering is caused by a sum

of short range potentials, randomly arranged within the lattice, that are

deviations from the averaged crystal potential. Alloy scattering rate, P_{alloy},

involving bound states is described as (Walukiewicz *et al* 1984, Bastard

1984)

$$P_{alloy} = \frac{(\Delta U)^2 x (1 - x) a_o^3}{4\hbar} \frac{k_{\parallel f}}{\left| \frac{\partial E_f}{\partial k_{\parallel f}} \right|} \int \left| f'(z) \right|^2 \left| f(z) \right|^2 dz \qquad 4.1$$

where ΔU ($= 0.42\text{eV}$), the alloy scattering potential, acts over a region which

has the volume of the primitive unit cell. If scattering to all subbands is

considered in the limit of an infinitely wide quantum well, equation 4.1

reduces to the expression for the bulk scattering rate calculated under the

same assumptions. x is the concentration of indium and a_o is the lattice

constant of the alloy. $k_{\parallel f}$ is the final parallel electron wavevector, $\left| \frac{\partial E_f}{\partial k_{\parallel f}} \right|$

is the conversion factor to change from an energy to a wavevector delta

function, and $f(z)$, $f'(z)$ give the z dependences of the initial, final electron

wavefunctions respectively.

In the system considered here only the well material is a ternary

alloy, therefore only those parts of the electron wavefunction inside the well region contribute to the scattering rate. That is, the z integral in equation 4.1 is only over the well width. The interaction of unbound electron states with the random alloy potential of the well is negligible due to the small percentage of electron probability inside the well region.

Because the structures have low doping, the remote ionised impurity scattering of bound electrons and the ionised impurity scattering of unbound electrons can be neglected, and the effects due to interface roughness are negligible. Piezoelectric scattering of electrons has not been included as it is only significant at low temperatures.

All the possible scattering events, both intra- and inter-valley, between the bound and unbound states of the three quantum well valleys have been included, except for alloy scattering of unbound electron states. It is apparent from the description of the electron states and the scattering processes included in our model that there are a large number of transitions possible for every electron state. For example, a bound electron in an L valley can be scattered in 50 different ways.

Scattering between two bound subbands has been discussed in chapter three. The scattering between two unbound states is treated as for the bulk barrier material. It remains to give details of the description of scattering between bound and unbound states.

4.4   Phonon scattering between bound and unbound states.

$\mathcal{S}$*tarting* from Fermi's Golden rule, the generalised formula for a bulk phonon mode scattering a quantum well electron state from **k** to **k'** can be obtained as (Kelsall 1989)

$$P\left(\mathbf{k},\mathbf{k}'\right) = \frac{2\pi}{\hbar}\frac{\Omega}{(2\pi)^3}\int C^2(q)\left\{\begin{matrix} N_q \\ N_q+1 \end{matrix}\right\}\left|I(\mathbf{k}',\mathbf{k})\right|^2 \delta\left(E_{k'}-E_k \mp \epsilon_{ph}\right)d\mathbf{q}, \quad 4.2$$

where the matrix element is defined thus:-

$$I(\mathbf{k}',\mathbf{k}) = \int \psi_{k'}^* e^{\pm i\mathbf{q}\cdot\mathbf{r}}\psi_k \, d\mathbf{r}. \qquad 4.3$$

In equations 4.2 and 4.3, the upper options are for absorption with the lower options for emission of a phonon. $C(q)$ is a function of the phonon wavevector **q** and is dependent on the mode of phonon involved in the scattering, N_q is the phonon mode occupation number, E_k, $E_{k'}$, and ϵ_{ph} are the initial and final electron state energies, and the phonon energy respectively. The initial and final electron state wavefunctions are designated by ψ_k and $\psi_{k'}$ respectively, and are functions of the form:-

$$\psi_k = \frac{1}{\sqrt{A}}u_k(r)f(z)e^{i\mathbf{k}_\parallel \cdot \mathbf{x}_\parallel}, \qquad 4.4$$

where A is the area of the well plane, $u_k(r)$ is the periodic part of the bulk Bloch function, and $f(z)$ describes the z dependence of the wavefunction.

If the wavefunctions of equation 4.4 are substituted into the expression for $I(\mathbf{k}',\mathbf{k})$ and the periodic function $u_{k'}^*(r)u_k(r)$ is expanded as a

Fourier series over reciprocal lattice vectors, g,:

$$I(\mathbf{k}',\mathbf{k}) = \sum_{\mathbf{g}} c_{\mathbf{g}} \frac{(2\pi)}{A} \delta(\mathbf{k}_{\parallel} - \mathbf{k}'_{\parallel} \pm \mathbf{q}_{\parallel} + \mathbf{g}_{\parallel}) \int f'^{*}(z) e^{i(\pm q_z + g_z) \cdot z} f(z) dz, \qquad 4.5$$

where $c_{\mathbf{g}}$ are the coefficients of the Fourier series defined as:-

$$c_{\mathbf{g}} = \frac{1}{V_{\text{cell}}} \int_{\text{cell}} u_{k'}^{*}(r') u_k(r') e^{-i\mathbf{g}\cdot\mathbf{r}'} d\mathbf{r}'. \qquad 4.6$$

As the smallest non-zero value of $\mathbf{g}_{\parallel}$ is much larger than $\mathbf{k}_{\parallel}$ and $\mathbf{q}_{\parallel}$, the argument of the delta function can vanish only if $\mathbf{g}_{\parallel} = 0$, retaining only the term with $\mathbf{g} = 0$. The probability of scattering from a state $\mathbf{k}$ to state $\mathbf{k}'$ follows from equation 4.2 as

$$P\left(\mathbf{k},\mathbf{k}'\right) = \frac{2\pi}{\hbar} \frac{\Omega}{(2\pi)^3} \int C^2(q) \left\{ \begin{matrix} N_q \\ N_q + 1 \end{matrix} \right\} \left| J(k'_z, q_z) \right|^2 \left| G(\mathbf{k}',\mathbf{k}) \right|^2$$

$$\times \frac{(2\pi)^2}{A} \delta(\mathbf{k}_{\parallel} - \mathbf{k}'_{\parallel} \pm \mathbf{q}_{\parallel}) \delta\left(E_{k'} - E_k \mp \epsilon_{ph}\right) d\mathbf{q}, \qquad 4.7$$

where $G(\mathbf{k}',\mathbf{k})$ is the overlap integral;

$$G(\mathbf{k}',\mathbf{k}) = \frac{1}{V_{\text{cell}}} \int_{\text{cell}} u_{k'}^{*}(r') u_k(r') dr', \qquad 4.8$$

and, $J(k'_z, q_z)$ is the envelope function integral over z on the right hand side of equation 4.5:

$$J(k'_z, q_z) = \int f'^{*}(z) e^{\pm i q_z z} f(z) dz. \qquad 4.9$$

Making the standard assumption that the functions $u_k(r)$ can be approximated by the zone centre Bloch functions, $\left| G(k'_z, k_z) \right|^2$ is unity for all transitions. Integrating over $\mathbf{q}_{\parallel}$ in equation 4.7 gives

$$P\left(\mathbf{k},\mathbf{k}'\right) = \frac{L_z}{\hbar} \int_{-\infty}^{+\infty} C^2(q_{\parallel}, q_z) \Big|_{q_{\parallel} = |\mathbf{k}_{\parallel} - \mathbf{k}'_{\parallel}|} \left\{ \begin{matrix} N_q \\ N_q + 1 \end{matrix} \right\}$$

$$\times \left| J(k'_z, q_z) \right|^2 \delta\left(E_{k'} - E_k \mp \epsilon_{ph}\right) dq_z. \qquad 4.10$$

To find the total probability for an electron to be scattered from state **k** by a phonon process (with properties defined by $C(q)$), $P(\mathbf{k}, \mathbf{k}')$ must be integrated over all possible final electron states. The number of these final states is determined by considering whether the scattering is to a bound or an unbound state.

4.4.1 Scattering from a bound state to an unbound state

The total rate of scattering of an electron in a state **k** by a phonon of wavevector **q**, to any unbound state **k**' is given by:-

$$P_{\text{scat}} = \frac{\Omega}{(2\pi)^3} \int P(\mathbf{k}, \mathbf{k}') d\mathbf{k}' \qquad\qquad 4.11$$

where the integral is over all possible final states **k**'.

Now $d\mathbf{k}'$ can be written in spherical polar coordinates as

$$d\mathbf{k}' = k'^2 \sin\theta \, dk' d\theta d\phi \qquad\qquad 4.12$$

where the origin of θ is along the z axis (growth direction), and that of ϕ along the in-plane component of the initial wavevector. Hence θ is the angle between k' and k_z and ϕ is the angle between $k'_{\parallel}$ and $k_{\parallel}$. The components of k' are given by

$$k'_z = k' \cos\theta, \qquad\qquad 4.13.a$$

$$k'_x = k' \sin\theta \cos\phi, \qquad\qquad 4.13.b$$

$$k'_y = k' \sin\theta \sin\phi. \qquad\qquad 4.13.c$$

Changing from an energy delta function to a wavevector delta function using

$$\delta(E' - E_f) = \frac{\delta(k' - k_f)}{\left|\frac{\partial E'}{\partial k'}\right|},$$

4.14

where k_f is the well material wavevector which satisfies

$$k_f = \sqrt{\frac{2m_w^* E_f}{\hbar^2}},$$

4.15

and $E_f(= E \pm \epsilon_{ph})$ is measured from the well minimum. In equation 4.15 the effective mass appropriate to the final state is approximated by that of the well, m_w^*. The barrier wavevector component of the final wavefunction in the scattering rate is automatically picked out by the definition of k_z in the barrier as shown in figure 4.4 (a). P_{scat} becomes

$$P_{\text{scat}} = \frac{L_z m_w^*}{\hbar^3} \frac{\Omega}{(2\pi)^3} \left\{ \begin{matrix} N_q \\ N_q + 1 \end{matrix} \right\} \int_0^\pi \int_0^{2\pi} \int_0^{+\infty} \int_{-\infty}^{+\infty} C^2(q_\parallel, q_z) \Big|_{q_\parallel = \left| k_\parallel - k'_\parallel \right|}$$
$$\times \left| J(k'_z, q_z) \right|^2 \delta \left(k' - k_f \right) dq_z k' dk' \sin\theta d\theta d\phi.$$

4.16

For scattering to parabolic bands

$$\left| \frac{\partial E'}{\partial k'} \right| = \frac{\hbar^2 k'}{m_w^*}.$$

4.17

The delta function now gives us limits to the integral over θ (see figure 4.4). There are two regions in which scattering is possible, those for $\theta = 0$ to $\theta_{\max}$ and $\theta = \pi - \theta_{\max}$ to π. Where $\theta_{\max}$ is defined as the largest possible angle for which the z component of the barrier wavefunction is still real. This gives then for the generalised rate for scattering to unbound

Well and barrier
wavevector
components of one
unbound state.
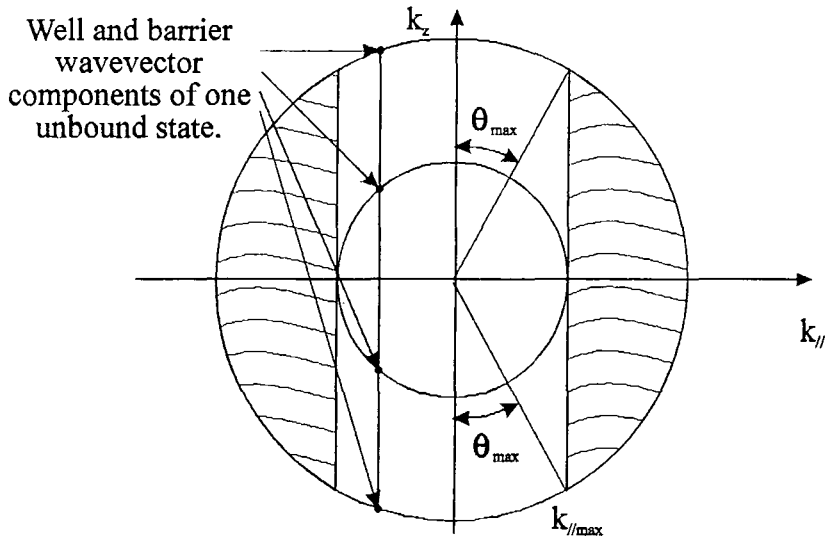
a) Equal energy lines for the bulk well and barrier materials showing the

limits to the integral over θ. Also shown are the wavevector components of

one possible final state and the maximum allowed value of parallel

wavevector ($k_{//max}$).
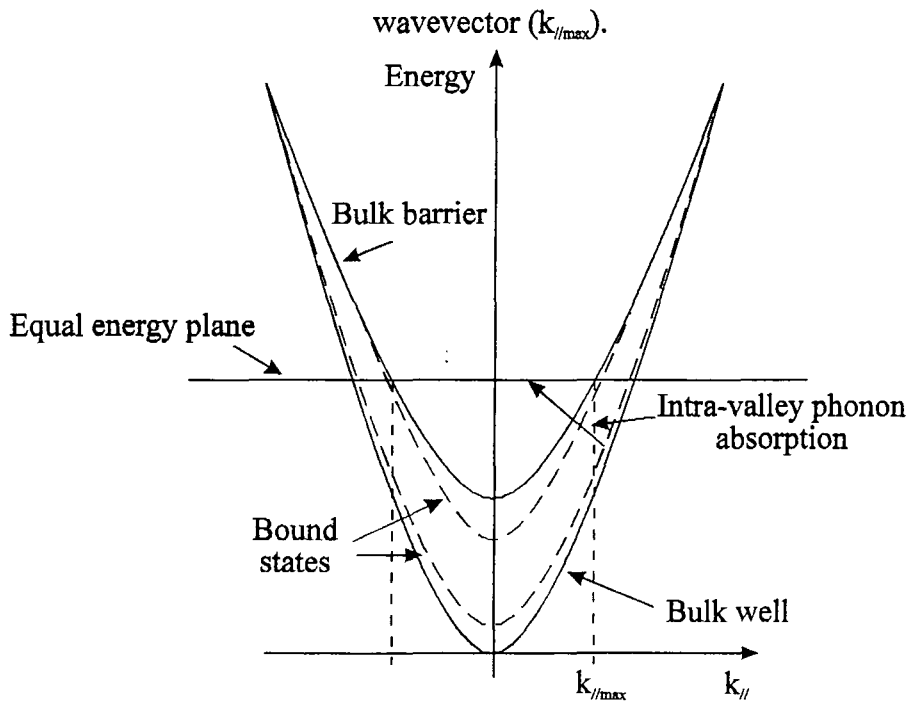
b) The E-$k_{//}$ diagram showing the bulk well and barrier materials' band edge

and the bound states of the well. The equal energy surface of all possible

unbound states in (a) is indicated along with a possible scattering event from a

bound state to an unbound one.

Figure 4.4

states,

$$P_{scat} = \frac{L_z m_w^*}{\hbar^3} \frac{\Omega}{(2\pi)^3} \left\{ \begin{matrix} N_q \\ N_q + 1 \end{matrix} \right\} \int_0^{2\pi} \int_{\theta_2}^{\theta_1} \int_{-\infty}^{+\infty} C^2(q_\parallel, q_z) \Big|_{q_\parallel = k_\parallel - k_{\parallel f}}$$
$$\times \left| J(k_{zf}, q_z) \right|^2 dq_z k_f \sin\theta \, d\theta \, d\phi \quad \left\{ \begin{matrix} \theta_1 = 0, & \pi - \theta_{max} \\ \theta_2 = \theta_{max}, & \pi \end{matrix} \right. \quad 4.18$$

Usually the integral over ϕ may be done analytically, but we have found the θ and q_z integrals to be intractable, and have evaluated those numerically.

	$C^2(q)$	N_q
Polar optical phonons	$\frac{e^2 \hbar \omega_{pop}}{2\Omega \varepsilon_0 q^2} \left(\frac{1}{\varepsilon_\infty} - \frac{1}{\varepsilon_s} \right)$	$\left(e^{\frac{\hbar \omega_{pop}}{k_B T} - 1} - 1 \right)^{-1}$
Acoustic phonons	$\frac{\Xi^2 \hbar q}{\rho \Omega v_s}$	$N_q \approx N_q + 1 \approx \frac{k_B T}{\hbar v_s q}$
Non-polar optical phonons	$\frac{\hbar D_{nop}^2}{2\rho \Omega \omega_{nop}}$	$\left(e^{\frac{\hbar \omega_{nop}}{k_B T} - 1} - 1 \right)^{-1}$
Inter-valley phonons	$\frac{Z_f \hbar D_{iv}^2}{2\rho \Omega \omega_{iv}}$	$\left(e^{\frac{\hbar \omega_{iv}}{k_B T} - 1} - 1 \right)^{-1}$

Table 4.3

$C(q)$ and phonon occupation number N_q functions for the

general scattering formula defined in text.

Table 4.3 gives the form of the function $C(q)$ and N_q for polar optical, acoustic, non-polar optical and inter-valley phonon scattering, Where e is the electronic charge, $\omega_x (x = pop, \ nop \ iv)$ are the phonon frequencies for polar optical phonons, non-polar optical phonons and inter-valley phonons respectively, ε_0, ε_∞ and ε_s are the permitivity of free space, high and low

frequency dielectric constants, k_B is Boltzmann's constant, Ξ is the acoustic deformation potential, ρ the material density, v_s the velocity of sound in the material, $D_x(x = nop, iv)$ are the deformation potentials for optical phonon scattering and Z_f is the number of equivalent destination valleys.

4.4.2 Scattering from an unbound to a bound state

We shall now calculate the scattering rate for scattering from an unbound state to one within a well. For scattering to a bound state the z component of the final wavefunction is already determined by the transition process considered, i.e. we are calculating scattering to a specific bound state, and so the sum over all final states is over $\mathbf{k}'_\parallel$ only, thus

$$P_{\text{scat}} = \frac{A}{(2\pi)^2} \int P(\mathbf{k}, \mathbf{k}') d\mathbf{k}'_\parallel. \tag{4.19}$$

Here $d\mathbf{k}'_\parallel$ can be written

$$d\mathbf{k}'_\parallel = k'_\parallel dk'_\parallel d\phi, \tag{4.20}$$

where ϕ is the angle between the initial and final parallel wavevectors.

Following a similar procedure as above we arrive at

$$P_{\text{scat}} = \frac{L_z A}{\hbar (2\pi)^2} \left\{ \begin{matrix} N_q \\ N_q + 1 \end{matrix} \right\} \int_0^{2\pi} \int_0^\infty \int_{-\infty}^{+\infty} C^2(q_\parallel, q_z) \Big|_{q_\parallel = \left| k_\parallel - k'_\parallel \right|}$$
$$\times \left| J(k'_z, q_z) \right|^2 \frac{\delta \left(k'_\parallel - k_{\parallel_f} \right)}{\left| \frac{\partial E'}{\partial k'_\parallel} \right|} dq_z k'_\parallel dk'_\parallel d\phi \tag{4.21}$$

This gives us then the total rate for scattering from an unbound state to a bound state;

$$P_{\text{scat}} = \frac{\Omega}{\hbar(2\pi)^2} \left\{ \begin{array}{c} N_q \\ N_q + 1 \end{array} \right\} \int_0^{2\pi} \int_{-\infty}^{+\infty} k_{\|f}$$

$$\times C^2(q_\|, q_z) \Big|_{|q_\| = k_\| - k_{\|f}|} \frac{\left| J(k_{zf}, q_z) \right|^2}{\left| \frac{\partial E_f}{\partial k_{\|f}} \right|} dq_z d\phi \qquad 4.22$$

As with the bound to unbound state scattering case described above the integral over ϕ is generally straightforward and can be evaluated analytically.

It should be noted that P_{scat} does depend on the angle the initial wavevector makes with the $\mathbf{k}_z$ direction (θ). Since the rate of unbound to bound state scattering is low in comparison with the rate of unbound to unbound state scattering we have made use of a single θ averaged scattering rate in the simulations.

4.4.3 Bound state scattering

Figure 4.5 compares the scattering rates for electrons in the bound states of the Γ valley well of the unstrained and strained layers. Plotted are the rates for intra-valley and inter-valley scattering to bound and unbound states. Below about 0.37eV in the unstrained well, and 0.33eV in the strained well, only intra-valley scattering is present with the dominant rates being intrasubband optical phonon emission and absorption, followed by intrasubband alloy scattering and acoustic phonon scattering in that order. Scattering to the first excited state of the Γ valley occurs only over a
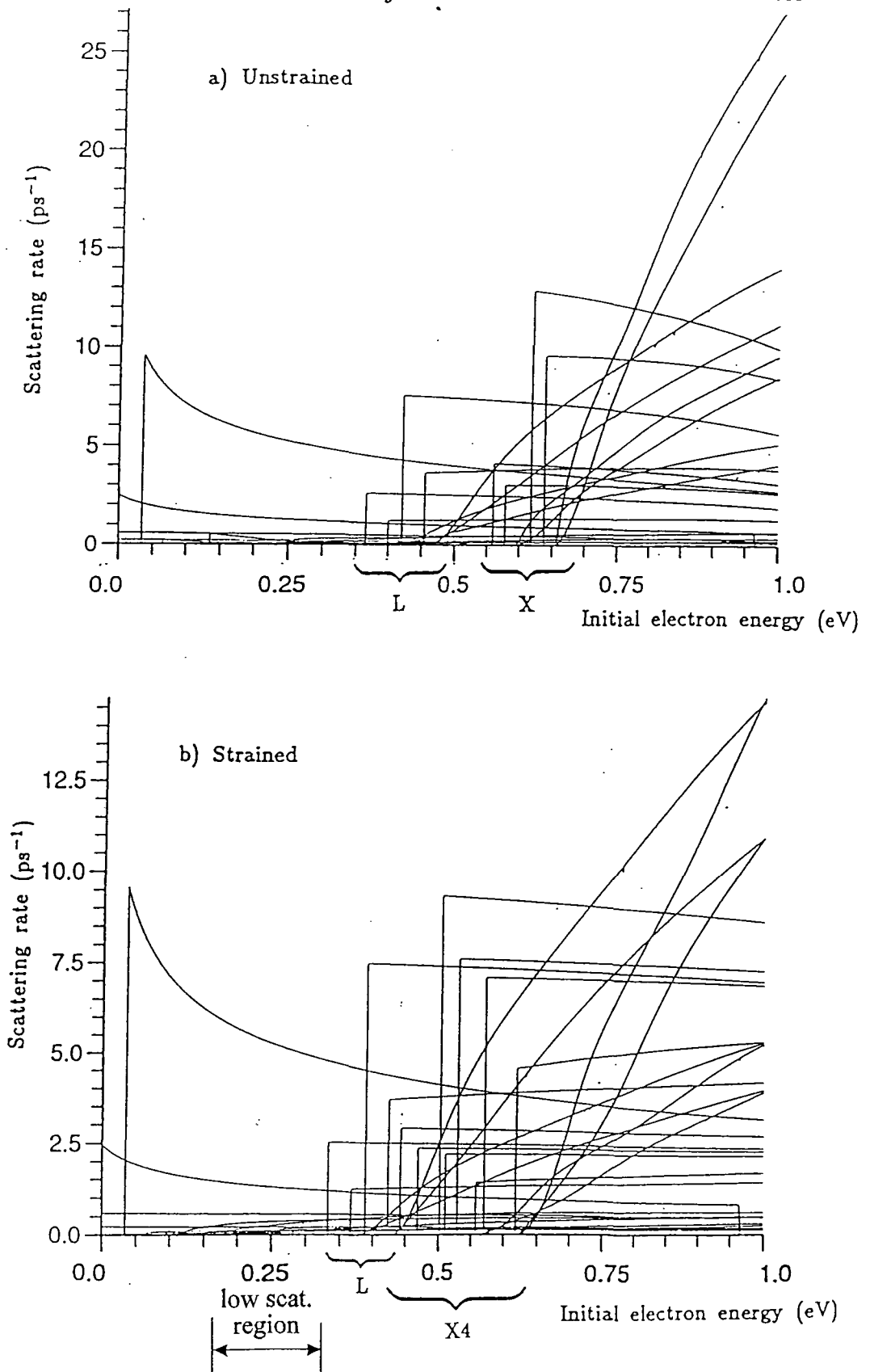
Figure 4.5

The scattering rate against initial energy for electrons in the

ground state of the Γ valley quantum well of the, a) unstrained and,

b) strained system.

limited range of energies because this state becomes unbound at relatively small in-plane wavevector as described in section 4.2. Intra-valley scattering rates for transitions to unbound states are small in comparison with the intra-subband scattering rates.

The destination satellite valleys for the inter-valley rates are indicated in figure 4.5. The curves that have sharp thresholds refer to bound states where the final density of states has a step like form. Those rates which gradually increase from zero are for scattering to unbound states where there is a continuous density of states.

The energy at which scattering to the satellite valleys becomes probable is less in the strained layer case due to the general reduction in inter-valley separation with strain. A consequence of this is that scattering to bound states in the X4 valleys becomes probable around the same energy as scattering to the unbound states in the L valleys. As the X4 valley wells have more bound states than the X valleys of the unstrained system there are more transitions possible to these valleys.

Also note the region between the threshold for intra-subband polar optical phonon emission and inter-valley scattering, where the intra-subband rates are relatively low and so the bound to unbound transitions have a correspondingly higher probability of occurring, which is indicated on the diagram.

4.4.4 Unbound state scattering

Figure 4.6 compares the scattering from an unbound state of the Γ valley well of the strained and unstrained systems. Plotted are the rates for intra-valley scattering via polar optical phonon emission and absorption, elastic acoustic phonon scattering, and inter-valley scattering. The rates for scattering from unbound odd or even states to unbound odd and even states are the same, for any specific process. Scattering to bound states is negligible in comparison. The well constitutes only a small fraction of the total system volume. Since the difference between the strained and unstrained systems is associated only with the well, the results for a strained system are essentially identical to those in figure 4.6.

4.5   Electron transport simulation results.

*W*e have examined how an ensemble of electrons react when subjected to a range of electric fields, from 0.0kVcm^{-1} to 20.0kVcm^{-1}, applied parallel to the well-barrier interface. The transient and steady state response of the electrons has been studied with specific reference to their average drift velocity, average energy and real- and reciprocal-space distributions. All the electrons are in the ground state of the Γ valley well with zero average velocity until the electric field is 'switched on' at time t=0.0ps. Unless otherwise stated all results and discussions refer to the
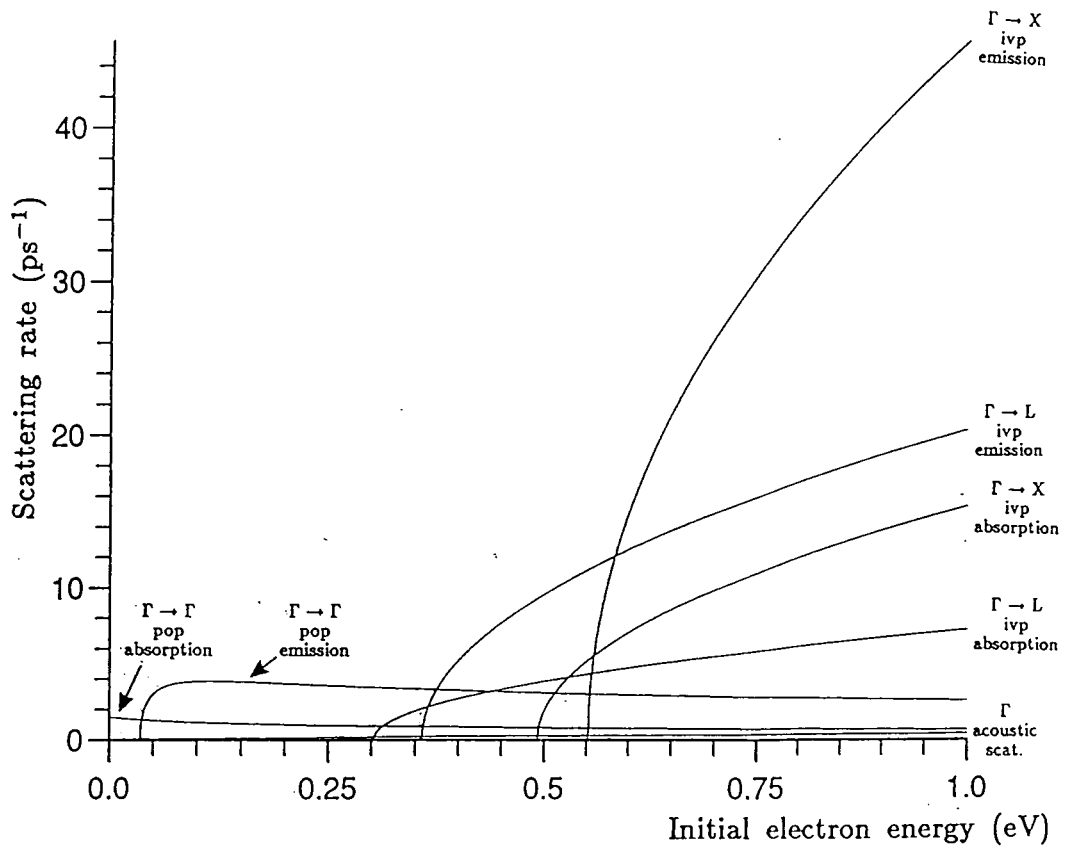
Figure 4.6

The scattering rate against energy for electrons in the even

state of the Γ valley of the unstrained quantum well. The

scattering processes are indicated (ivp = inter-valley phonon,

pop = polar optical phonon).

strained layer system.

4.5.1 Average energy response

The average energy of the electrons, measured from the bottom of the Γ valley well, is plotted for a range of fields against time in figure 4.7. The response has similar basic features for each field strength; the energy increases with time until it reaches some value which it maintains for the rest of the simulation. For low fields the rise in energy is small and the time taken to reach steady state large, but as the field is increased the energy increases more rapidly to a higher value which is achieved in a shorter time. Also it should be noted that the increase in saturation energy for a unit increase in field strength goes through a peak at about 3.0 to 4.0kVcm^{-1}.

The shape of the curves can be explained in terms of the opposing actions of the field, and the carrier scattering. At the start of the simulation, the field is the dominant influence and the electrons rise in energy until the two effects balance. This occurs at larger energies for stronger fields as, generally, the scattering rates are greater at these larger energies. In particular the electrons may scatter to the satellite valleys where the effective masses are greater. Also, for higher fields, the initial rate of energy gain increases and so the electrons more quickly reach energies where they can scatter to the heavier satellite states and a balance is arrived at in a shorter time.

The trend in the curves may be explained with reference to the
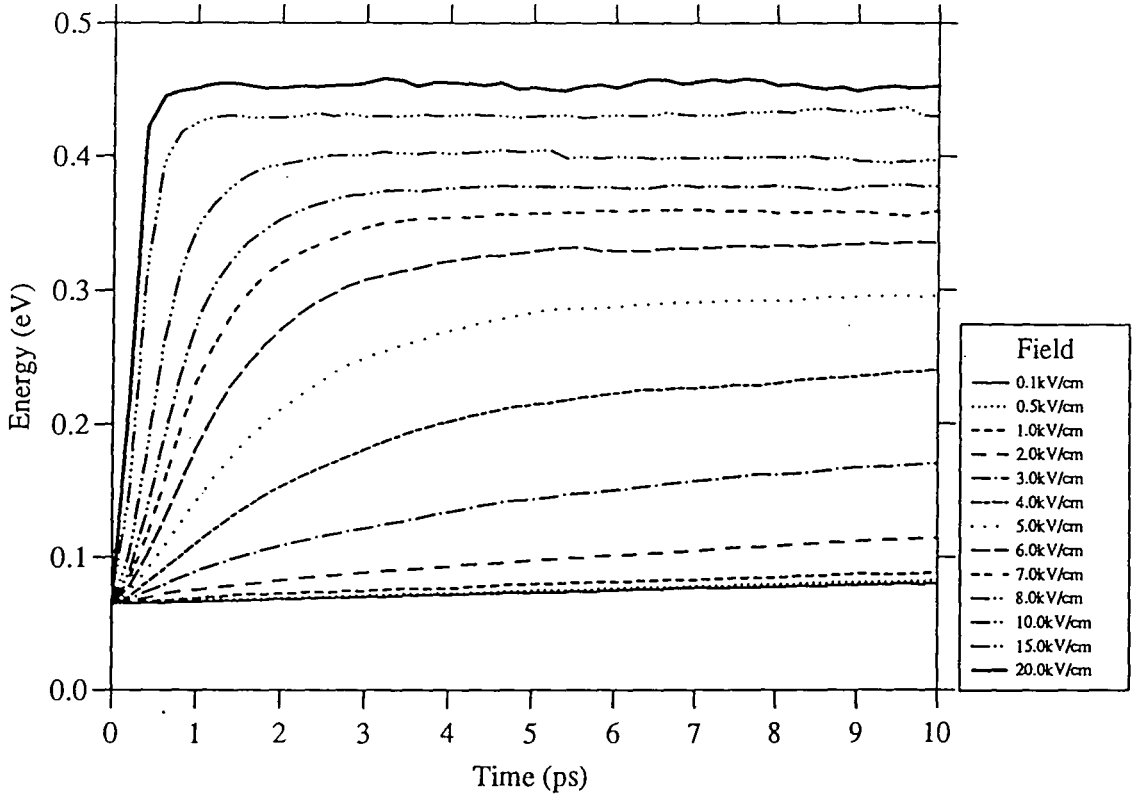
Figure 4.7

Average electron energy, measured from the Γ point minimum of the

well bandstructure, plotted against time for a range of fields (0.1 to

$20.0\mathrm{kVcm}^{-1}$) in the strained $In_{0.15}Ga_{0.85}As/GaAs$ quantum well structure.

scattering rate diagram for the ground state of the Γ valley well, figure 4.5. At the low fields the average energy of the electrons is a little below the threshold for intra-subband phonon emission and so the electrons are inhibited from rising further in energy. As the field is slowly increased the electrons enter an energy region where the intra-valley scattering rates are smaller than at threshold and there is still little probability of making a transition to the satellite valley states. Therefore, in this region, the extra energy gained for an increment in field is larger than at lower fields. This largest rise in energy occurs between 3.0 and 4.0kVcm^{-1}. After this, however, the number of possible scattering events rises considerably because the inter-valley transitions occur readily. This has the effect of repressing any rise in energy, and reducing the increase in energy for a given increment in field.

4.5.2 Transient real- and reciprocal-space distributions

The electron distributions among the bound and unbound states of all the valleys considered are plotted with time for a range of fields in figures 4.8 (a) to 4.8 (j). To show why the states are occupied as they are the average energy as a function of time is plotted on each graph. For low fields ($< 2.0 \text{kVcm}^{-1}$, figures 4.8 (a) to 4.8 (d)) only the Γ valley is occupied although there is a steady leakage of carriers from the well to the barrier (unbound) states. This transfer of carriers continues until the distribution of carriers between the bound and unbound states reaches steady state, which can be after tens of picoseconds. For very low fields $\leq 0.5 \text{kVcm}^{-1}$ the
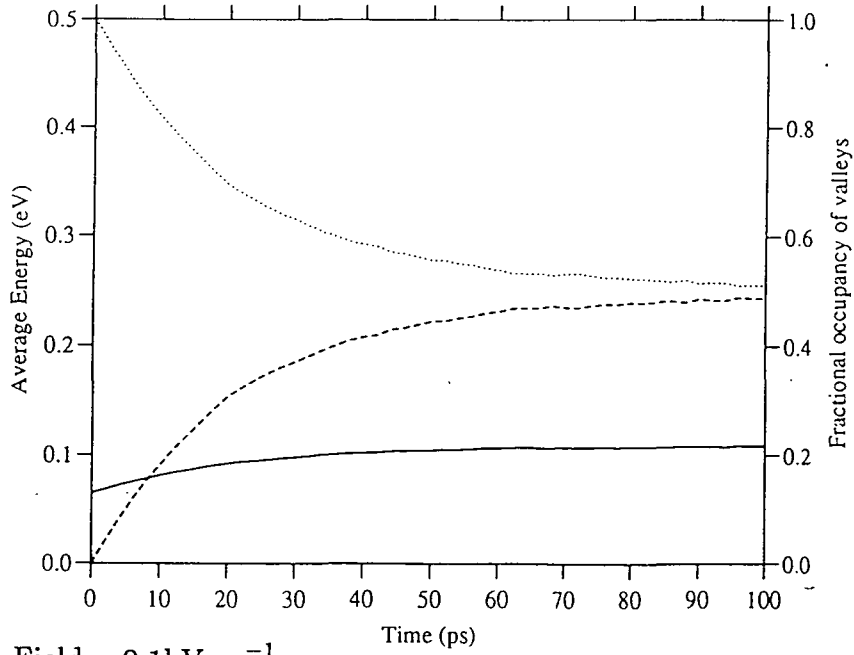
(a) Field $= 0.1 \text{kVcm}^{-1}$
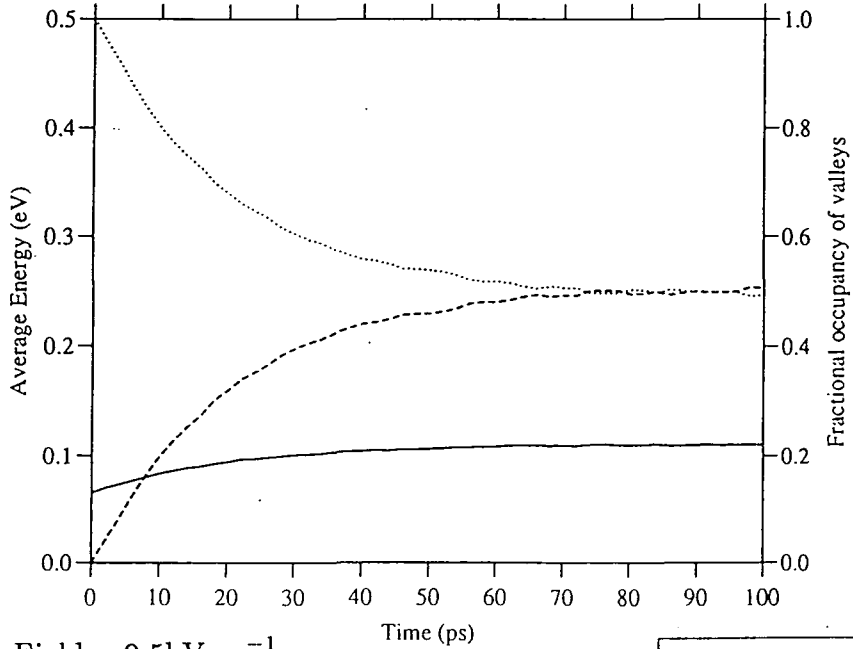
(b) Field $= 0.5 \text{kVcm}^{-1}$
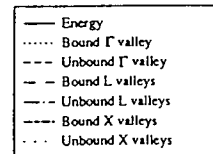
Figure 4.8(a) to (j)

Average electron energy and fractional occupancy of bound and

unbound states in all valleys plotted against time for the strained

$In_{0.15}Ga_{0.85}As/GaAs$ quantum well structure.

(c) Field = 1.0kVcm^{-1}

(d) Field = 2.0kVcm^{-1}

Legend:
- —— Energy
- ········ Bound Γ valley
- – – – Unbound Γ valley
- — — Bound L valleys
- —·— Unbound L valleys
- —··— Bound X valleys
- ··· Unbound X valleys
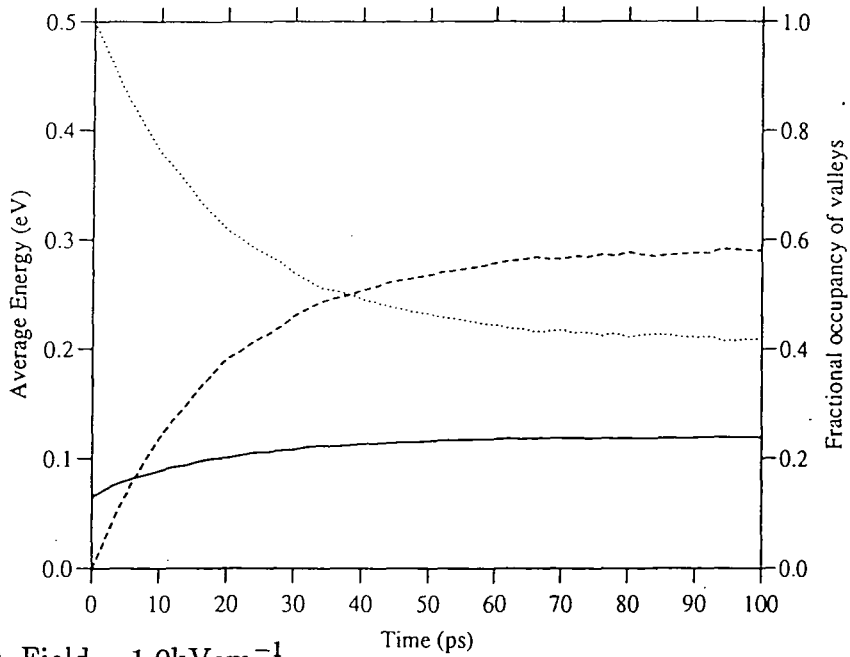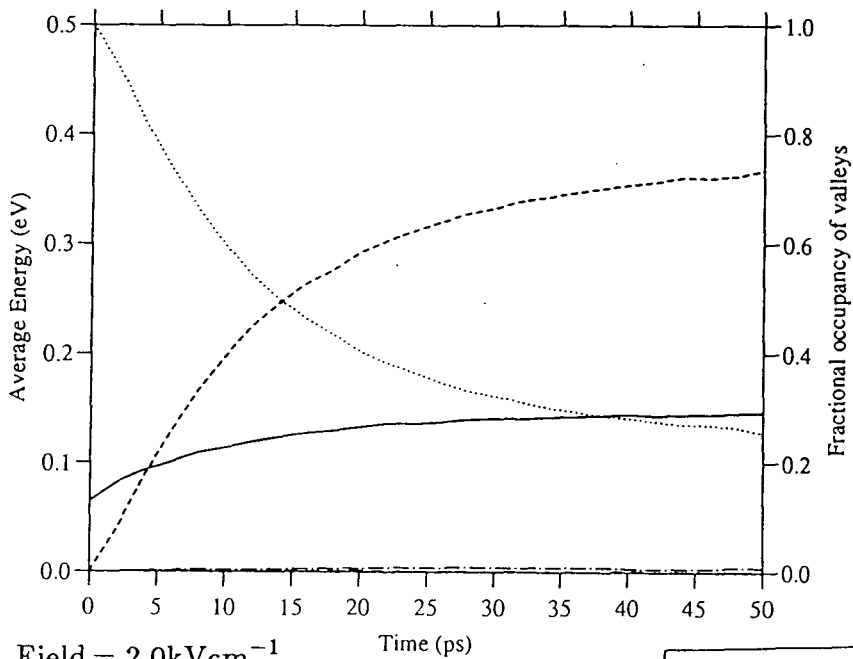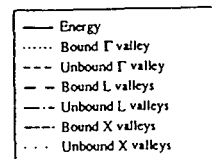
Figure 4.8 (c) & (d)

(c) Field = 1.0kVcm^{-1} & (d) Field = 2.0kVcm^{-1}

(i) Field = 15.0kVcm^{-1}

(j) Field = 20.0kVcm^{-1}

Legend:
— Energy
······ Bound Γ valley
--- Unbound Γ valley
-- Bound L valleys
-·- Unbound L valleys
-··- Bound X valleys
··· Unbound X valleys
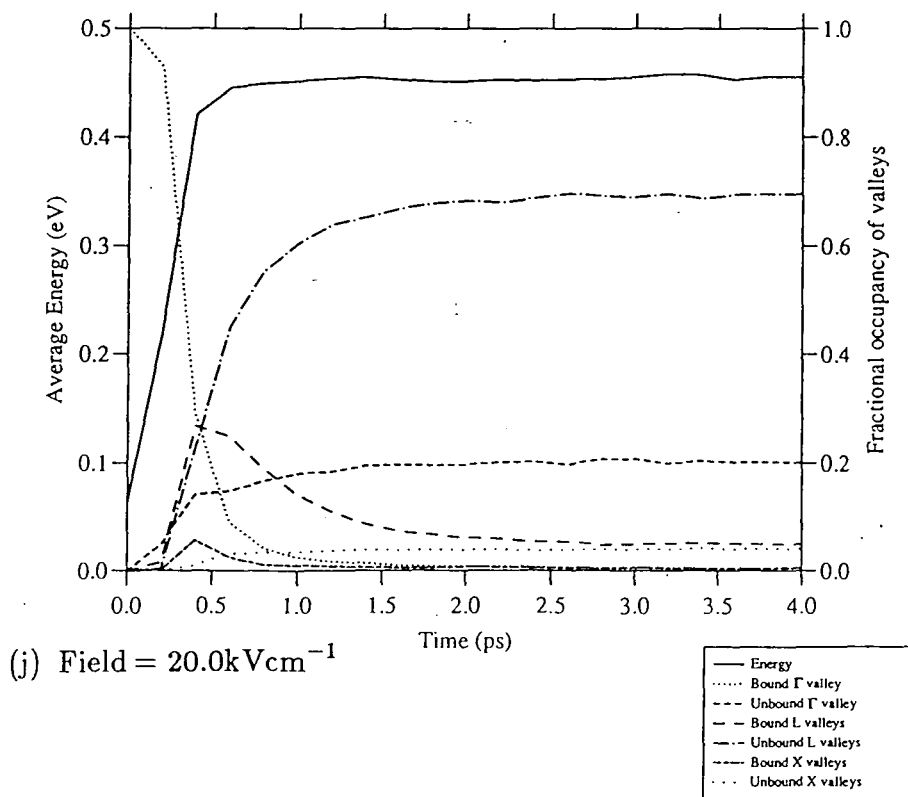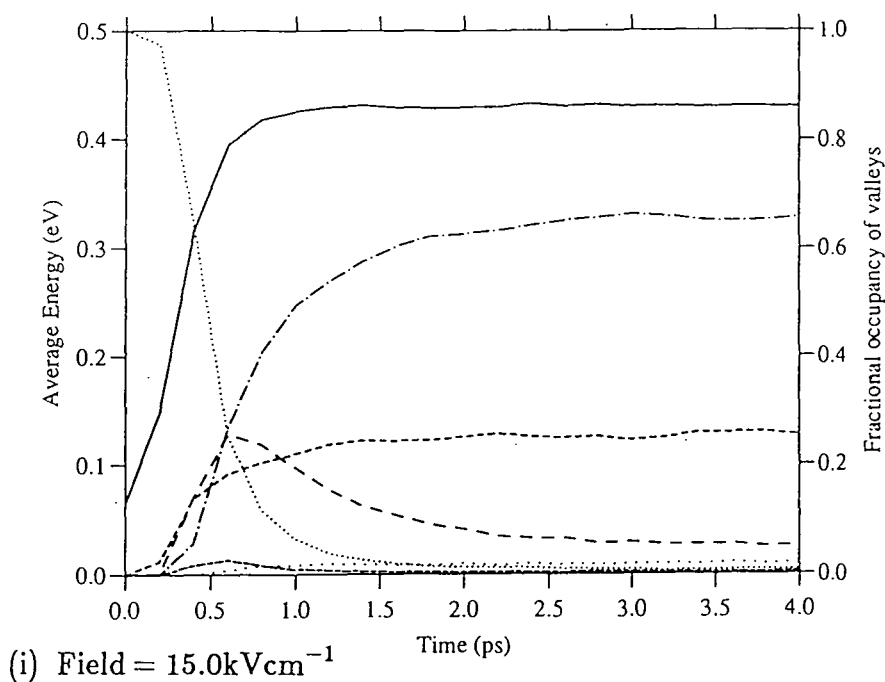
Figure 4.8 (i) & (j)

(i) Field = 15.0kVcm^{-1} & (j) Field = 20.0kVcm^{-1}

majority of the electrons remain in the subbands of the Γ valley well, but for stronger fields than this there is a greater proportion of the electrons in the unbound states at steady state. As the field intensifies the Γ valley well states depopulate faster and the steady state is reached quicker.

At 2.0kVcm^{-1} the L valleys states start to populate, slowly at first. We can see the time dependence of the population of the L valleys if we study fields above 4.0kVcm^{-1} (figure 4.8 (e) to (j)), initially it is the bound states that are occupied, however as the simulation progresses, it is in the L valley unbound states that the electrons are more likely to inhabit.

The X4 valley states begin to fill at fields in excess of 10.0kVcm^{-1} (figure 4.8 (h) to(j)), and follow a similar trend to the L valley states described above. That is, it is the bound states that are the first to populate, but in the steady state a majority of the electrons in the X4 valleys reside in the unbound states. For fields greater than 6.0kVcm^{-1} for the L valleys, and 15.0kVcm^{-1} for the X4 valleys, the bound state populations exhibit a transient overshoot which increases with field.

When considering the average energy curves of in figures 4.8 (a) to 4.8 (j) it should be remembered that what is plotted is the *average* energy, and the ensemble of electrons will have a distribution about this mean. Consider first the low field curves of figures 4.8 (a) to 4.8 (d), in which the average energy rises slowly. The emission of carriers from the well into the unbound Γ valley states, from which they have a very small probability of returning to the bound states, is slow and so steady state is reached only

after a long time. At the lowest fields the average energy is below the threshold at which scattering to the unbound states is possible, but there are carriers with energies above this average that are able to make this transition. However the probability of scattering to the unbound states is low and only a small fraction of the electrons at these energies make the transition. As the field is increased the number of electrons that are at energies where they are able to scatter to the barrier states increases, and the rate of population of the unbound states increases. This trend is also enhanced because, as mentioned above, there is a region of energy where the relative probability of scattering to unbound states is increased.

At the higher fields, there is also an increasing number of (un)bound electrons that reach energies at which scattering to the (un)bound states of the L valleys is probable, and so these states start to populate. Further increase of the field promotes the scattering of electrons in the bound states of the L valley, as well as the bound and unbound Γ valley states, to the unbound L valleys states.

The threshold for scattering to bound L valley states is lower in energy than for transitions to unbound L valley states. Also scattering to the bound states has a step-like form as a function of energy as opposed to the softer increase of the rates for transitions to the unbound states. As a result, there is significant transfer of electrons to bound L valley states as Γ valley bound electrons heated by the field pass through the relevant energy range. This has the effect of removing electrons which would otherwise have reached

the threshold for scattering to the unbound L valley states. Furthermore, the rate at which the electrons increase in energy in the heavier L valley is much less than in Γ valley and consequently they are slower to reach energies where they can scatter to the unbound states. In effect the L valley bound states cause a bottleneck which results in the transient build-up of carriers in those states which is seen in the simulations and has been commented on above. The peak in the population increases with field as electrons arrive at a greater rate at energies where scattering to these states is probable. The transient occupancy is shorter lived for higher fields as the excitation out of the L valley bound states occurs at a greater rate. At still higher fields similar processes occur involving the X4 valley states. The L and X4 valley unbound states are also populated by electrons transfering from the unbound Γ valley states.

The X valley populations are small for the fields we consider and so the assumption of using only the X4 valleys for the strained well material is justified.

4.5.3 Transient velocity characteristics

The time dependence of the average drift velocity for different fields is shown in figure 4.9. The general nature of the response is similar to that for bulk semiconductors (see for example figure 2.4). The average drift velocity rises from zero, exhibiting transient velocity overshoot at the higher fields to reach what appears to be a steady state value within about 5.0ps. The velocity peak develops, that is, it increases in magnitude but exists for
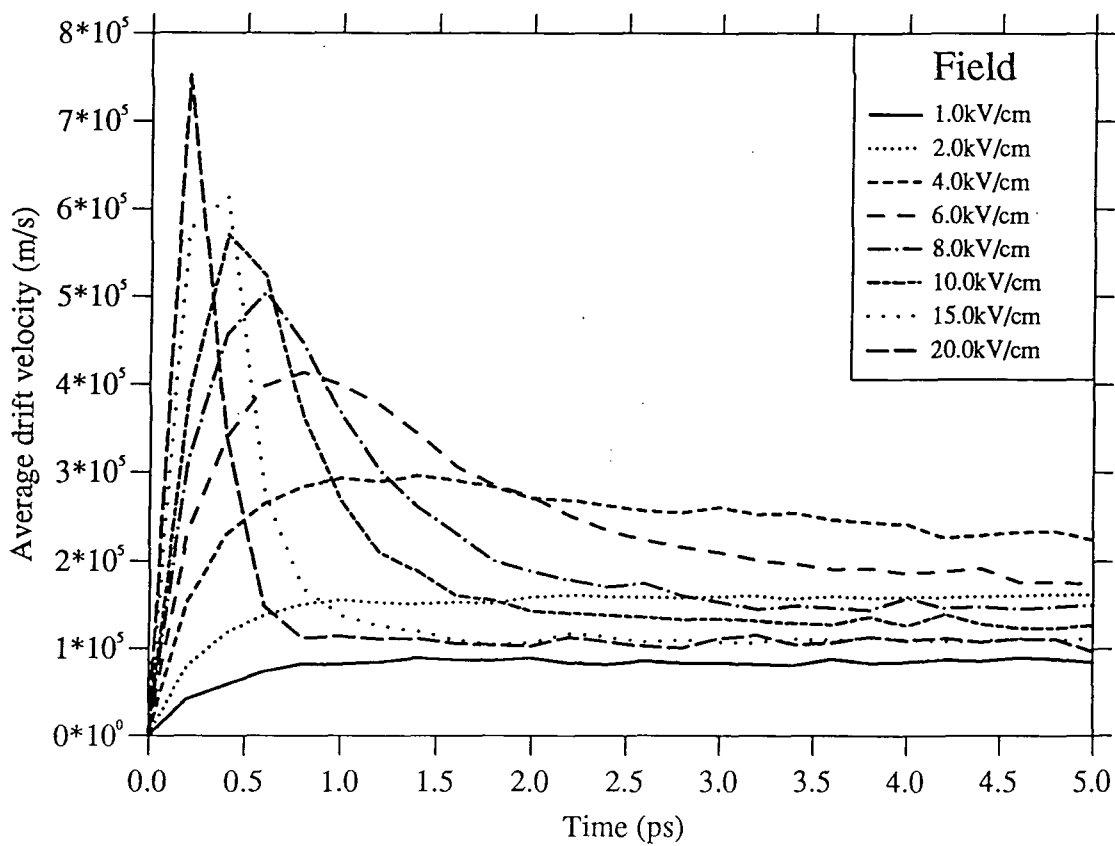
Figure 4.9

Average drift velocity against time for a range of fields

(0.0 to 20.0kV/cm) for the strained In15Ga85As/GaAs quantum well.

shorter periods, as the field is increased above $4.0 \mathrm{kVcm^{-1}}$. To understand why the peak changes as it does, it is instructive to consider the real- and reciprocal-space distributions of the carriers along with the velocities. These are plotted for a range of fields in figures 4.10 (a) to 4.10 (j), where the average drift velocity and the fractional valley occupancy are plotted together as a function of time. As a guide to the relative velocities attained for each field, all the velocity curves are plotted on the same scale.

As we now know from examining the average energy response to the fields, and the distribution of the carriers, the system is not in a steady state within 5.0ps for low fields and may take many tens of picoseconds to reach this balance. However, the velocity appears to have reached some sort of steady state due to the similarity in effective masses of the well and barrier material states. In quantum wells where the barrier material has an appreciably larger effective mass than the well material, such as the AlGaAs/GaAs well discussed in chapter three (also Moško & Novák 1989, Masselink *et al* 1988), transfer of carriers into the barrier causes a reduction in the average drift velocity and has a major effect on the velocity-field characteristic; this is the real space transfer induced negative differential mobility (Hess *et al* 1979).

As can be seen from the graphs, there is an obvious correlation between the valley populations, the fields and the velocity. As the field is increased the velocity rises more quickly. When transfer to the satellite valleys occurs, the velocity rise is repressed and may, as more carriers enter
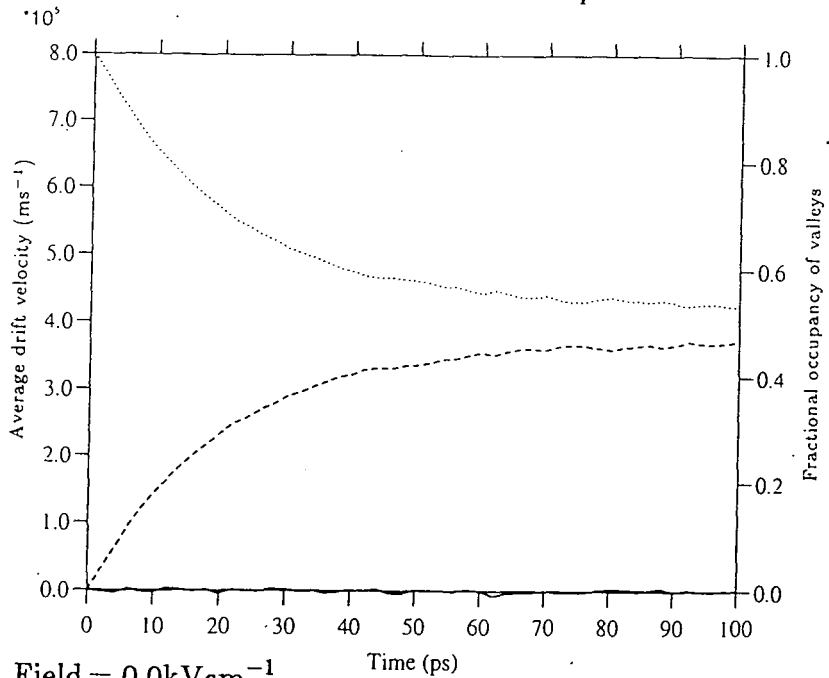
(a) Field $= 0.0\mathrm{kVcm}^{-1}$

(b) Field $= 0.5\mathrm{kVcm}^{-1}$

Velocity
Bound Γ valley
Unbound Γ valley
Bound L valleys
Unbound L valleys
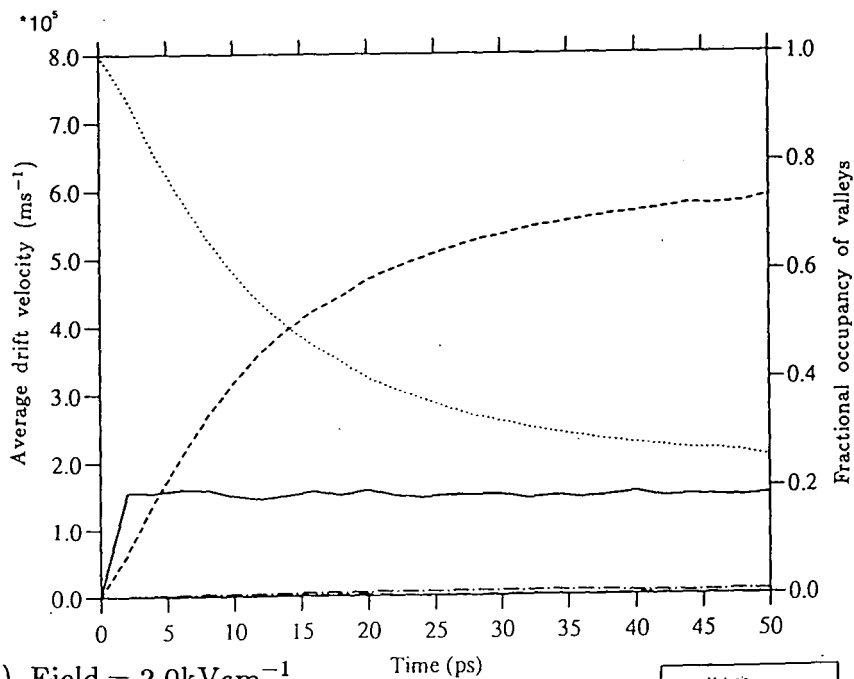Bound X valleys
Unbound X valleys
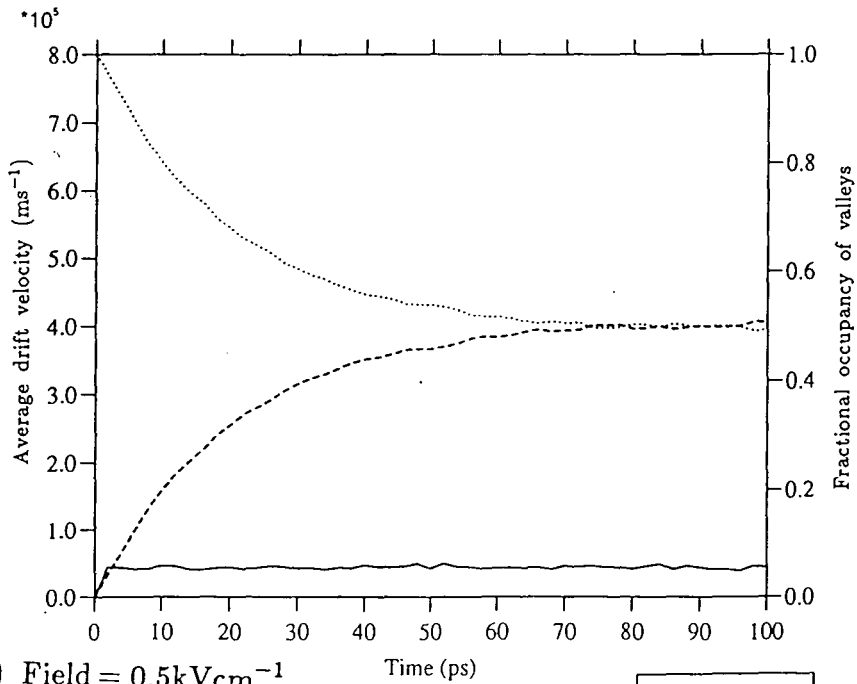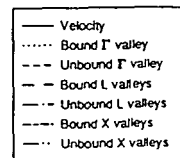
Figure 4.10 (a) to (j)

Average electron drift velocity and fractional occupancy of bound and

unbound states in all valleys plotted against time for the strained

$In_{0.15}Ga_{0.85}As/GaAs$ quantum well structure.
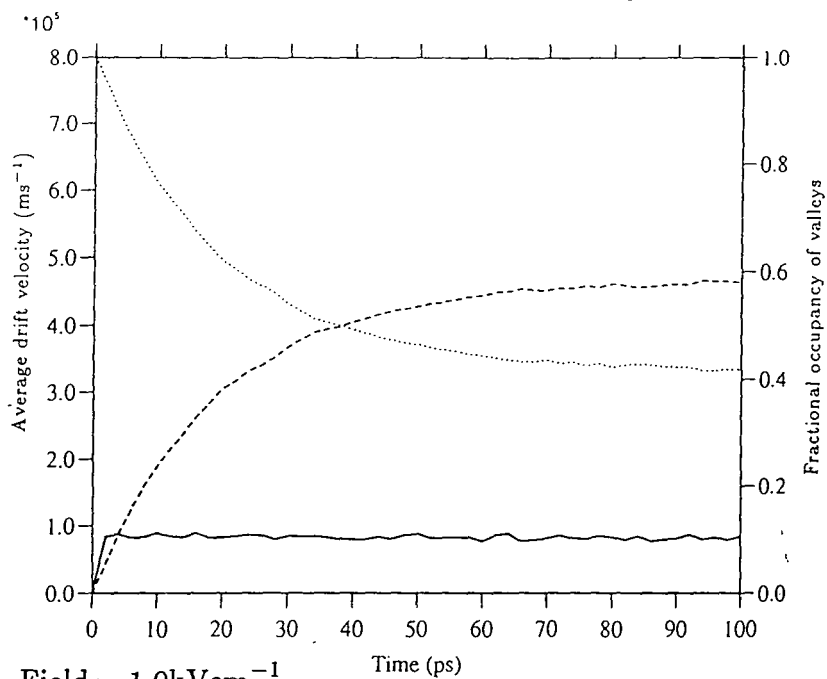
(c) Field = 1.0kVcm^{-1}
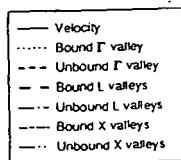
(d) Field = 2.0kVcm^{-1}

Figure 4.10 (c) & (d)

(c) Field = 1.0kVcm^{-1} & (d) Field = 2.0kVcm^{-1}

(e) Field $= 4.0\mathrm{kVcm}^{-1}$

(f) Field $= 6.0\mathrm{kVcm}^{-1}$

Legend:
— Velocity
····· Bound Γ valley
- - - Unbound Γ valley
— — Bound L valleys
— · — Unbound L valleys
— ·· — Bound X valleys
— ··· — Unbound X valleys
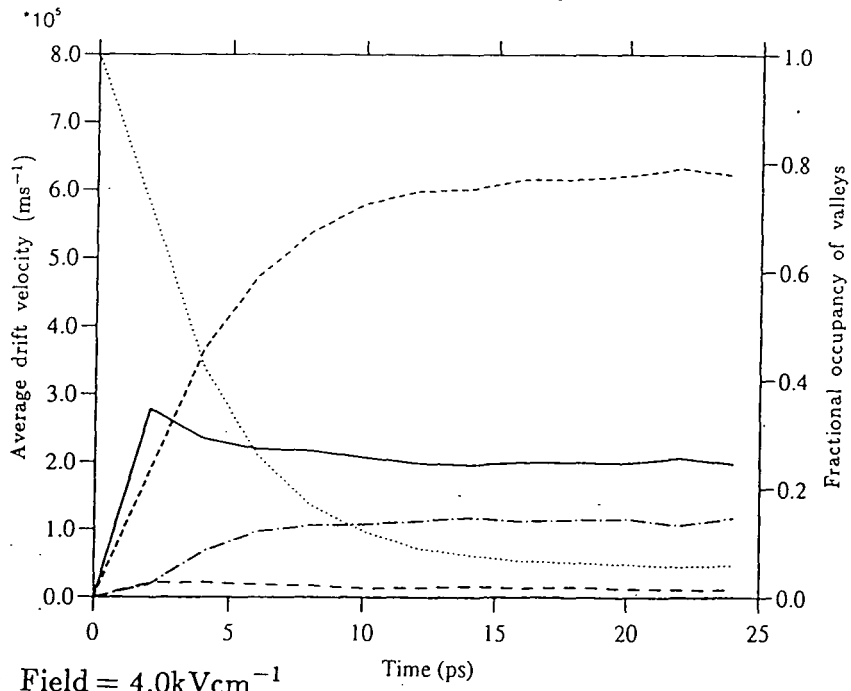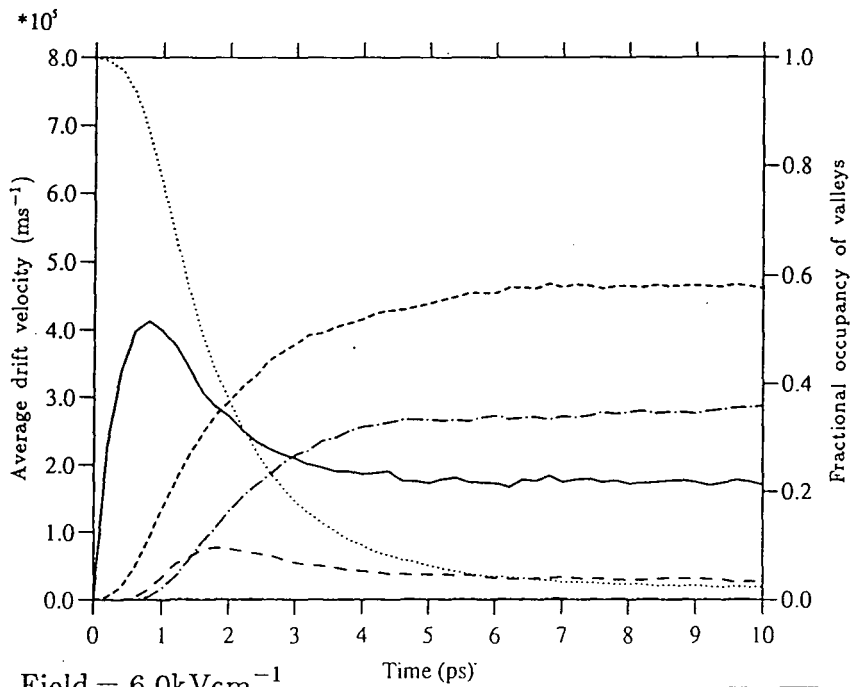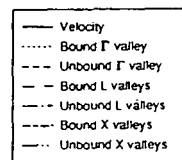
Figure **4.10** (e) & (f)

(e) Field $= 4.0\mathrm{kVcm}^{-1}$ & (f) Field $= 6.0\mathrm{kVcm}^{-1}$
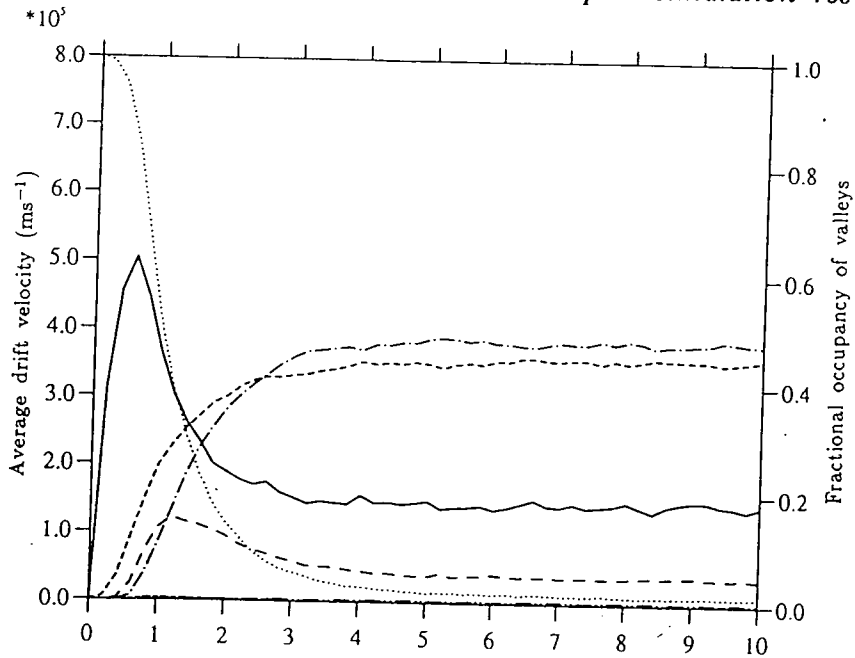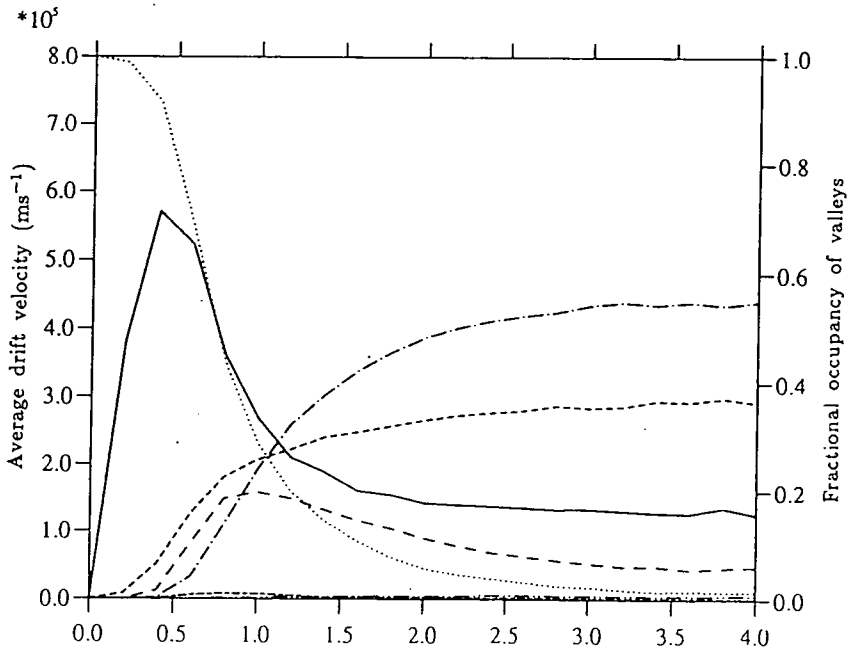
(g) Field = 8.0kVcm^{-1}
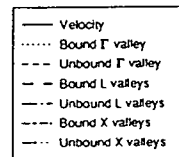
(h) Field = 10.0kVcm^{-1}

Figure 4.10 (g) & (h)

(g) Field = 8.0kVcm^{-1} & (h) Field = 10.0kVcm^{-1}

(i) Field $= 15.0 \mathrm{kVcm}^{-1}$
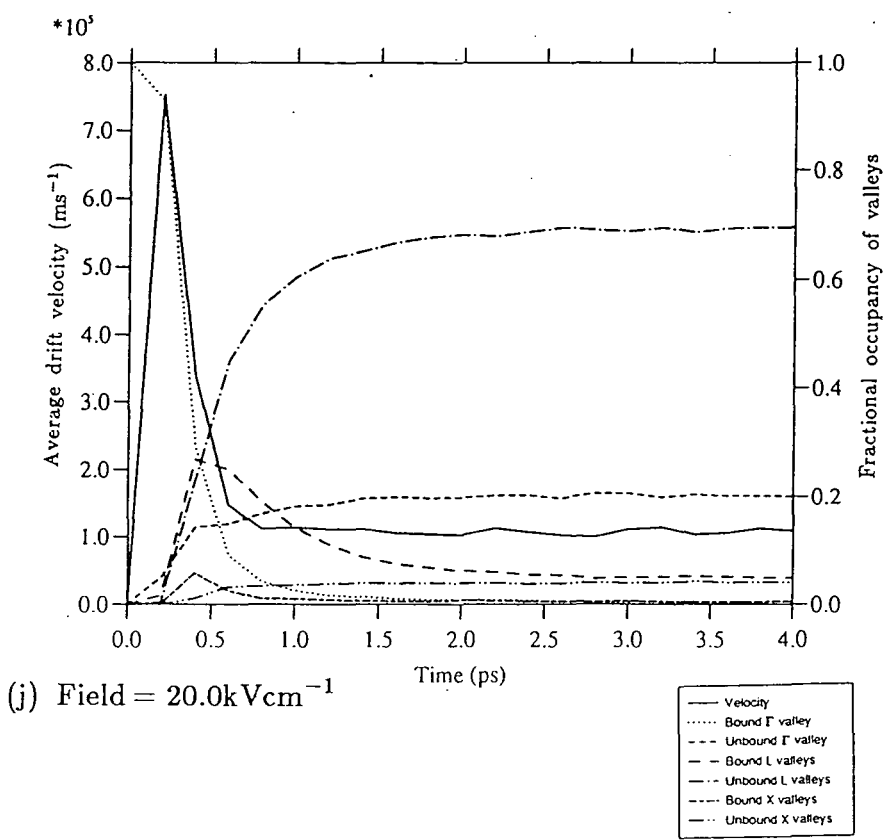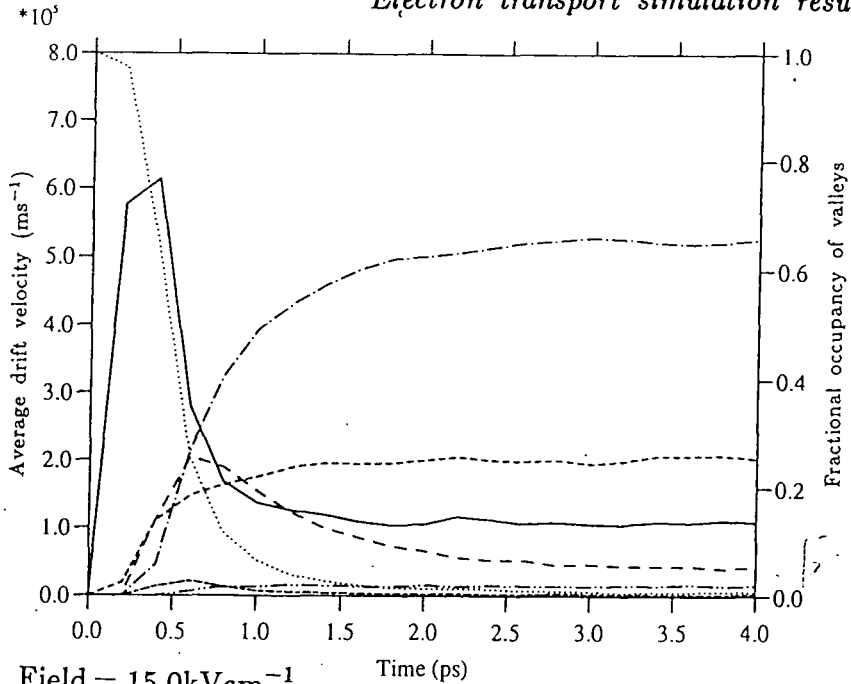
(j) Field $= 20.0 \mathrm{kVcm}^{-1}$

Figure 4.10 (i) & (j)

(i) Field $= 15.0 \mathrm{kVcm}^{-1}$ & (j) Field $= 20.0 \mathrm{kVcm}^{-1}$

the satellite valley states, be reversed causing the overshoot effect.

For high fields the carriers can attain large velocities quickly, but a rapid transfer to the L and X valleys occurs, which is even faster than transfer to the Γ valley unbound states for fields $> 15.0\text{kVcm}^{-1}$, and this causes the velocity to drop substantially in a short period. This fast re-distribution of carriers allows the system to reach equilibrium quickly.

4.5.4 Comparison of transport simulation results of the strained and un-strained well systems

The main differences in the results of the strained and unstrained layer simulations are to be seen in the average drift velocity and the real- and reciprocal-space distributions. Figure 4.11 (a) to (c) compares these quantities plotted against time for three fields (one low $= 0.5\text{kVcm}^{-1}$, one medium $= 4.0\text{kVcm}^{-1}$, and one high $= 20.0\text{kVcm}^{-1}$) to highlight the major points of interest.

At low fields (figure 4.11 (a)), where there is no transfer of charge to the satellite valleys, the velocity profile for both systems is closely matched at all times. For the unstrained layer the rate of electron emission from the bound states of the Γ valley well is smaller and there is a larger fraction of carriers still bound at steady state.

For medium fields (figure 4.11 (b)), in which electrons populate the L valleys, a higher peak in the average drift velocity develops in the unstrained device when compared with the results of the strained layer
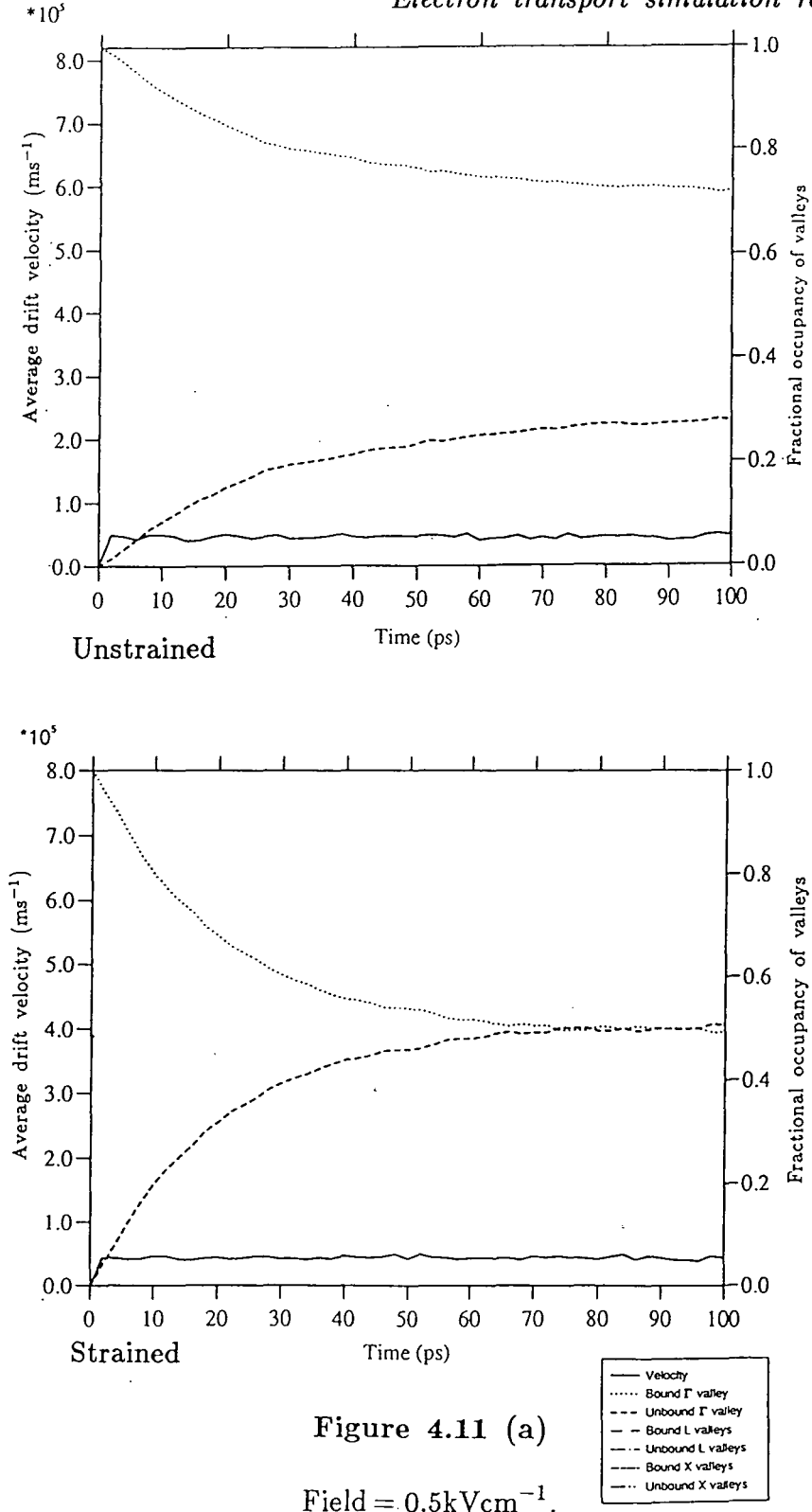
Figure 4.11 (a)

Field = 0.5kVcm^{-1}.

Figure 4.11 (a) to (c)

Average electron drift velocity and fractional occupancy of bound and

unbound states in all valleys plotted against time for the strained

and unstrained In$_{0.15}$Ga$_{0.85}$As/GaAs quantum well structures.

Unstrained

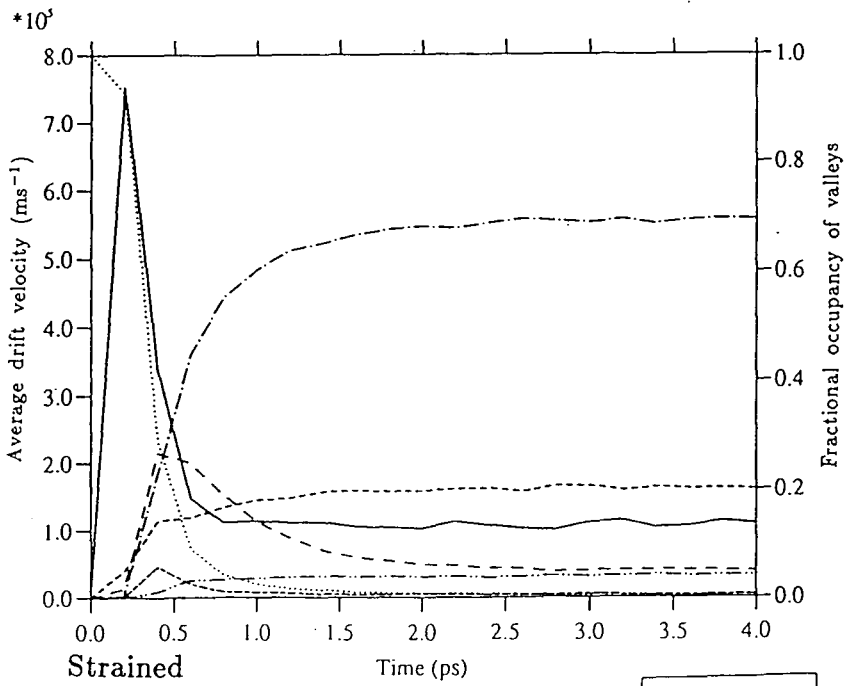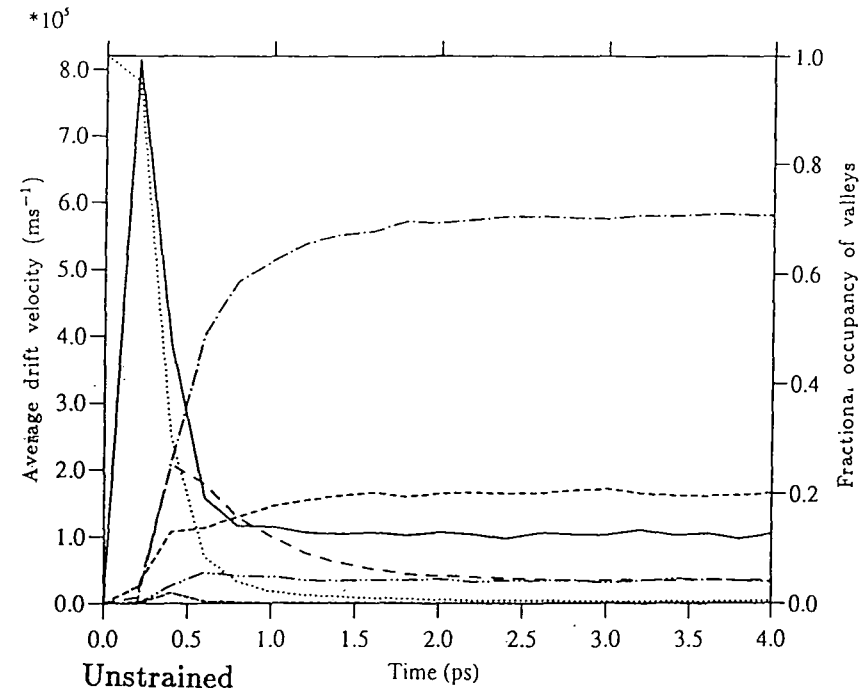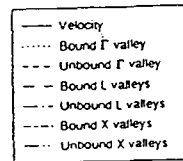Strained
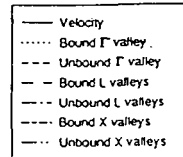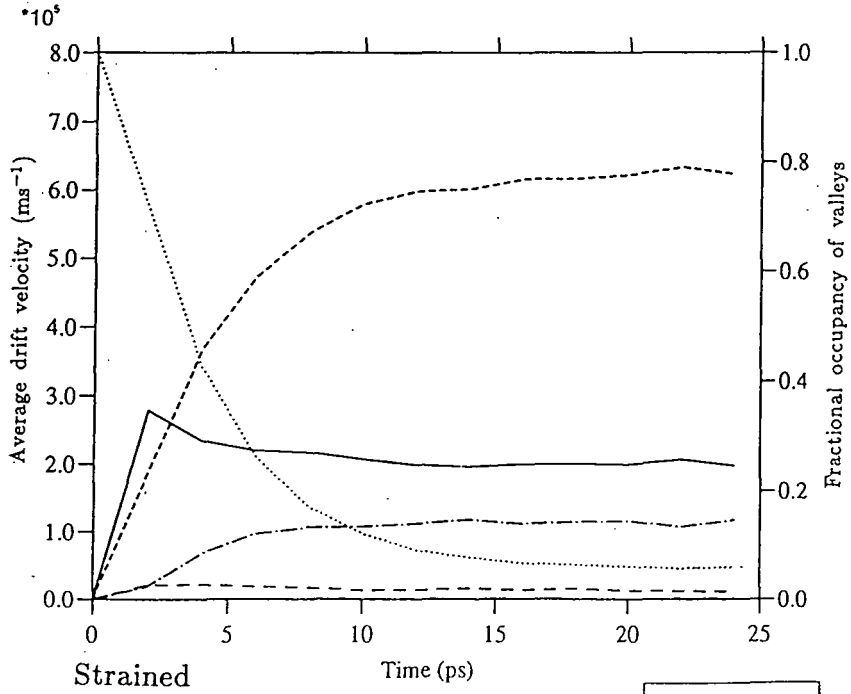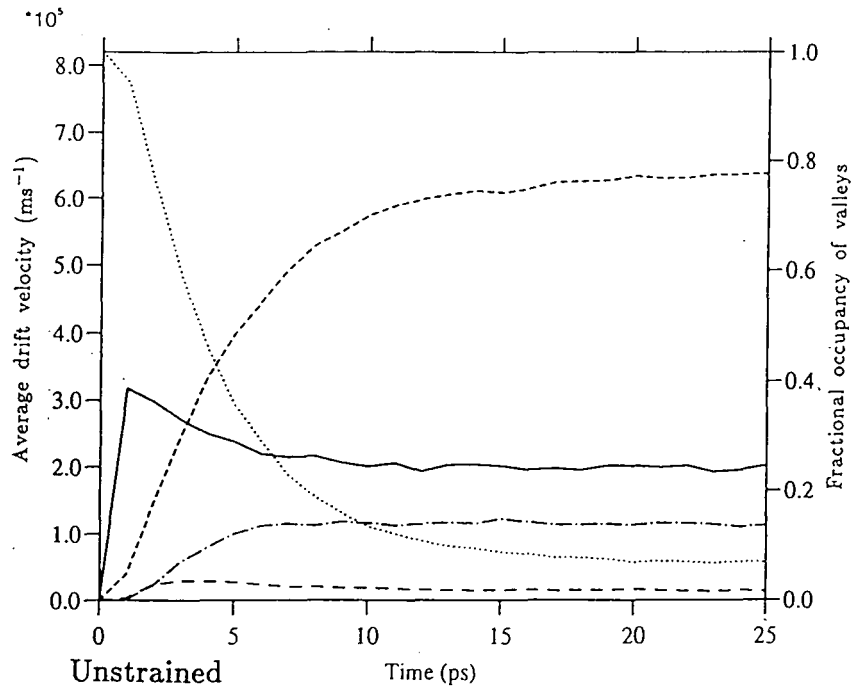
Figure 4.11 (b)

$Field = 4.0 kVcm^{-1}$.

Figure 4.11 (c)

Field = 20.0kVcm^{-1}.

simulation, but at steady state the velocities for both layers are equal. When considering relative populations of the states in the quantum well heterostructures at this field, we see that initial electron emission to the unbound states of the Γ valley is faster in strained layer than in the unstrained one and when the L valleys start to populate the relative populations of the valleys in both systems is similar, although there is always a slightly higher fraction of carriers in Γ valley subbands of the unstrained heterostructure.

High field drift velocities like those of figure 4.11 (c), where all valleys are populated, again show a larger peak in the average drift velocity of the unstrained layer but at steady state both simulations agree. Before the satellite valleys are occupied the emission rate in the strained device is again bigger than in the unstrained one. However, when the satellite valleys start to populate the general trend is the same in both cases; there is an overshoot in both X valley and L valley subband occupancy and at steady state most of the carriers are in the unbound states. The transient population overshoot of the X valley subbands is larger in the strained well than in the unstrained one.

The steady state velocity of both structures is compared in the next section; here we shall discuss the transient velocity effects and the occupancy of states. The larger valley separations of the well material in the unstrained layer coupled with a slightly lower Γ valley effective mass causes the higher transient peak velocity seen in that system because the electrons are able to attain higher energies/velocities more quickly before

intervalley scattering occurs. Another consequence of this difference in the bandstructure of the well material is that more electrons are able to reach energies where scattering to the X valley subbands is probable before they are emitted from the well. This results in the higher transient population of the X valley subbands in that system.

The slower emission rate for, and larger population at steady state of, electrons in the unstrained Γ valley subbands is attributed to the greater depth of this well.

4.5.5 Steady state velocity characteristics

Figure 4.12 shows the average drift velocity results plotted against electric field for bulk GaAs and for the strained and unstrained quantum wells, at a time when the simulation had reached steady state. As can be seen, the quantum well models have the same low field mobility (slightly higher than bulk GaAs) but generally the three curves are very similar. It is perhaps not surprising that the steady state velocity/field characteristic of the quantum well is similar that of bulk GaAs, as in steady state most of the carriers are in the barrier material.

4.5.6 Comparison with experiments and other simulations

Despite the use of InGaAs in HEMTs, we are unaware of other theoretical studies or any basic experimental measurements of transport in $In_{0.15}Ga_{0.85}As/GaAs$ double heterostructure quantum wells. Under the conditions relevant to the devices the closest simulation results we have

References for chapter four.

Artaki M. and Hess K. 1988 *Phys. Rev. B* **37** 2933

Bastard G. 1984 *Surface Science* **142** 284

Bhattacharyya K., Orwa J. O., and Goodnick S. M. 1993 *J. Appl. Phys.* **73** 4396

Brennan K. F. and Park D. H. 1989 *J. Appl. Phys.* **65** 1156

Brum J. A. and Bastard G. 1985 *Solid State Comm.* **53** 727

Brum J. A. and Bastard G. 1986 *Phys. Rev. B* **33** 1420

Chamberlain M. P., Hoare D., Kelsall R. W. and Abram R. A. 1992 *Semicond. Sci. Technol.* **7** B45

Crow G. C., Kelsall R. W. and Abram R. A. 1993 *Semicond. Sci. Technol.* **8** 219

Dollfus P., Bru C., and Hesto P. 1993 *J. Appl. Phys.* **73** 804

Hess K., Morkoç H., Shichijo H., and Streetman B. G. 1979 *Appl. Phys. Lett.* **35** 496

Inoue K. and Matsuno T. 1993 *Phys. Rev. B* **47** 3771

Jensen G. U., Lund B., Fjeldly T. A. and Shur M. 1991 *IEEE Trans. Electron Devices* **38** 840

Ji G., Huang D., Reddy U. K., Unlu H., Henderson T. S. and Morkoç 1987 *J. Vac. Sci. Technol. B* **5** 1346

Kelsall R. W. 1989 *Phd Thesis* University of Durham, unpublished.

Kelsall R. W. 1992 *Private communication* unpublished.

Kelsall R. W. and Abram R. A. 1992 *Semicond. Sci. Technol.* **7** B312

Kelsall R. W. and Abram R. A. 1992 in *Proceedings of 8th NASECODE, Vienna, 1992* Boole Press, Dublin. p34.

Kim K. W., Tian H., and Littlejohn M. A. 1991 *IEEE Trans. Electron Devices* **38** 1737

Kobayashi E., Matsuoka T., Taniguchi K., and Hamaguchi C. 1989 *Solid State Electron.* **32** 1845

Lee K., Shur M. S., Drummond T. J., and Morkoç H. 1983 *J. Appl. Phys.* **54** 6432

Masselink W. T., Braslau N., LaTulipe D., Wang W. I., and Wright S. L. 1988 *Proceedings of the International Symposium on Gallium Arsenide and Related Compounds, Heraklion 1987* Institute of Physics, London. p665.

Moško M. and Novák I. 1989 *J. Appl. Phys.* **66** 2011

Park D. H. and Brennan K. F. 1989 *J. Appl. Phys.* **65** 1615

Park D. H. and Brennan K. F. 1989 *IEEE Trans. Electron Devices* **36** 1254

Park D. H. and Brennan K. F. 1990 *IEEE Trans. Electron Devices* **37** 618

Tanimoto H., Yasuda N., Taniguchi K., and Hamaguchi C. 1988 *Jpn. J. Appl. Phys.* **27** 563

Thobel J. L., Dessenne F., Fauquembergue R., Baudry L., and Bourel P. 1991 *Proceedings of the 17th International Symposium on Gallium Arsenide and Related Compounds, Jersey 1990* Institute of Physics, London. p351.

Thobel J. L., Baudry L., Dessenne F., Charef M., and Fauquembergue R. 1993 *J. Appl. Phys.* **73** 233

CHAPTER FIVE

SUMMARY, CONCLUSIONS,

& SUGGESTIONS FOR FURTHER WORK

5.1 Summary & conclusions.

$\mathcal{T}$he main aim of the work presented in this thesis was the study, using the Monte-Carlo method, of the significant factors affecting electron transport in strained $In_{0.15}Ga_{0.85}As/GaAs$ quantum well heterostructures at room temperature.

In chapter two we explored the effects of strain and alloying on the electron transport properties of bulk III-V semiconductors. After first testing our model on bulk GaAs, InAs, and $In_{0.53}Ga_{0.47}As$, we simulated electron transport in $In_xGa_{1-x}As$ ($x = 0.05, 0.10, 0.15, 0.20,$ and 0.25) with particular consideration of the effects of alloying and strain on the low field mobility, peak velocity, and saturation velocity. In the unstrained material, we found a higher low field mobility, greater peak velocity and lower saturation velocity with increasing indium concentration x (despite the accompanying increase

in alloy scattering), which were attributed to the reduced Γ valley effective mass, the higher Γ to L valley separation, and the larger effective masses of the satellite valleys, respectively. Strain increased the Γ valley effective mass and decreased the inter-valley energies, which caused a lower low field mobility than in the unstrained material and bulk GaAs and a lower peak velocity than in the unstrained material but still larger than in bulk GaAs.

The lattice vibrational modes of heterostructures are different from bulk materials. We have compared three continuum phonon models (the Hydrodynamic Model (HDM), the Dielectric Continuum Model (DCM), and the Bulk Phonon Approximation (BPA)) with specific reference to the electron-phonon scattering rates they predict and how the scattering affects the low field transport properties of electrons bound in an $Al_{0.3}Ga_{0.7}As/GaAs$ quantum well. This work was reported in chapter three. We found that the transport properties from simulations which used the HDM and BPA were in good agreement and compared well with experimental velocity-field results of a similar system. We concluded that, until more realistic continuum phonon models have been investigated with respect to electron transport in quantum wells, the BPA was a suitable model to use in carrier transport simulations.

In chapter four we developed the Γ valley quantum well model introduced in chapter three, and included the L and X valleys, alloy scattering, strain effects, and scattering rates for transitions between bound and unbound states. We compared the latter scattering rates and found

them to be small in comparison to unbound-to-unbound and bound-to-bound state scattering rates due to the small overlap between bound and unbound states. The transient and steady state transport characteristics of electrons in the strained and (artificially) unstrained $In_{0.15}Ga_{0.85}As/GaAs$ quantum well heterostructure were studied at fields large enough that real- and reciprocal-space transfer effects occurred. The differences in the strained and unstrained transient and steady state properties were found to be small and mainly transient, which is to be expected because at steady state most of the electrons inhabit the unbound states, which are nearly identical in both systems. The low field mobilities of the strained and unstrained quantum wells were slightly larger than in bulk GaAs.

Although electrons in bulk and artificially strained $In_{0.15}Ga_{0.85}As$ have a smaller low field mobility, the results from the strained quantum well model showed a larger value, when both were compared to bulk GaAs.

5.2   Suggestions for further work.

*O*ur model may be used with little extra development work to study electron transport in a range of quantum wells with different indium concentrations or, in fact, wells made from other III-V semiconductor materials.

One way in which to refine the quantum well model of chapter four further is by the introduction of a more complex bandstructure model. Models derived using, for example, pseudopotential calculations offer one way of modelling the effects on energy levels due to the interaction of equivalent and non-equivalent valley states, non-parabolicity, and non-spherical bands. However, the complexity of the simulation is already considerable due to the multiplicity of scattering processes and bands, and the incorporation of more complete bandstructure information would be a substantial task.

As was mentioned in chapter three, the development of sophisticated, hybrid, continuum phonon models, which show good agreement with the results of microscopic models of lattice vibrations in quantum well heterostructures, occurred too late to be studied in this work. It would be worthwhile to carry out further work to investigate the transport properties of carriers in quantum wells when the scattering rates are calculated from the new hybrid phonon models.